Multicomponent Self-Assembly of C_{60}/C_{70}-Decanethiol Systems

By

Bosheng Li

A thesis submitted to the University of Birmingham for the degree of Doctor of Philosophy

School of Physics and Astronomy

University of Birmingham

June 2025

Abstract

This study investigates the self-assembly of C_{70} fullerene and decanethiol (DT) molecules on Au(111) substrates, focusing on the influence of different factors (molecular symmetry, intermolecular interactions, deposition methods, etc) in forming ordered nanostructures. Utilizing the low-temperature scanning tunnelling microscopy (LT-STM) in an ultra-high vacuum environment, I characterize the bicomponent C_{70}/DT system at room temperature (RT) and low temperature (LT) conditions (290 K and 77 K). Two primary self-assembled structures, dimer row and porous framework, are observed, with their formation driven by van der Waals forces and sulfur-gold bonding. Intramolecular LT-STM data reveals the molecular orientations of C_{70}, enabling the construction of structural models for C_{70}/DT system, though the uncertainties necessitate further refinement. Additionally, mixed C_{60}-C_{70}/DT system demonstrate that both fullerenes adapt their orientations to form guided supramolecular frameworks, highlighting the role of molecular geometry and deposition methods in controlling molecular assembly. These findings advance the understanding of C_{70}-based self-assembly mechanisms and their potential applications in molecular electronics, sensors, and surface engineering.

Abbreviation

AFM	Atomic Force Microscopy
DFT	Density Functional Theory
DT	Decanethiol
FCC	Face Centred Cubic
FCS	Fluorescence Forrelation Spectroscopy
HCP	Hexagonal Closed Packed
HOMO	Highest Occupied Molecular Orbital
HOPG	Highly Oriented Pyrolytic Graphite
LDOS	Local Density of States
LEED	Low Energy Electron Diffraction
LT	Low Temperature
LUMO	Lowest Unoccupied Molecular Orbital
MBE	Molecular Beam Epitaxy
PVD	Physics Vapor Deposition
RT	Room Temperature
SAM	Self-Assembled Monolayer

SC	Simple Cubic
SEM	Scanning Electron Microscopy
STM	Scanning Tunnelling Microscopy
STS	Scanning Tunnelling Spectroscopy
TEM	Transmission Electron Microscopy
TSP	Titanium Sublimation Pump
UHV	Ultra-High Vacuum
VT	Variable Temperature
XPS	X-Ray Photoelectron Spectroscopy
XRD	X-Ray Diffraction
2D	Two Dimensional
3D	Three Dimensional

Acknowledgement

I express my deepest gratitude to those who have supported me throughout this doctoral journey. First, I thank my supervisor, Dr. Quanmin Guo, for his invaluable guidance, expertise, and encouragement, which shaped this work. I am also grateful to my co-workers, Prof. Jianzhi Gao and Prof. Minghu Pan from Shaanxi Normal University, for their careful guidance in our experimental design and paper writing.

To my colleagues and peers at University of Birmingham, thank you for the stimulating discussions and camaraderie that enriched my research experience. I extend special appreciation to Haoxuan Ding, Hualin Yang, Ying Gao, Haoyu Zhao and Chunqiu Xia for their assistance, collaboration, and shared enthusiasm.

I am indebted to my parents, for their unwavering love, patience, and belief in me. Their sacrifices and encouragement provided the foundation for this achievement. I also thank my friends, Yazhou Xu, Faisal Alayed, Fatmah Saad, Hanan Alhabeadi, Bin Zhang, for their moral support and moments of levity during challenging times.

Finally, I acknowledge the support from University of Birmingham, which made this research possible, and the resources provided by Nanoscale Physics Research Laboratory. This dissertation stands as a testament to the collective support of all those mentioned and many others unlisted but not unappreciated.

Contents

I. Introduction

Self-assembly is an import process, particularly for its applications in nanotechnology, molecular electronics, and catalysis. Among various molecules used for self-assembled monolayer formation, fullerene molecules and alkanethiol molecules are of particular interest due to their electronic properties, superior stability in the ambient and compatibility with gold substrates. In the fullerene-alkanethiol system, this phenomenon involves the interaction between fullerene molecules and alkanethiol molecules, which are long-chain hydrocarbons terminated with a thiol (-SH) group. This system is of significant interest due to its potential in creating well-defined nanostructures for applications in molecular electronics, sensors, and surface engineering.

In the C_{60}/C_{70}-alkanethiol system, self-assembly is driven by a synergy of interactions, including van der Waals forces, π-π stacking among fullerene molecules, and the sulfur-metal bonding of alkanethiols. These interactions facilitate the formation of ordered hybrid architectures, such as fullerene-terminated SAMs, fullerene clusters within alkanethiol matrices, or mixed fullerene-alkanethiol layers. The geometric differences between C_{60} (sphere, highly symmetric) and C_{70} (elongated, less symmetric) influence the packing density, molecular orientation and the stability of the assemblies, offering different properties for specific applications. In this work, we mainly focus on the self-assembly of C_{70}-decanethiol system. With lower symmetry, the self-assembly of C_{70} is considered to be more limited, as the C_{70} have less available stable binding types with the Au(111) substrate than C_{60}. Understanding the self-assembly mechanism of C_{70} will not only fill the gap in research on this system, but can also help to analyse the self-assembly mechanism of C_{60}.

In Chapter II, the literature reviews about various relevant fields are introduced. First, I introduced the molecular self-assembly, which is the basic concept of the research I conducted. Then, I introduced the Au(111) surface, which is used as the substrate for our sample. Au(111) is commonly used in the studies in surface science due to its low reactivity and high chemical stability. Understanding the properties of the Au(111) surface can be useful for analysing the molecule-surface interaction. Then, the self-assembly of decanethiol (DT) on Au(111) is introduced. DT

molecules bind with the Au(111) substrate through forming the Au-S bond or the S-Au-S bond. The structure of the alkanethiol monolayer is coverage dependent. The mobility of the DT alkane chains makes it available to interact effectively with other molecules. Finally, I introduced the C_{60} and C_{70} fullerenes, which have unique shapes and properties. Understanding the properties of C_{60} and C_{70} fullerenes can help us to analyse the interactions of molecules within the complex bicomponent and multicomponent self-assembly system.

In Chapter III, the low temperature scanning tunnelling microscope (LT-STM) housed in an ultra-high vacuum (UHV) chamber is introduced. STM is a powerful instrument for studies in surface science. Especially, with the cryogenic equipment of LT-STM, the molecules and atoms can be frozen at 77 K or 5 K, which can reveal the intramolecular structure. The other equipment used for sample preparation and maintaining the UHV system is then introduced. The working principle for STM is also introduced in this chapter.

In Chapter IV, the first experiment is introduced, which is the C_{70}/DT self-assembled structures at RT. There are mainly two self-assembled structures observed in this system, respectively the C_{70}/DT dimer row structure and the C_{70}/DT porous framework structure. Through careful measurement, we have learned the details of these bicomponent self-assembled structures, and we explain how these structures are formed. The thermal stabilities of both structures are also introduced.

In Chapter V, we conducted the LT scanning for the C_{70}/DT system. According to intramolecular information from the LT data, we clarified the molecular orientations of C_{70} molecules in different structures and hence constructed structural models. Based on our measurement for the structure and our analysis about the arrangement of DT, several reasonable structural models are built. Further work is still needed to determine which structural model is the most appropriate because of uncertainties in the measurement.

In Chapter VI, the self-assembly of mixed C_{60}-C_{70}/DT system is introduced. Through changing the deposition methods of C_{60} and C_{70}, three different samples were prepared to compare the behaviours of C_{60} and C_{70}. It is interesting to notice that both C_{60} and C_{70} can be guided to form the pre-existing self-assembled structure through adapting their molecular orientations and binding sites on the Au(111) surface, which reveal their potential in the synthesis of surface supramolecular frameworks.

Through the research in the C_{70}/DT self-assembly on the Au(111) surface, we have observed how the geometric shape influences the molecular self-assembly. And from the data showing the formation of their structures, we have noticed how the C_{70} arrange their positions and interact with the neighbouring C_{70} molecules. And that shows us a clear process of the self-assembly in C_{70}/DT system.

Through the research in mixed C_{60}-C_{70}/DT self-assembly on Au(111) surface, we observed how the different fullerene molecules affect the arrangement of other surrounding fullerene molecules. And the appearance of mixed structure of C_{60} and C_{70} indicates that the self-assembled structure can be precisely controlled by carrying experimental parameters (molecular ratio, molecule-substrate interaction).

II. Literature Review

1. Molecular Self-Assembly

Molecular self-assembly is defined as the assembly of molecules without any guidance from an external source. The molecules spontaneously organize into the ordered structures driven by non-covalent interactions, such as van der Waals interaction, hydrogen bonding, π-π bonding, metal coordination, etc.[1] Molecular self-assembly has been widely observed and proved to be one of the fundamental mechanisms in natural systems, such as DNA double-helix assembly and protein folding[2-4]. Due to its ability to achieve nanoscale precision, molecular self-assembly has been widely applied in the fields such as nanotechnology, medicine, and materials science as a synthetic strategy[5-10].

1.1 Basic Principles of Molecular Self-Assembly

Different from covalent bonding, of which the molecules form strong and permanent chemical bonds, self-assembly relies on the weaker and reversible interactions, allowing dynamic and adaptable structures. Normally, these interactions include: i) Van der Waals force. This kind of non-specific attraction comes from the temporary dipoles in molecules[11], which contributes to the molecular packing in crystals (three-dimensional (3D)) and surfaces (two-dimensional(2D)) assemblies. ii) Hydrogen bonding. This is a relatively strong and directional interaction between electronegative atoms (such as oxygen, nitrogen) and hydrogen atoms bonded to other similar atoms[12], which is found critical in stabilizing structures such as the DNA double helix[13]. iii) π-π stacking. This kind of interaction happens in between the aromatic rings, where they interact with each other through overlapping the π-orbitals[14], and the supramolecular assemblies such as in conjugated polymers system[15] are thus stabilised. iv) Metal coordination. This is the interaction between metal ions and ligands[16], which can direct the assembly of complex structures, such as metal-organic frameworks[17,18]. v) Electrostatic interactions. This kind of interaction happens in between the groups which are charged oppositely, which contribute to the assembly such as in ionic systems[19]. vi) Hydrophobic interactions. This interaction happens in the aqueous

environments, the nonpolar molecules will aggregate to avoid contact with water, which is observed in the formation of structures like lipid bilayers in cell membranes[20].

In each particular system, some of these interactions act synchronously, but usually only one of them is considered to play a dominant role, which needs to be analysed based on the specific molecular systems and their environmental conditions.

To ensure the formation of ordered structures, the molecular self-assembly is governed by several fundamental principles. First, the self-assembled structures minimize the free energy of the system, which is determined by the Gibbs free energy change[21], and the self-assembly process helps the system to achieve a thermodynamically stable state[22]. This is driven by the balance of attractive and repulsive interactions of the neighbouring molecules, leading to structures with the lowest possible energy configuration. In addition, the kinetic effects also play important roles in some systems, which can further affect the final self-assembled structures. It is possible for the samples transfer into kinetically trapped states, where the overall self-assembly process of the system is obstructed when the local areas of the system have reached their minimum energy[23]. This has been observed in the processes such as the formation of the self-assembled monolayers (SAMs)[24]. During the preparation of SAMs, the molecules deposited on the substrate may form into the clusters if the deposition rate is too fast. And this rapid accumulation of molecules makes it easier for them to stack into more stable structures in the *z* direction, thus the diffusion of molecules on the substrate is restricted.

Except for these two major principles, the molecular self-assembly would also be affected by the external factors, such as environmental temperature, molecular concentration and solvent/substrate types[25-30]. Even for the same system, the self-assembly can be varied in the different external conditions[26]. Therefore, when synthesising the specific self-assembled structures, it is necessary to analyse not only the interactions between the target molecules, but also the external factors such as the molecules-substrate interactions, the substrate temperature and the deposition methods[31-33].

1.2 Development and Applications

The molecular self-assembly was first discovered from the biological systems ~ 1950's, Pauling *et al.* explored how chemical bonds shape protein structures[34], laying the groundwork for understanding the self-assembly process. Then Watson and Crick reported their discovery of DNA

double-helix structure[35], showing how molecules pair up naturally, and it is considered to be one of the classic examples of self-assembly in nature. By the 1980s and 1990s, with more of the self-assembly systems are further studied by researchers, their potentials are gradually being discovered, and researchers started to use it as an effective method to create and synthesize new materials. Mann reported the inorganic-organic molecular recognition processes at interfaces between the crystals and substrate macromolecules[36], revealing the potential technological application in synthetic materials. Whitesides *et al.* reported that the self-assembly could be used as a method to build the tiny structures in nanoscale[10], which strongly sparked the interest of researchers. Since the 1990s, with the support of the more advanced techniques, such as the scanning tunnelling microscopy (STM), atomic force microscopy (AFM), fluorescence correlation spectroscopy (FCS) and X-ray photoelectron spectroscopy (XPS), the properties of various of self-assembly systems are studied in detail[37-40]. In addition, with the development of computational and theoretical approaches, such as density functional theory (DFT) and molecular dynamics (MD) simulations[41,42], the theories of self-assembly are also gradually refined and developed, which lays a strong foundation for the applications of molecular self-assembly in various fields.

In recent studies, molecular self-assembly has been used in the fields such as high-performance batteries, cancer therapy and synthetic biology[43,44]. Li *et al.* reported a kind of flexible all-perovskite tandem solar cells, which achieves a more stable power conversion efficiency, showing the potential of self-assembly in enhancing energy conversion[45]. Tan *et al.* reported the enzymatic self-assemblies of thiophosphopeptides, which are used for selective cancer cell killing, and shows the potential of self-assembly for personalized medicine[46]. Liu *et al.* reported the Cu^{2+}-phenolic nanoflower designed to combat the fungi, which is prepared by coordination interaction, showing a potential of self-assembly for therapeutic strategy[47].

2. Au(111) Surface Structure

The Au(111) surface, representing the (111) crystallographic orientation of face-centred cubic (FCC) gold, is widely studied for its unique herringbone reconstruction[48], which contributes to enhance its stability and utility in various applications. Au(111) surface has low reactivity and high chemical stability, which makes it to be one of the most ideal substrates for catalysis, nanotechnology and surface molecular self-assembly[48].

2.1 Structural Details of Au(111) Surface

The Au(111) surface is characterized by its herringbone reconstruction, as shown in the STM image in **Figure 2.1** (b). The Au(111) reconstruction pattern shown as the zigzag herringbone stripes, which represents a periodic arrangement of alternating FCC and HCP stacking regions separated by discommensuration lines (brighter lines)[49]. The elbows within the herringbone stripes represent the regions of localized strain, and these elbow sites are usually the preferred initial binding sites for the other atoms and molecules deposited onto the Au(111) surface[50].

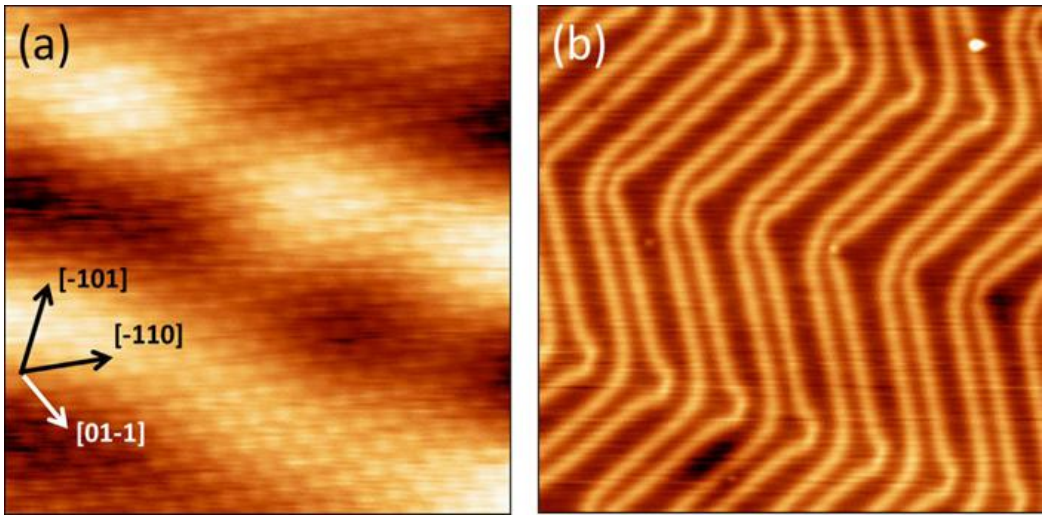

Figure 2.1 The STM image of Au(111) surface collected at 5 K. [51] (a) Atomically resolved image. Image size 5 × 5 nm^2. (b) Image size 50 × 50 nm^2.

The atomically resolved STM image in **Figure 2.1** (a) shows the arrangement of Au atoms in Au(111) surface, and the Au(111) lattice constant a is proved to be 2.88 Å[52]. Due to the unavoidable errors during the STM scanning process, such as the thermal drift, this lattice constant a is always used to correct the distances measured from the STM images.

The period of this reconstruction patten is measured to be 6.3 nm after the correction[49], which corresponds to 22 lattice sites of the substrate. However, it is found that there are 23 Au atoms fit into this limited region, which is then proved to be the reason causing the reconstruction on Au(111) surface. The illustration for the Au(111) 22×√3 reconstruction is shown in **Figure 2.2**.

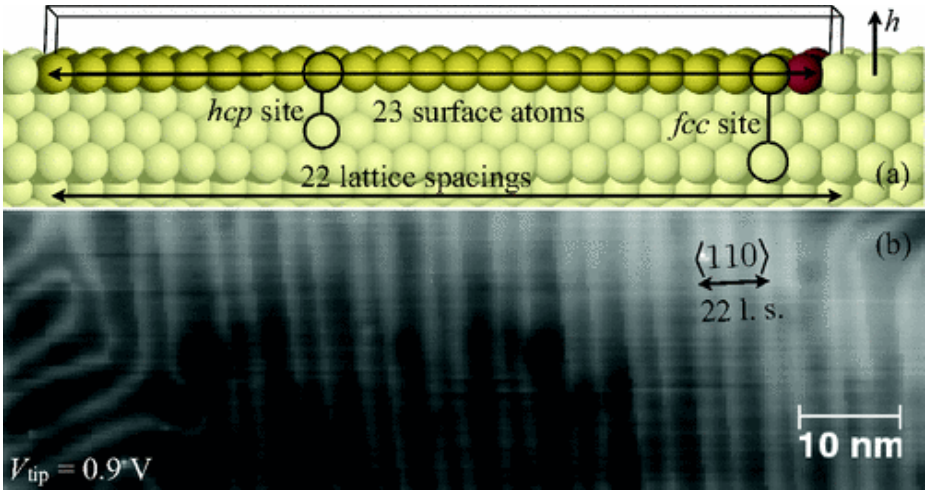

Figure 2.2 (a) The model of the Au(111) 22 × √3 reconstruction. This model shows how 23 Au atoms on the surface fit into 22 lattice sites by compressing the top layer of the surface with the additional atoms coloured dark red. The positions corresponding to lined-up FCC and HCP sites are indicated by the vertical lines. (b) STM image of the Au(111) herringbone reconstruction. [53]

In **Figure 2.2** (a), The basic unit cell is shown in the black rectangular frame, which is two atomic rows wide in the <112> direction and contains two extra atoms every 22 lattice spacings in the <110> surface direction. In the bulk, there are 44 Au atoms fit within the unit cell, while in the surface layer there are 46 Au atoms. These two more Au atoms at the surface then lead to a 4.5% compression in the <110> direction, which further creates alternating FCC and HCP regions, with widths of 38 Å and 28 Å respectively. And there is slight buckling between these two regions, where the atomic density is higher.

2.2 Formation of Herringbone Reconstruction on Au(111) Surface

The surface reconstruction is an important feature of transition metals, which is caused by the mismatching of the coordination number of atoms. Usually, the coordination number on the metal surfaces is lower than that in the bulk phase, leading to a tensile stress on the metal surface and a tendency for the surface to reconstruct and release the stress[54]. The reconstruction of Au(111) surface is also driven by such a force. The Au(111) reconstruction pattern can be considered as consisting of two parts: the stripes and the elbows. Thus, the formation of this herringbone pattern of Au(111) reconstruction can be regarded as a two-step process: i) The top layer densifies into the 22 × √3 stripe reconstruction by inserting an extra Au atom into an atomic chain in <110> direction

every 22 lattice constants. This densification creates a slight fluctuation on the surface of Au(111) surface, with a height of approximately 0.2 Å[49] on the surface. ii) The formation of stripe reconstruction mainly releases the tensile stress in Au top layer along the <110> direction. However, according to continuum elastic theory[55], this stripe reconstruction is not stable and will further reconstruct into a herringbone pattern with periodic stress domains. The details are shown in the **Figure 2.3**[48].

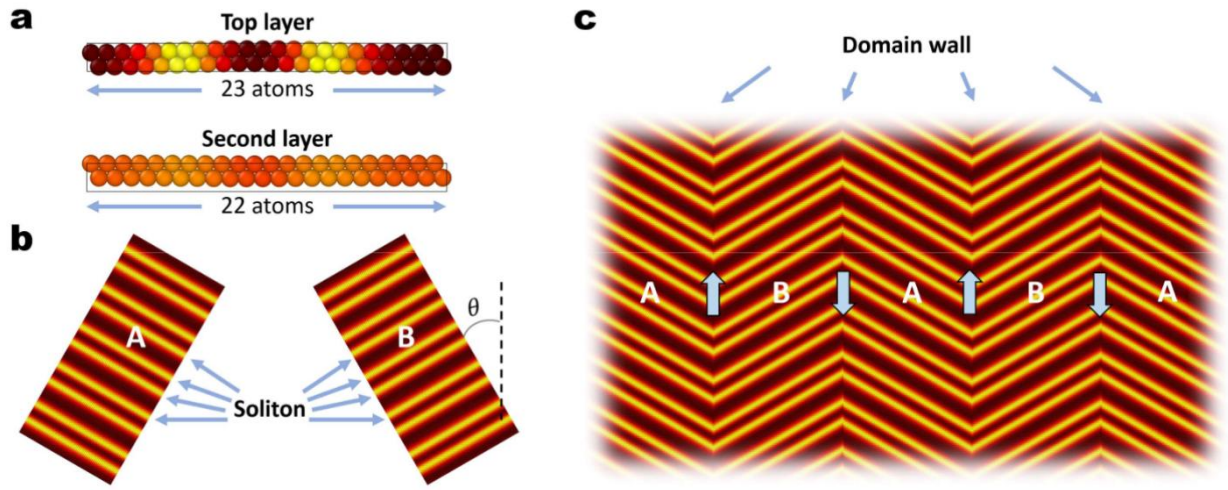

Figure 2.3 Illustration of the herringbone reconstruction on Au(111) surface. (a) Unit cell of the $22\times\sqrt{3}$ stripe reconstruction (top view). Colormap denotes the corrugation on the top layer where atoms on bridge sites are higher and are shown in brighter colours. (b) Stripe grains with different rotations. The brighter solitons consist of top-layer atoms located on bridge sites. (c) Rearrangement of stripe grains forming the herringbone pattern. Arrows on the domain walls denote the force density directions. [48]

Figure 2.3 (a) shows the arrangement of Au atoms in the top layer and the second layer respectively. The atoms filled in yellow in the top layer correspond to the bright stripes on Au(111) surface, representing the positions of discommensuration lines, which are the boundaries of FCC and HCP regions. On the second layer, with no extra Au atom filling in the space, the Au atoms remain their arrangements in FCC stacking[56]. In **Figure 2.3** (b), two regions of reconstruction stripes have the different orientations, and that is caused by the rotational symmetry of (111) oriented plane. Due to the HCP arrangement of gold atoms in the (111) plane, this surface has a three-fold rotational symmetry. This symmetry allows the surface to reconstruct along three equivalent crystallographic

directions, specifically the <110> directions (or the equivalent directions in the surface plane). These directions correspond to the close-packed rows of Au atoms, which are rotated 120° relative to each other. As a result, the reconstruction stripes can align along any of these three directions, leading to domains with different stripe orientations, as the domains A and B shown in **Figure 2.3** (b). Then, a stress domain would appear at the boundaries of these stripe domains, and the force density directions are corresponding to the orientations of the stripes, as shown in **Figure 2.3** (c).

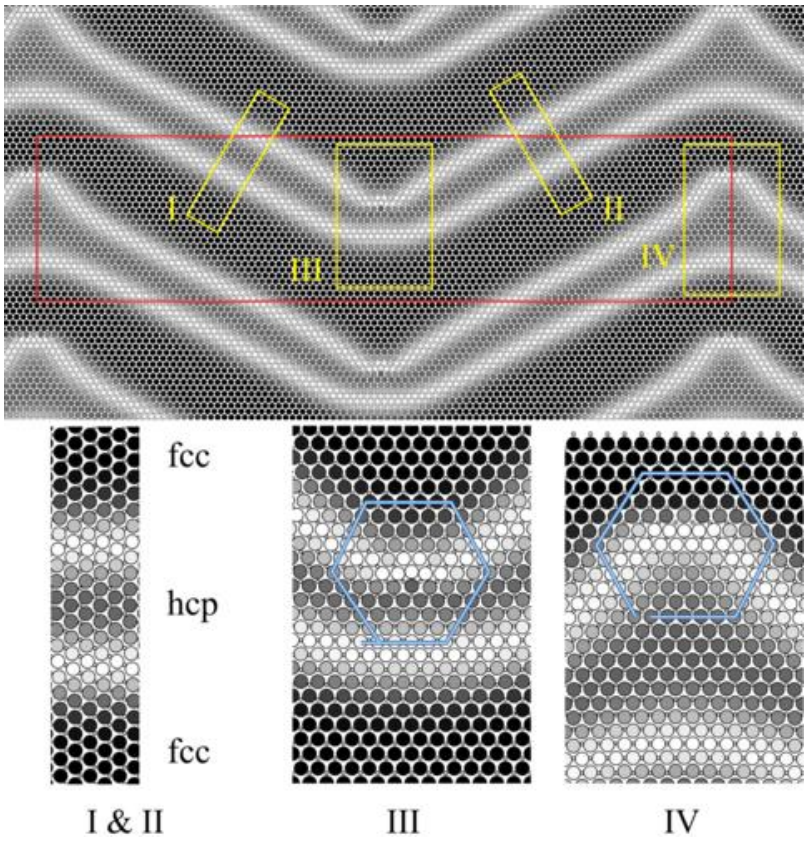

Figure 2.4 Schematic of the herringbone reconstruction. Regions I and II are two rotationally equivalent domains of the 22 × √3 stripe phase. Regions III and IV are two types of threading edge dislocations. [57]

The details of the arrangement of Au atoms at the elbow sites are shown in **Figure 2.4**. The transformation from the stripe pattern (regions I and II) to the herringbone pattern (regions III and IV) is attributed to the fact that the stripe pattern is more anisotropic and thus mainly allows the stress relaxation along one direction on Au(111) surface. While the formation of the herringbone pattern, of which the arrangement is more isotropic, allows the relaxation of the stress in another

direction, and the system energy is thus lower[48]. According to the calculations reported by Li *et al.*, with the formation of the herringbone reconstruction, the tensile stress is reduced by about 26% from that of the pristine Au(111) surface. Though the herringbone reconstruction cannot reduce the Au(111) surface stress to near zero either, it is still a more stable structure compared with the stripe reconstruction. The formation of the herringbone reconstruction is highly sensitive to the strain applied to the surface. By applying a tensile or compressive strain to the Au(111) surface, the reconstruction pattern can be changed. When the magnitude of the applied strain becomes over 0.2%, the herringbone reconstruction will be replaced by the stripe reconstruction.

3. Decanethiol Self-Assembly on Au (111)

Decanethiol ($C_{10}H_{22}S$, DT) is a straight-chain alkanethiol with a ten-carbon alkane chain and a thiol (-SH) functional group. It is a colourless to pale yellow liquid with a strong odour, which is commonly used in self-assembled monolayers (SAMs) on metal surfaces like gold for nanotechnology and surface chemistry applications.

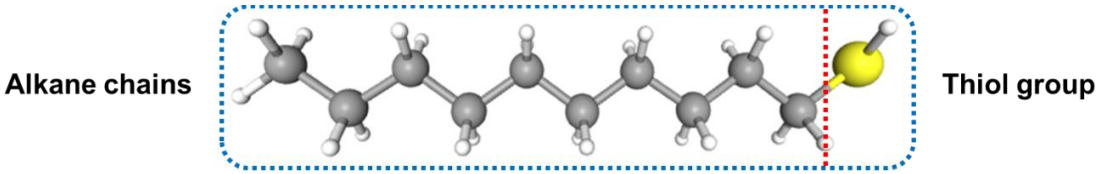

Figure 2.5 The ball-stick model for DT molecules

The model for DT molecule is shown in **Figure 2.5**. In this model, the sulfur atom is in yellow, the carbon atoms are in grey and hydrogen atoms are in white. The right half of this model is the thiol (-SH) group of DT, which enables a strong binding to surfaces. And the left half is the long hydrocarbon chain, which provides hydrophobic properties (van der Waals interaction).

3.1 Decanethiol Self-Assembled Monolayer on Au(111) Surface

3.1.1 Formation and Structural Detail

The self-assembly of alkanethiol molecules has been widely studied for its ability to form highly organized SAMs on the Au(111) surface. Sulfur have a strong affinity to transition metal surfaces[58-60], and they are able to form multiple bonds with surface metal clusters[61]. The formation of DT SAMs starts from the rapid formation of S-Au bond with the sulfur head group (-SH) attaching to

the Au(111) surface[62,63], with a bond dissociation energy of ~ 40-50 kcal/mol, significantly stronger than physisorption (~ 5-10 kcal/mol) but weaker than Au-Au bonds (~ 60 kcal/mol), allowing adsorbed molecules to diffuse across the surface to minimize defects during assembly[64]. This chemisorption involves electron donation from the lone-pair orbitals of sulfur to conduction band of gold, forming a polarized thiolate bond (R-S-Au), as confirmed by X-ray photoelectron spectroscopy (XPS) showing S 2p peaks at ~162 eV, distinct from free thiols (~ 163-164 eV)[65]. This chemisorption occurs within seconds to minutes, which depends on the concentration of DT solution[66]. After the chemisorption, the disordered DT molecules are then driven by the van der Waals interaction among alkane chains, adjusting their arrangement and gradually occupying their preferred sites of Au(111) substrate. And this process would last for hours or days. Finally, most of the DT molecules transfer from the disordered phase to close-packed φ phase on Au(111) surface. The STM image of the close-packed φ phase DT is shown in **Figure 2.6** (a).

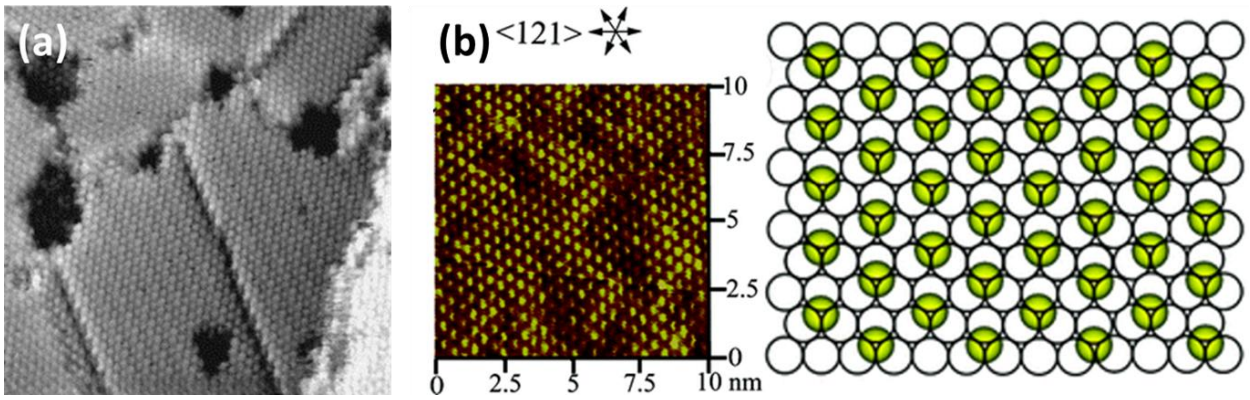

Figure 2.6 (a) The STM image of a 250 Å × 250 Å area of the close-packed φ phase DT.[67] (b) Higher-resolution STM image of decanethiol molecules adsorbed on Au(111) surface. The structural model for the ordered adlayer of decanethiol molecules adsorbed on Au(111) is shown on the right.[68]

The arrangement of DT molecules is shown in **Figure 2.6** (b). The DT molecules are found to form into a ($\sqrt{3} \times \sqrt{3}R30°$) adlayer structure on Au(111) surface[69], which means that the sulfur atoms from the DT molecules bind to the Au(111) surface in a pattern that repeats every $\sqrt{3}$ times the lattice constant of gold ($\sqrt{3}a \approx 0.499$ nm) and is rotated by 30°, leading to a close-packed and stable monolayer. The standard $(\sqrt{3}\times\sqrt{3})R30°$ alkanethiol SAM on Au(111) is found to consist of domains

with Au-adatom-alkanethiolate occupying the FCC hollows site, alongside domains where the hcp hollow site is occupied[70]. The coverage of DT in this arrangement is calculated to be 0.33 ML[71].

For the alkane chains of DT in this close-packed phase, they are not standing vertically on the Au(111) surface, but tilting with an angle of approximately 30° off the surface normal[72,73]. The appearance of this tilt angle of DT alkane chains arises from a combination of molecular interactions and structural properties. Firstly, the tilting allows the alkane chains to pack more efficiently, which enhances the van der Waals interactions between neighbouring DT molecules. And this dense packing further contributes to the stability of the DT monolayer. Secondly, the tilt facilitates alignment of the alkane chains with the lattice of Au(111) substrate, accommodating the $(\sqrt{3} \times \sqrt{3})R30°$ superstructure observed in these systems[74]. Thus, the tilt angles for the alkane chains within different alkanethiol SAMs are different, which is due to the variations in the density of their head groups. A higher density of the head groups may lead to a smaller tilt angle due to limitation of the space, while a lower density allows for a larger tilt angle[75]. Similarly, the tilt angle for the same kind of alkanethiol in different phase are also different, which leads to a large uncertainty for analysing the behaviour of the alkane chains in lower coverage phases.

3.1.2 Electrical and Thermal Features

The charge conductivity of the DT SAMs on metal surface is generally found to be low[76], which is due to the large HOMO-LUMO gap (~ 10 eV) of the alkane chains, and that makes the charge transport occurring primarily via the tunnelling[77-80]. Due to the low conductance of alkane chains, the signals of DT we observed from STM images, such as in **Figure 6.2** (a), are mainly contributed by the terminal ($-CH_3$) groups of the alkane chains[81]. These groups are positioned at the outermost surface of the monolayer, making them the closest to the STM tip and most accessible for electron tunnelling. Thus, the signals from the STM images of DT SAMs actually reflect the positions of the terminal groups rather than the positions of S-Au bonds. Meanwhile, the low conductance of DT could also lead to the inaccurate height information from the STM data. For example, when C_{60} and DT molecules coexist on the Au(111) surface, the height profile shows that the C_{60} molecules are about 0.25 nm higher than DT molecules. However, the true heights of C_{60} and DT are respectively 0.71 nm[82] and the 1.32 nm[83]. Though the DT molecules are almost twice longer than the C_{60} molecules, due to a relatively large difference in their conductivities, the DT molecules look even about 0.25 nm shorter than the C_{60} molecules.

The thermal stability of the DT SAMs on Au(111) is mainly attributed to the thermal cleavage of the S-Au bond. As the temperature of sample increases, the thermal energy can overcome the binding energy of the S-Au bond[84,85], leading to desorption of the thiol molecules. The desorption temperature of DT on Au(111) surface is around 380 K - 400 K[86-88]. According to the different binding sites of DT in different phases, the desorption temperature of DT varies. In addition, the thermal stability can be affected by the chain length and packing density. The alkanethiol with longer chains like decanethiol show enhanced stability due to the stronger van der Waals interactions, which delays their desorption compared to shorter thiols.

3.2 δ Phase Decanethiol on Au(111) Surface

3.2.1 Au-Adatom-Decanethiolate Model

DT molecules have been observed to form various self-assembled phases on Au(111) surface, and the formation of these ordered phases is strongly related to the coverage of DT[74]. The coverage of DT can be adjusted through the thermal annealing of the sample. During the thermal annealing, some of the DT molecules desorb from the surface, and the rest of the DT molecules rearrange and absorb on the surface. Each two S atoms bind with an Au adatom, and finally reform into the Au–adatom–decanethiolate (AAD)[89], which is also represented as RS-Au-SR (R = $CH_3(CH_2)_9$) staples. The model for the RS-Au-SR staple is shown in **Figure 2.7**.

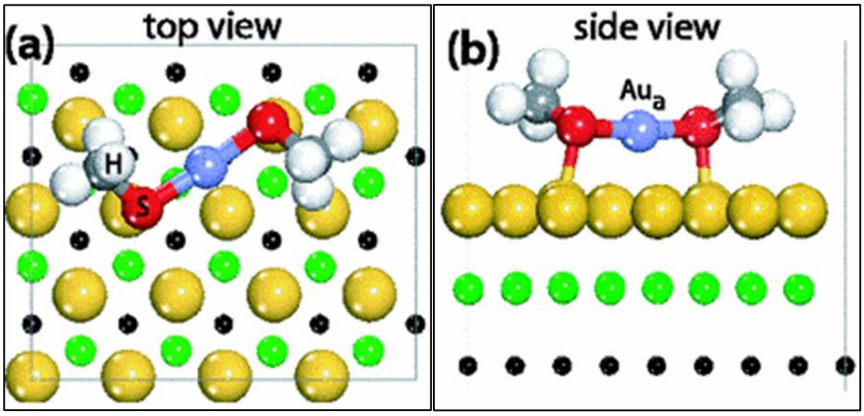

Figure 2.7 (a) Structural model showing the details of the RS-Au-SR staple and how it is attached to the Au(111) substrate. (a) The top view. (b) The side view. The Au adatom (in blue) is located at the bridge site between two substrate Au atoms (in yellow) on the top layer. The two S atoms (in red) sit almost directly above the substrate Au atoms.[90]

In this model, the Au adatom occupies the two-fold bridge site of the Au(111) substrate, and the S atom of RS makes one bond to the Au adatom and one bond to the underlying lattice Au atom, which stabilises the whole DT molecule on the Au(111) substrate. The bond length of S-Au-adatom is 2.33 Å and the bond length of S-Au-lattice is 2.49 Å[90]. Through the formation of this AAD unit, the binding energy of the RS on Au(111) surface is increased[91-93], and thus the DT molecules are more stably fixed on the surface even the coverage of DT dropped.

The existence of Au adatoms in the self-assembled alkanethiol films on Au(111) surfaces has been proved in previous works[94,95]. However, due to the low charge conductivity of alkane chains, these Au adatoms are not visible in the STM images, which leads to an uncertainty in the position of the Au adatoms, especially in the low coverage phase of long chain alkanethiols. For the long chain alkanethiols such as DT in close-packed phase, since the arrangement of DT is strongly compatible with the Au(111) surface, and the DT alkane chains remain in a specific angle off the surface plane[73], it is easier to determine the binding sites of DT. While for the DT in a lower coverage phase, with less DT molecules occupying on the surface, there are relatively larger space for DT alkane chains to lie down, bend or stack[96], and there is also more available binding sites for DT to occupy. And that makes it possible for different alkane chains having different tilt angles, thus the signals from the terminal groups of DT alkane chains may not reflect the true binding sites of DT. Though we can still come up with the reasonable arrangement of DT by analysing the binding energy of different sites and the stability of the overall structure, the complex van der Waals interactions among the alkane chains still introduce uncertainty into the results. Although the positions of the AAD units within the low coverage ordered DT phases are hard to be confirmed, the model of the AAD unit has been supported by some following works[97,98].

3.2.2 Structure of δ Phase Decanethiol on Au(111) Surface

After the thermal annealing, the DT molecules on Au(111) surface transfer from the close-packed φ phase into various of other ordered phases, as shown in **Figure 2.8** (a). Usually, with the decrease of the DT coverage, the ordered phases change in sequence: i) δ phase (zigzag meshed phase); ii) χ phase (alternating stripe phase); iii) β phase (stripe phase); iv) α phase (liquid phase)[99]. Due to the tiny but unavoidable temperature difference of the sample during thermal annealing, these ordered phases are found always to coexist on the Au(111) surface. If the DT/Au(111) sample is annealed at a lower heating rate, the DT molecules on the Au(111) surface will be more likely to

form a uniform and consistent phase. Among these ordered phases, the δ phase is considered to have the highest DT coverage[74,100]. The STM image of δ phase DT is shown in **Figure 2.8** (b). In this region, the δ phase DT coexists with the φ phase DT, and the δ phase DT grows in the direction parallel to the $[11\bar{2}]$ direction and the other two equivalent directions[74].

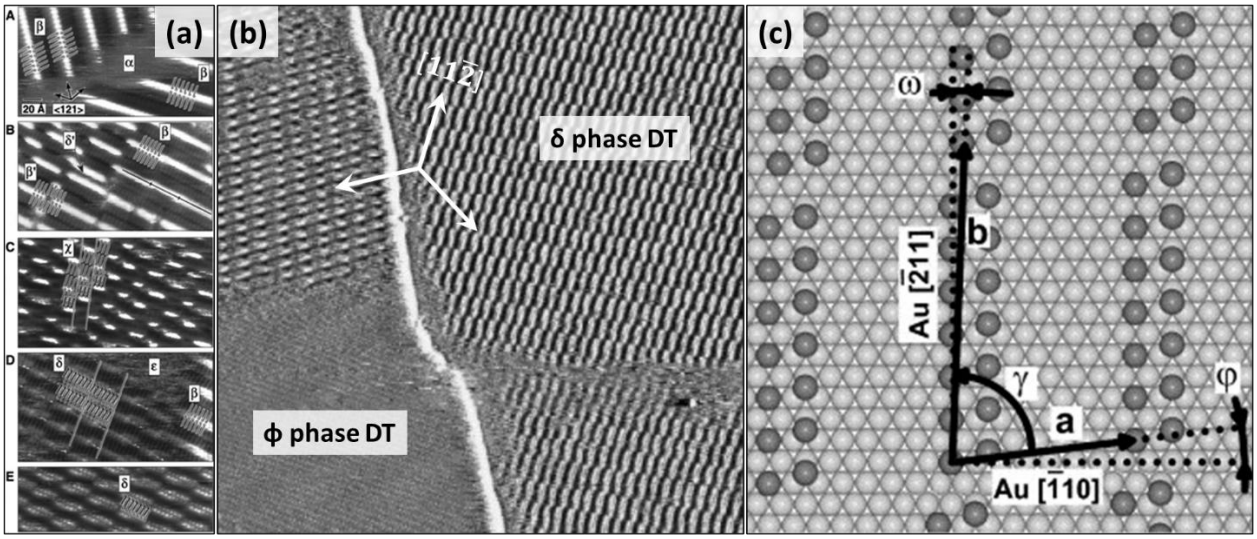

Figure 2.8 (a) Various of ordered phases of DT observed from the Au(111) surface.[99] (b) The STM image of the δ phase DT on Au(111) surface. (c) The model showing the positions of the terminal groups of DT alkane chains relative to the Au(111) substrate.[74]

The model of δ phase DT is shown in **Figure 2.8** (c). The darker grey spheres shows the positions of the terminal groups of DT alkane chains, rather than the positions of the DT binding sites, as previously discussed. The distances and angles in this δ phase DT model are: a = 2.18 nm, b = 3.75 nm, α = 81.2°, v = 6.6° and ω = 2.2°. And the distance of two neighbouring DT terminal group rows is 2.16 nm (≈ 7.5a)[99,101]. The local coverage of DT in δ phase is calculated to be 0.23 ML. The DT molecules in this phase are deduced to bind with the Au(111) surface through forming the AAD units. While due to the mobility of the DT alkane chains, there is the uncertainty of the true binding sites of the AAD units. On the other hand, the mobility of the DT alkane chains makes it easier for the other added molecules, such as C_{60} fullerene molecules, to drop onto the Au(111) substrate, rather than be held on the top of the DT alkane chains. And that enable the added molecules to interact more effectively with the DT alkane chains, which makes the δ phase DT/Au(111) sample an ideal template for the studies of bicomponent and multicomponent supramolecular self-assembly[102,103].

4. C_{70} and C_{60} Fullerenes

C_{60} and C_{70} fullerenes are carbon-based molecules belonging to the fullerene family, which were discovered by Kroto *et al.* in 1985[104]. After several years of research on the fullerenes, Krätschmer *et al.* reported the preparation method of C_{60} fullerene in 1990[105], and then Diederich *et al.* reported the preparation method of C_{70} fullerene in 1992[106]. Since then, fullerene molecules have been widely studied and applied in various fields, such as nanotechnology (e.g. molecular cages for drug delivery), organic electronics (e.g. solar cells), and superconductivity research.

4.1 Structural Detail and Properties of C_{70} and C_{60} Molecules

4.1.1 C_{60} Fullerene

The C_{60} fullerene molecule consists of 60 carbon atoms arranged in 20 hexagonal rings and 12 pentagonal rings, with each carbon atom bonded to three others, forming a closed cage[104], as shown in **Figure 2.9** (a). This arrangement ensures that no pentagonal rings share an edge, which minimizes the structural strain and enhances stability. C_{60} fullerene has the icosahedral symmetry (I_h), which is the highest possible symmetry for molecules, and it is characterized by two-fold, three-fold, and five-fold rotational axes. This high symmetry arises from the geometric arrangement of its pentagonal and hexagonal rings. The nucleus-to-nucleus diameter of the C_{60} is 0.707 nm[107]. And the van der Waals diameter of C_{60} is approximately 1.0 nm, which is determined by accounting for the electron cloud surrounding the molecule[108].

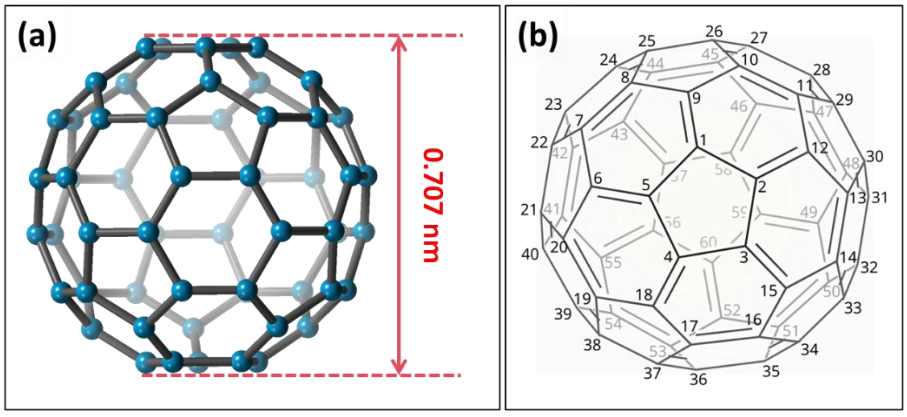

Figure 2.9 (a) Structure of C_{60} fullerene. (b) The details of the carbon atoms and the C-C bonds within the C_{60} fullerene.

As shown in **Figure 2.9** (b), there are two different types of C-C bonds within the C_{60} molecules. i) 6:6 ring bond (between two hexagonal rings). This type of bond is C-C double bond with a length of approximately 1.401 Å. ii) 6:5 ring bond (between a hexagonal and a pentagonal ring). This type of bond is C-C single bond with the bond length of approximately 1.458 Å[109,110]. And the bond energies of both types of C-C bonds have been reported in previous work[111,112]. The carbon atoms within the C_{60} molecule are sp^2 hybridized[113]. The isolated C_{60} in gas phase shows a HOMO-LUMO gap of 4.9 eV[114].

4.1.2 C_{70} Fullerene

The C_{70} fullerene molecule consists of 70 carbon atoms arranged in 25 hexagonal rings and 12 pentagonal rings[115]. C_{70} fullerene has D_{5h} symmetry, which is lower than the I_h symmetry of C_{60}. The D_{5h} point group reflects the ellipsoid-like structure, with a five-fold rotational axis along the long axis and a mirror plane perpendicular to it. This reduced symmetry results from the additional 10 carbon atoms forming an equatorial belt, which breaks the high symmetry of C_{60}. The D_{5h} symmetry influences the electronic and optical properties of C_{70}, contributing to a more complex electronic structure compared to C_{60}. **Figure 2.10** (a) and (b) show the side and top view of the C_{70} fullerene. C_{70} has a long axis, which is 0.791 nm, and a short axis, which is 0.710 nm[116]. The van der Waals diameter of C_{70} is approximately 1.1 nm, which is slightly larger than that of C_{60}[117].

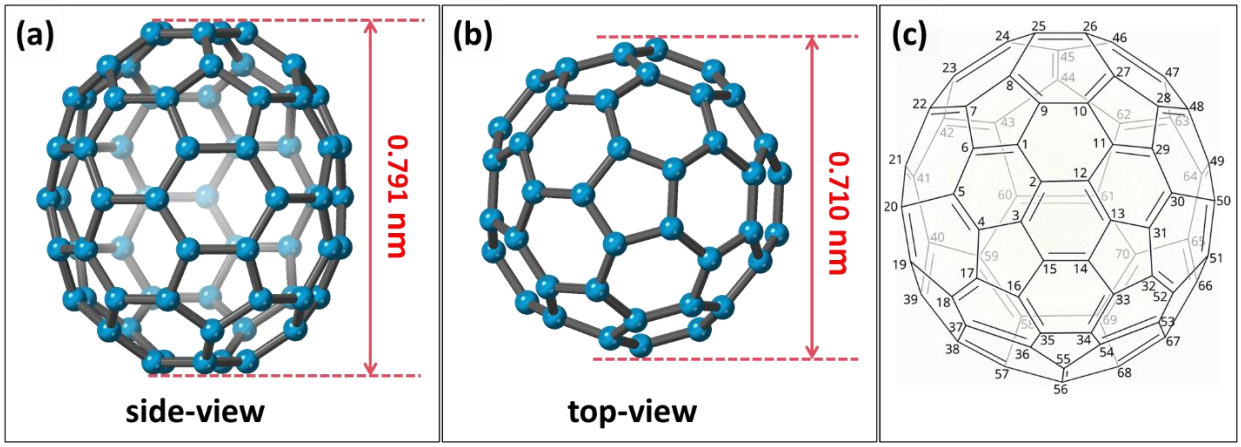

Figure 2.10 (a) The side view of C_{70} fullerene. (b) The top view of C_{70} fullerene. (c) The details of the carbon atoms and the C-C bonds within the C_{70} fullerene.

As shown in **Figure 2.10** (c), C_{70} is also consisted with 6:6 C-C double bonds and 6:5 C-C single bonds. However, due to the lower symmetry, the C_{70} fullerene has eight bond lengths ranging between 0.137 and 0.146 nm[118]. The HOMO-LUMO gap of C_{70} is measured to be 1.72 eV[119-121].

4.2 Molecular Orientations of C_{60} and C_{70} Molecules

The self-assembly of fullerenes on metal surface (Au(110), Ag(111), Pt(110), etc.) has been widely studied[122-125]. Research have indicated that at RT, the fullerene molecules keep rotating on the surface before reaching thermal equilibrium[126], and this rotation gradually slows down and eventually stops when the temperature of the sample decreases to 90 K[127]. According to the different binding sites of the fullerene molecules, they are stabilised on the surface in several specific molecular orientations, showing different intramolecular patterns, which are found to be consistent with the simulation results in various fullerene-metal self-assembly systems.

4.2.1 Molecular Orientations of C_{60} Molecule

C_{60}, due to its high symmetry, is the most commonly used fullerene in the studies of molecular orientations[128,129]. **Figure 2.11** (a) shows the molecular orientations of C_{60} within the C_{60} monolayers on Au(111) surface reported by Schull *et al*. The bright parts in the STM images correspond to the pentagonal rings of C_{60} molecules, which are known to be electron deficient[127]. And this can be explained with the excess LDOS in the empty-state level at pentagonal rings which consist of five sp^2 bonds. Thus, according to the one, two, or threefold symmetry axis shown in (a), it is easy to find the corresponding orientations with a molecular model. This method is also applicable to the analysis of the molecular orientations of other fullerenes.

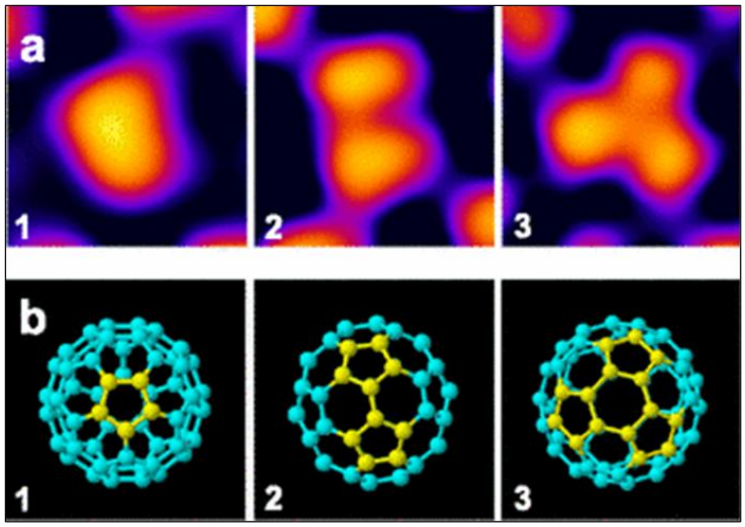

Figure 2.11 (a) The STM images showing the C_{60} molecules in three molecular orientations on Au(111) surface at 5.7 K. (b) Corresponding top view models. Pentagonal rings are highlighted in yellow in the models because they appear high in STM images at positive bias.[130]

Figure 2.11 (b) shows the C_{60} models corresponding to the LT STM images in specific molecular orientations and directions on Au(111) surface. The C_{60} are respectively in 1) pentagonal ring facing up; 2) 6:6 C-C bond facing up; 3) hexagonal ring facing up molecular orientations. It can be noticed that once the corresponding molecular orientations of C_{60} are matched, the direction in which these molecules bind to the substrate is determined as well, which can provide us with useful information when constructing complex models such as supramolecular frameworks.

In addition, more possible molecular orientations are proposed through the STM simulation, as reported by Wang *et al*[127,131]. In **Figure 2.12**, except for the three orientations observed in **Figure 2.11** (a), there are two more orientations have not been observed in this multilayer C_{60}/Au(111) system, which indicates that the molecular orientations that are also related to the interactions between the substrate and the added molecules. And the appearance of different orientations may require different conditions (binding sites, intermolecular interactions, etc). To acquire the accurate binding energy of the molecules, the interactions of the molecules and the surface need to be considered thoroughly.

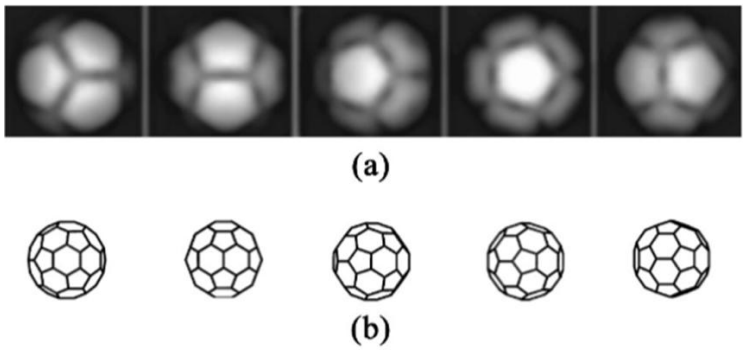

Figure 2.12 (a) Simulated empty-state STM images of a free C_{60} molecule with five types of high-symmetry rotational orientations corresponding to (b) schematic diagrams of C_{60} with a hexagon, a 6:6 bond, a 5:6 bond, a pentagon, and an atop atom facing up, respectively, from left to right.[127]

4.2.2 Molecular Orientations of C_{70} Molecule

Similarly, the C_{70} molecules are also able to bind with the substrate in different molecular orientations. However, the C_{70} molecules, as discussed previously, are less symmetric than C_{60}, which makes the possible binding types of C_{70} in different molecular orientations relatively limited. Niu *et al.* reported the C_{70} deposited on the CuSe monolayer[133], revealing the molecular orientations of C_{70} and providing the STM simulation from DFT calculations for all the other possible adsorption configurations of C_{70} on CuSe monolayer, as shown in **Figure 2.13**. **Figure 2.13** (a) shows the two different orientations of C_{70}, and the corresponding models and STM simulations are shown in **Figure 2.13** (b). C_{70} are found respectively in 1) C atom facing up; 2) 6:6 C-C bond facing up molecular orientation, and C_{70} are both lying down with their long axes parallel to the surface plane. The C_{70} in lying down orientation has been reported have be a more stable adsorption than in standing up orientation[132].

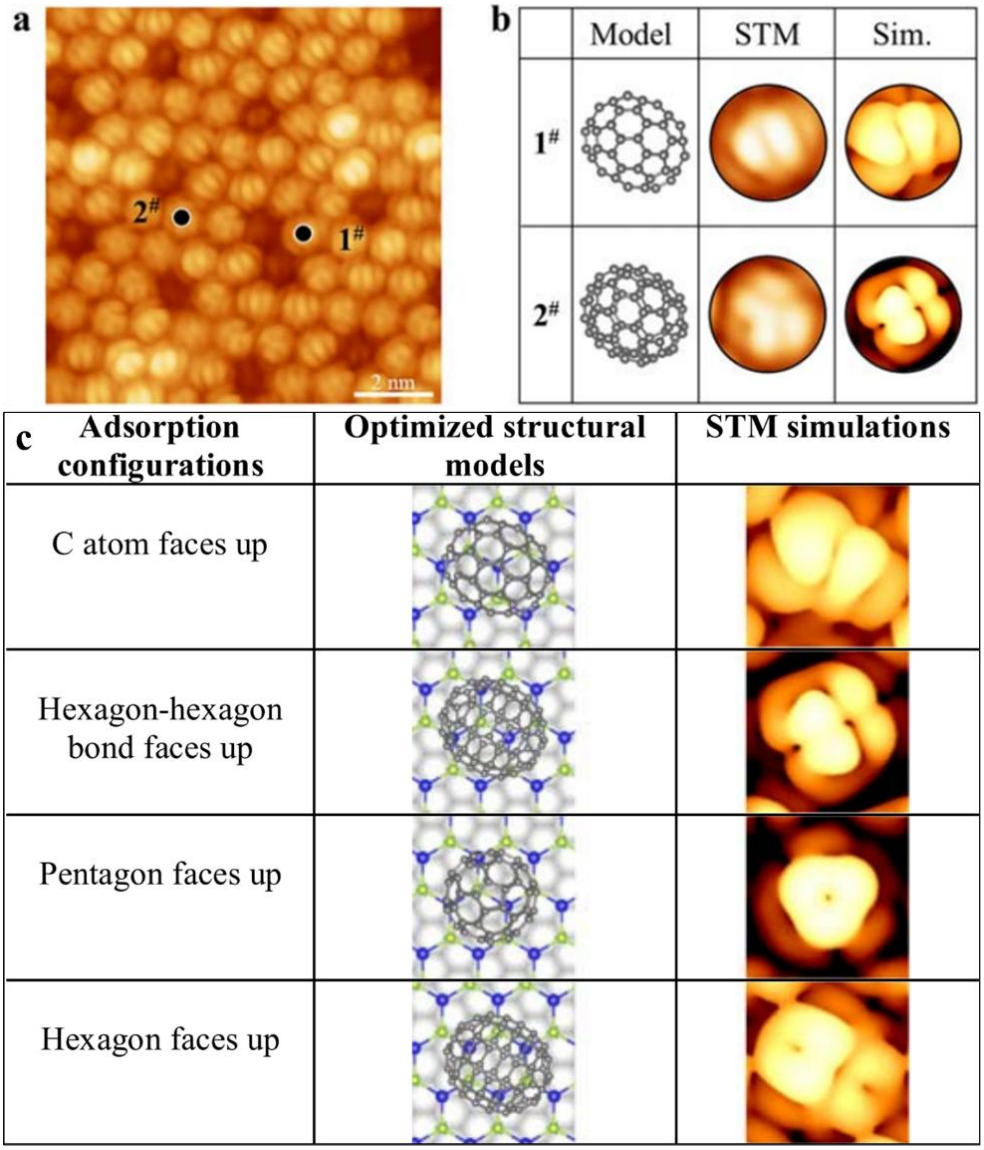

Figure 2.13 (a) The STM image showing the molecular orientations of C_{70} on the CuSe monolayer. (b) Two possible adsorption geometries and calculation models corresponding to the C_{70} molecules in (a). (c) The STM simulation of the possible molecular orientation of C_{70} on CuSe monolayer.[133]

Figure 2.13 (c) shows the four possible molecular orientations of C_{70} absorbing to the surface. According to Niu *et al.*'s calculation[133], the two molecular orientations of C_{70} shown in **Figure 2.13** (b) are the two lowest energy C_{70} configurations in this system. For the other adsorption configurations of C_{70}, they could be more stable in other systems, which needs to be further proved.

4.3 Self-Assembled Monolayer of C_{60} and C_{70} on Au(111) Surface

4.3.1 C_{60} Monolayer on Au(111) Surface

The C_{60} monolayer on Au(111) surface has been well studied[134,135], and the first monolayer is known to have several phases, respectively the in phase, $2\sqrt{3} \times 2\sqrt{3}$ R30° and R14°[136-138]. And that depends on how the direction of close-packed C_{60} related to the close-packing direction of the Au atom on the Au(111) surface. Altman and Colton first reported the in phase structure and the $2\sqrt{3} \times 2\sqrt{3}$ R30° structure of the C_{60} monolayer on Au(111) surface[139]. Then the R14° structure was reported by Tzeng *et al*[140].

The feature of in phase structure is that the close packing direction of the C_{60} molecules matches with the $[1\bar{1}0]$ direction or the other two equivalent direction of the Au(111) substrate, which is also the direction of close-packed Au atoms, as shown in **Figure 2.14** (d). The feature of the $2\sqrt{3} \times 2\sqrt{3}$ R30° structure is that there is an angle of 30° between the close-packing directions of C_{60} and Au atoms, and the arrangement of C_{60} is commensurate with the unreconstructed Au(111) surface, as shown in **Figure 2.14** (e). The distance of two neighbouring C_{60} is about 1 nm ($2\sqrt{3}a$, a = 0.288 nm). The feature of the R14° structure is that the closed packed C_{60} layer rotated by ± 14° from the in-phase structure. The nearest distance of the neighbour C_{60} molecules according to the model in **Figure 2.14** (f) is 1.039 nm, which is larger compared to the preferred spacing of 1.002 nm. Thus there would be a tensile stress within the C_{60} monolayer in this structure, and the Au atoms at the C_{60}/Au(111) interface have to reorganize to reduce this stress. Overall, though the C_{60} monolayer in different phases looks always keep the hexagonally packed structure, the arrangement of Au atoms at the interface have adjusted to stabilise the C_{60} monolayer.

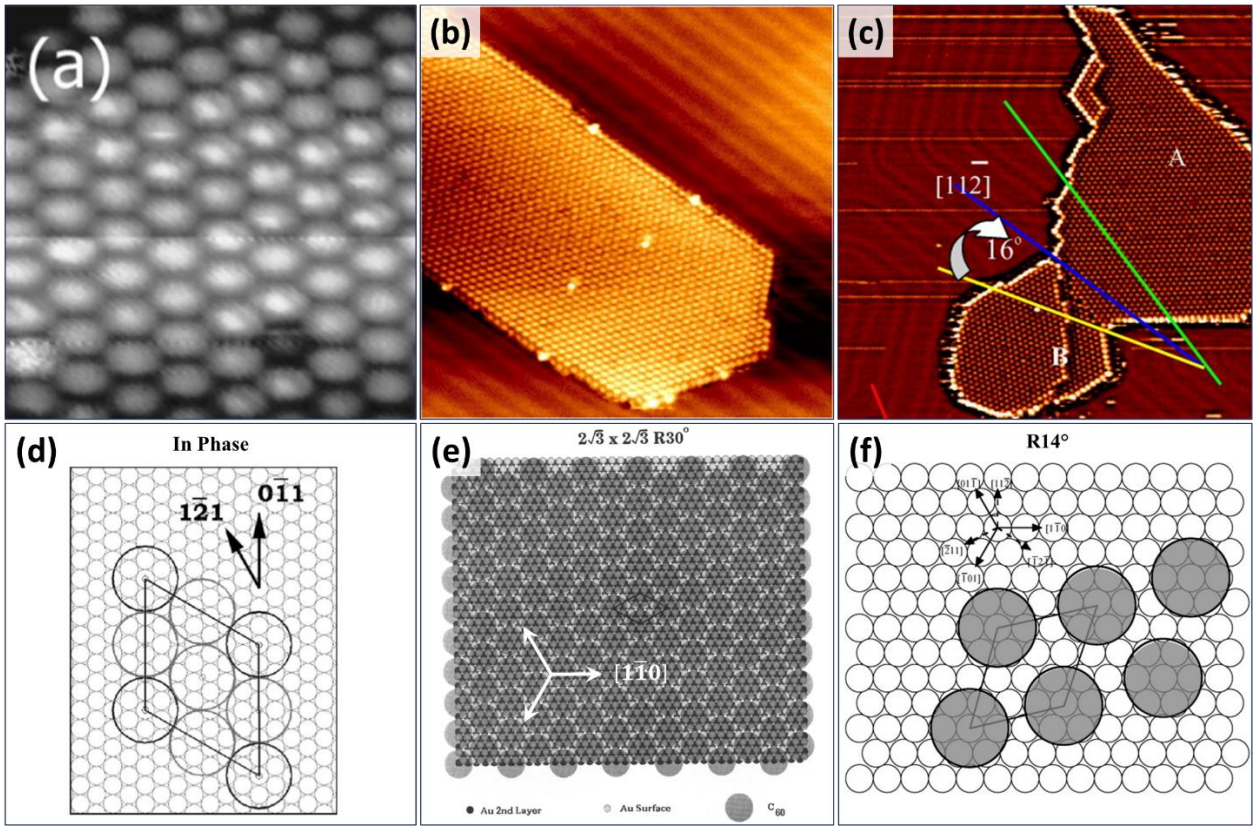

Figure 2.14 The C_{60} monolayer in three different phases on Au(111) surface. (a) STM image of in phase structure of the C_{60} monolayer.[141] (b) STM image of $2\sqrt{3} \times 2\sqrt{3}$ R30° structure of the C_{60} monolayer.[137] (c) STM image of R14° structure of the C_{60} monolayer.[137] (d)[141], (e)[134] and (f)[137] show the corresponding illustrations for (a), (b) and (c).

For the C_{60} monolayer on Au(111) surface, the HOMO-LUMO gap is proved to be 2.7 ± 0.2 eV[114]. As for the thermal stability of the C_{60} monolayer, the C_{60} will desorb from the substrate at the temperatures above 300 – 400 °C in UHV conditions[142,143], and the monolayer would then be broken.

4.3.2 C_{70} Monolayer on Au(111) Surface

The C_{70} monolayer on various of surfaces have been studied[144-147]. However, compared with the monolayer of C_{60}, much less attention has been paid to C_{70} monolayers, which present a greater variety of morphologies and related properties than C_{60} as its molecular symmetry drops from I_h to D_h. In the previous works, C_{70} have been observed to form into the close-packed hexagonal and quasi hexagonal lattice on the three-fold symmetry metal surface. Katsonis *et al.* reported the C_{70}

sub-monolayer on the n-tetradecane/Au(111) surface, revealing the two types of C_{70} close-packing, as shown in **Figure 2.15**. According to the ellipsoidal like shape of C_{70}, the α-type packing and β-type packing respectively correspond to the close-packed phase form with the C_{70} in standing up orientation and in lying down orientation[148]. In **Figure 2.15** (a), the C_{70} in α domain have the nearest neighbouring distance of 1.06 nm, and they are deduced to occupy the three-fold sites of Au(111) surface, so that the C_{70} monolayer forms into a $2\sqrt{3} \times 2\sqrt{3}$ R30° structure, which is similar with the C_{60} monolayer[137]. For the C_{70} in β domain, they arrange in the direction parallel to the $[1\bar{1}0]$ direction, and it is similar with the in phase structure of C_{60} monolayer on Au(111) surface[141]. And the nearest neighbouring distance along the $[1\bar{1}0]$ direction is 1.20 nm. In addition, the lengths of the C_{70} in α and β domains are measured to be 1.1 ± 0.1 nm and 1.3 ± 0.1 nm respectively, which matches with the previous observation of C_{70} with STM[149]. Thus, the models of α and β type close-packing with C_{70} in different molecular orientations are built in **Figure 2.15** (b).

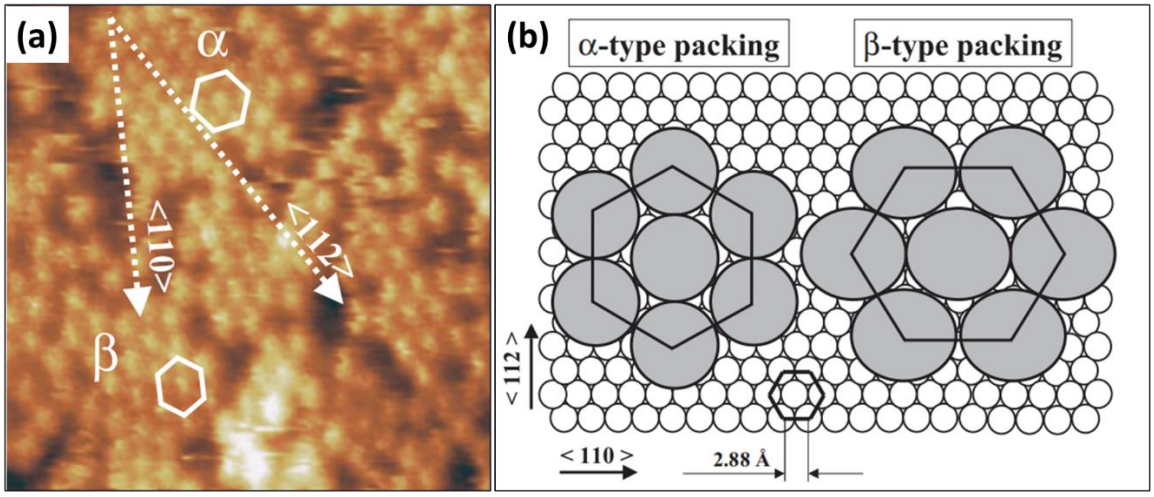

Figure 2.15 (a) The STM image (25 nm × 25 nm, V_t = + 0.2 V, I = 100 pA) showing the coexistence of two types of C_{70} close-packed phase on surface. In the α-domain, hexagonal close-packed molecular rows are aligned along the <112> direction; in the β-domains, the C_{70} rows are aligned along <110> direction.[148] (b) Schematic representation of two C_{70} packing modes on Au(111) surface: Left: $2\sqrt{3} \times 2\sqrt{3}$ R30° structure of α domains. Right: in phase structure of the b-domains.[148]

However, there is no long-range ordered C_{70} in any of these two packing type, and this can be explained by the formation of misfit dislocations between molecular rows and the Au(111) lattice along the <110> and <112> directions. In addition, the interaction between free C_{70} and Au(111)

substrate is relatively week[150], and the Au atoms at the C_{70}/Au(111) interface are not effectively driven to change their arrangements.

The desorption temperature of C_{70} is proved to be 467 °C[151]. And due to the weaker molecule-surface interaction, the thermal stability of the C_{70} monolayer on Au(111) surface is dominated by the properties of C_{70} itself.

5. Van der Waals Force in C_{60}/C_{70}-Decanethiol Systems

Van der Waals forces, specifically London dispersion forces, are weak intermolecular forces that arise from temporary, induced dipoles in molecules, even those that are nonpolar. These forces, named after Johannes Diderik van der Waals, who incorporated them into his equation for real gases[152], are a subset of van der Waals forces, distinct from dipole-dipole interactions and hydrogen bonding. London dispersion forces are universal, occurring in all molecules regardless of polarity, and are critical in processes such as gas condensation, the physical properties of liquids and solids (e.g., boiling and melting points), and the behaviour of nonpolar substances like hydrocarbons or noble gases[153].

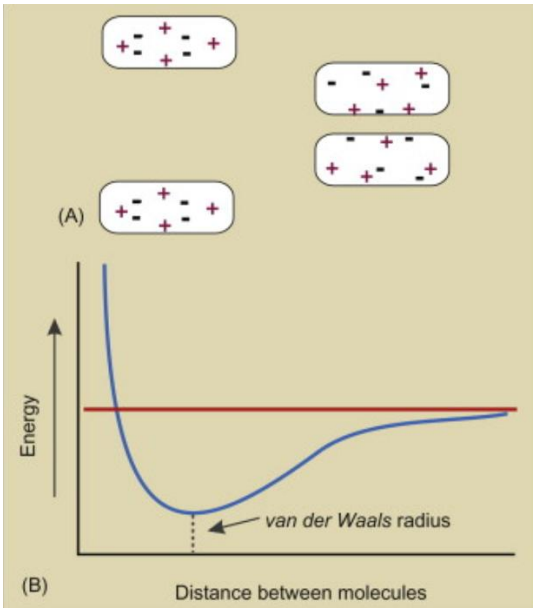

Figure 2.16 The illustration of van der Waals force.[154]

The mechanism behind London dispersion forces comes from quantum mechanical fluctuations in electron clouds. In a nonpolar molecule, the constant motion of electrons can lead to an

asymmetrical distribution at any given moment, creating a transient dipole. This temporary dipole induces a corresponding dipole in a neighbouring molecule, resulting in an attractive force[155]. The strength of these forces depends on the polarizability of molecule, which correlates with its size and number of electrons. For example, larger molecules like octane have greater polarizability than smaller ones like methane, leading to stronger dispersion forces and higher boiling points in homologous series[156].

Although London dispersion forces are relatively weak, typically ranging from 0.1-10 kJ/mol, their cumulative effect can be significant, particularly in large molecules or systems like polymers and biological macromolecules such as DNA, where they contribute to structural stability[155]. These forces are distance-dependent, decreasing rapidly with separation (proportional to r^{-6}, where r is the distance between molecules). Molecular shape and surface area also influence their strength, with linear molecules exhibiting stronger dispersion forces than branched ones due to greater contact area[152]. Therefore, the van der Waals interaction in the C_{60}/C_{70}-DT systems can be so complex, as there are three types of molecules (C_{60} (spherical), C_{70} (ellipsoidal), DT (linear)) contribute to this system simultaneously. Especially, for the C_{70} molecules, their molecular orientation can be strongly affected by the surrounding molecules. If small amount of C_{70} are deposited on the substrate, C_{70} would keep a lying down orientation so that the van der Waals interaction between C_{70} and the substrate could be stronger[148]. However, with the deposition of the C_{60} and DT molecules, the C_{70} are likely to change their orientations to interactive more effectively with the surrounding molecules. Therefore, the molecular orientation observed via STM can also provide useful information about this system.

References

[1] Whitesides, G. M.; Boncheva, M. Beyond Molecules: Self-Assembly of Mesoscopic and Macroscopic Components. *Proc. Natl. Acad. Sci.* **2002**, *99*, 4769–4774.

[2] Pinheiro, A. V.; Han, D.; Shih, W. M.; Yan, H. Challenges and Opportunities for Structural DNA Nanotechnology. *Nat. Nanotechnol.* **2011**, *6*, 763–772.

[3] Yin, P.; Choi, H. M. T.; Calvert, C. R.; Pierce, N. A. Programming Biomolecular Self-Assembly Pathways. *Nature* **2008**, *451*, 318–322.

[4] Rothemund, P. W. K. Folding DNA to Create Nanoscale Shapes and Patterns. *Nature* **2006**, *440*, 297–302.

[5] Zhang, S. Emerging Biological Materials through Molecular Self-Assembly. *Biotechnol. Adv.* **2002**, *20*, 321–339.

[6] Chang, R.; Zhao, L.; Xing, R.; Li, J.; Yan, X. Functional Chromopeptide Nanoarchitectonics: Molecular Design, Self-Assembly and Biological Applications. *Chem. Soc. Rev.* **2023**, *52*, 2688–2712.

[7] Sun, X.; Jia, P.; Zhang, H.; Dong, M.; Wang, J.; Li, L.; Bu, T.; Wang, X.; Wang, L.; Lu, Q.; Wang, J. Green Regenerative Hydrogel Wound Dressing Functionalized by Natural Drug-Food Homologous Small Molecule Self-Assembled Nanospheres. *Adv. Funct. Mater.* **2021**, *32*, 2106572.

[8] Pochan, D.; Scherman, O. Introduction: Molecular Self-Assembly. *Chem. Rev.* **2021**, *121*, 13699–13700.

[9] Verstraete, L.; De Feyter, S. 2D Self-Assembled Molecular Networks and On-Surface Reactivity under Nanoscale Lateral Confinement. *Chem. Soc. Rev.* **2021**, *50*, 5884–5897.

[10] Whitesides, G.; Mathias, J.; Seto, C. Molecular Self-Assembly and Nanochemistry: A Chemical Strategy for the Synthesis of Nanostructures. *Science* **1991**, *254*, 1312–1319.

[11] Margenau, H. Van Der Waals Forces. *Rev. Mod. Phys.* **1939**, *11*, 1–35.

[12] Grabowski, S. J. *Hydrogen Bonding - New Insights*; Springer: Dordrecht, 2014.

[13] Li, Y.; Wang, Y.; Huang, G.; Gao, J. Cooperativity Principles in Self-Assembled Nanomedicine. *Chem. Rev.* **2018**, *118*, 5359–5391.

[14] Smith, M.; March, J. *March's Advanced Organic Chemistry : Reactions, Mechanisms, and Structure.*; John Wiley & Sons: Hoboken, N.J., 2007.

[15] Knoblock, K. M.; Silvestri, C. J.; Collard, D. M. Stacked Conjugated Oligomers as Molecular Models to Examine Interchain Interactions in Conjugated Materials. *J. Am. Chem. Soc.* **2006**, *128*, 13680–13681.

[16] Lawrence, G. *Introduction to Coordination Chemistry*; John Wiley: Chichester, 2010.

[17] Furukawa, H.; Cordova, K. E.; O'Keeffe, M.; Yaghi, O. M. The Chemistry and Applications of Metal-Organic Frameworks. *Science* **2013**, *341*, 1230444.

[18] Xu, Z. Mechanics of Metal-Catecholate Complexes: The Roles of Coordination State and Metal Types. *Sci. Rep.* **2013**, *3*, 2914.

[19] Meka, V. S.; Sing, M. K. G.; Pichika, M. R.; Nali, S. R.; Kolapalli, V. R. M.; Kesharwani, P. A Comprehensive Review on Polyelectrolyte Complexes. *Drug Discov. Today* **2017**, *22*, 1697–1706.

[20] Richter, R. P.; Bérat, R.; Brisson, A. R. Formation of Solid-Supported Lipid Bilayers: An Integrated View. *Langmuir* **2006**, *22*, 3497–3505.

[21] Perrot, P. *A to Z of Thermodynamics*; Oxford ; New York Oxford University Press, 2008.

[22] Carlos, J. *Thermodynamics*; BoD – Books on Demand, 2011.

[23] Choo, Y.; Majewski, P. W.; Masafumi Fukuto; Osuji, C. O.; Yager, K. G. Pathway-Engineering for Highly-Aligned Block Copolymer Arrays. *Nanoscale* **2017**, *10*, 416–427.

[24] Ulman, A. Formation and Structure of Self-Assembled Monolayers. *Chem. Rev.* **1996**, *96*, 1533–1554.

[25] Edmondson, M.; Saywell, A. Molecular Diffusion and Self-Assembly: Quantifying the Influence of Substrate Hcp and Fcc Atomic Stacking. *Nano Lett.* **2022**, *22*, 8210–8215.

[26] Percec, V.; Ungar, G.; Mihai Peterca. Self-Assembly in Action. *Science* **2006**, *313*, 55–56.

[27] Badia, A.; Lennox, R. B.; Reven, L. A Dynamic View of Self-Assembled Monolayers. *Acc. Chem. Res.* **2000**, *33*, 475–481.

[28] Carl, N.; Wenke Müller; Ralf Schweins; Huber, K. Controlling Self-Assembly with Light and Temperature. *Langmuir* **2019**, *36*, 223–231.

[29] Korevaar, P. A.; Schaefer, C.; Tom; Meijer, E. W. Controlling Chemical Self-Assembly by Solvent-Dependent Dynamics. *J. Am. Chem. Soc.* **2012**, *134*, 13482–13491.

[30] Quan, Z.; Xu, H.; Wang, C.; Wen, X.; Wang, Y.; Zhu, J.; Li, R.; Sheehan, C. J.; Wang, Z.; Smilgies, Detlef-M.; Luo, Z.; Fang, J. Solvent-Mediated Self-Assembly of Nanocube Superlattices. *J. Am. Chem. Soc.* **2014**, *136*, 1352–1359.

[31] Packwood, D. M.; Han, P.; Hitosugi, T. Chemical and Entropic Control on the Molecular Self-Assembly Process. *Nat. Commun.* **2017**, *8*, 14463.

[32] Janas, A.; Jany, B. R.; Szajna, K.; A. Kryshtal; G. Cempura; Kruk, A.; Krok, F. Nanostructure Phase and Interface Engineering via Controlled Au Self-Assembly on GaAs(001) Surface. *Appl. Surf. Sci.* **2019**, *492*, 703–710.

[33] Lei, P.; Zhao, L.; He, L.; Zhao, F.; Xiao, X.; Tu, B.; Zeng, Q. Temperature Induced Supramolecular Structural Transition and as a Host Cavity to Capture the Guest Molecules. *Appl. Surf. Sci.* **2021**, *550*, 149352–149352.

[34] Pauling, L.; Wheland, G. W. The Nature of the Chemical Bond. V. The Quantum-Mechanical Calculation of the Resonance Energy of Benzene and Naphthalene and the Hydrocarbon Free Radicals. *J. Chem. Phys.* **1933**, *1*, 362–374.

[35] WATSON, J. D.; CRICK, F. H. C. Molecular Structure of Nucleic Acids: A Structure for Deoxyribose Nucleic Acid. *Nature* **1953**, *171*, 737–738.

[36] Mann, S. Molecular Recognition in Biomineralization. *Nature* **1988**, *332*, 119–124.

[37] Whitelam, S. Examples of Molecular Self-Assembly at Surfaces. *Adv. Mater.* **2015**, *27*, 5720–5725.

[38] Palmer, L. C.; Stupp, S. I. Molecular Self-Assembly into One-Dimensional Nanostructures. *Acc. Chem. Res.* **2008**, *41*, 1674–1684.

[39] Chan, F. T. S.; Kaminski, C. F.; Kaminski Schierle, G. S. HomoFRET Fluorescence Anisotropy Imaging as a Tool to Study Molecular Self-Assembly in Live Cells. *ChemPhysChem* **2010**, *12*, 500–509.

[40] Zhang, F.; Srinivasan, M. P. Self-Assembled Molecular Films of Aminosilanes and Their Immobilization Capacities. *Langmuir* **2004**, *20*, 2309–2314.

[41] Grimme, S.; Antony, J.; Schwabe, T.; Mück-Lichtenfeld, C. Density Functional Theory with Dispersion Corrections for Supramolecular Structures, Aggregates, and Complexes of (Bio)Organic Molecules. *Org. Biomol. Chem.* **2007**, *5*, 741–758.

[42] Maillet, J.-B. .; Lachet, V.; Coveney, P. V. Large Scale Molecular Dynamics Simulation of Self-Assembly Processes in Short and Long Chain Cationic Surfactants. *Phys. Chem. Chem. Phys.* **1999**, *1*, 5277–5290.

[43] Yi, R.; Mao, Y.; Shen, Y.; Chen, L. Self-Assembled Monolayers for Batteries. *J. Am. Chem. Soc.* **2021**, *143*, 12897–12912.

[44] Hirschi, S.; Ward, T. R.; Meier, W.; Müller, D. J.; Fotiadis, D. Synthetic Biology: Bottom-up Assembly of Molecular Systems. *Chem. Rev.* **2022**, *122*, 16294–16328.

[45] Li, L.; Wang, Y.; Wang, X.; Lin, R.; Luo, X.; Liu, Z.; Zhou, K.; Xiong, S.; Bao, Q.; Chen, G.; Tian, Y.; Deng, Y.; Xiao, K.; Wu, J.; Saidaminov, M. I.; Lin, H.; Ma, C.; Zhao, Z.; Wu, Y.; Zhang, L. Flexible All-Perovskite Tandem Solar Cells Approaching 25% Efficiency with Molecule-Bridged Hole-Selective Contact. *Nat. Energy* **2022**, *7*, 708–717.

[46] Tan, W.; Zhang, Q.; Wang, J.; Yi, M.; He, H.; Xu, B. Enzymatic Assemblies of Thiophosphopeptides Instantly Target Golgi Apparatus and Selectively Kill Cancer Cells**. *Angew. Chem.* **2021**, *60*, 12796–12801.

[47] Liu, F.; Chen, Y.; Huang, Y.; Li, Y.; Lu, Z.; Han, H.; Song, X.; Jin, Q.; Ji, J. Synergistic Wall Digestion and Cuproptosis against Fungal Infections Using Lywallzyme-Induced Self-Assembly of Metal-Phenolic Nanoflowers. *Nat. Commun.* **2024**, *15*, 9004.

[48] Li, P.; Ding, F. Origin of the Herringbone Reconstruction of Au(111) Surface at the Atomic Scale. *Sci. Adv.* **2022**, *8*, 8.

[49] Repain, V.; Berroir, J. M.; Rousset, S.; Lecoeur, J. Reconstruction, Step Edges and Self-Organization on the Au(111) Surface. *Appl. Surf. Sci.* **2000**, *162-163*, 30–36.

[50] Bartelt, N. C.; Thürmer, K. Structure and Energetics of the Elbows in the Au(111) Herringbone Reconstruction. *Physical Review B* **2021**, *104*, 165425.

[51] Walen, H.; Liu, D.; Oh, J.; Lim, H.; Evans, J. W.; Kim, Y.; Thiel, P. A. Self-Organization of S Adatoms on Au(111): √3R30° Rows at Low Coverage. *J. Chem. Phys.* **2015**, *143*, 014704.

[52] Rai, A.; Singh, V. K.; Nayak, J.; Roy Barman, S. Parameter Dependent Fabrication of Chromium Nano-Structures on Au(111) Surface. *Surf. Sci.* **2019**, *679*, 169–173.

[53] Hanke, F.; Björk, J. Structure and Local Reactivity of the Au(111) Surface Reconstruction. *Phys. Rev. B* **2013**, *87*, 235422.

[54] Yoshinori Shiihara; Masanori Kohyama; Ishibashi, S. Origin of Surface Stress on Late Transition Metal Surfaces:*Ab Initio*Local Stress and Tight-Binding Model. *Phys. Rev. B* **2013**, *87*, 125430.

[55] Barth, J. V.; Brune, H.; Ertl, G.; Behm, R. J. Scanning Tunneling Microscopy Observations on the Reconstructed Au(111) Surface: Atomic Structure, Long-Range Superstructure, Rotational Domains, and Surface Defects. *Phys. Rev. B* **1990**, *42*, 9307–9318.

[56] Bragg, W. L. The Structure of Some Crystals as Indicated by Their Diffraction of X-Rays. *Proc. R. Soc. A* **1913**, *89*, 248–277.

[57] Bartelt, N. C.; Thürmer, K. Structure and Energetics of the Elbows in the Au(111) Herringbone Reconstruction. *Phys. Rev. B* **2021**, *104*, 165425.

[58] Bain, C. D.; Whitesides, G. M. Modeling Organic Surfaces with Self-Assembled Monolayers. *Adv. Mater.* **1989**, *1*, 110–116.

[59] Dubois, L. H.; Nuzzo, R. G. Synthesis, Structure, and Properties of Model Organic Surfaces. *Ann. Phys. Chem.* **1992**, *43*, 437–463.

[60] WANG, T.; Vazquez, A.; Kato, A.; Schmidt, L. D. Sulfur on Noble Metal Catalyst Particles. *J. Catal.* **1982**, *78*, 306–318.

[61] Sellers, H.; Ulman, A.; Shnidman, Y.; Eilers, J. E. Structure and Binding of Alkanethiolates on Gold and Silver Surfaces: Implications for Self-Assembled Monolayers. *J. Am. Chem. Soc.* **1993**, *115*, 9389–9401.

[62] Rodriguez, J. A.; Dvorak, J.; Jirsak, T.; Liu, G.; Hrbek, J.; Aray, Y.; González, C. Coverage Effects and the Nature of the Metal−Sulfur Bond in S/Au(111): High-Resolution Photoemission and Density-Functional Studies. *J. Am. Chem. Soc.* **2003**, *125*, 276–285.

[63] Ulman, A. Formation and Structure of Self-Assembled Monolayers. *Chem. Rev.* **1996**, *96*, 1533–1554.

[64] Nuzzo, R. G.; Allara, D. L. Adsorption of Bifunctional Organic Disulfides on Gold Surfaces. *J. Am. Chem. Soc.* **1983**, *105*, 4481–4483.

[65] Tjandra, S.; Zaera, F. Adsorption and Thermal Decomposition of Propyl Iodides on Ni(100) Surfaces. *Langmuir* **1994**, *10*, 2640–2646.

[66] Schreiber, F. Structure and Growth of Self-Assembling Monolayers. *Prog. Surf. Sci.* **2000**, *65*, 151–257.

[67] Smith, R. K.; Lewis, P. A.; Weiss, P. S. Patterning Self-Assembled Monolayers. *Prog. Surf. Sci.* **2004**, *75*, 1–68.

[68] Li, S.-S.; Xu, L.-P.; Wan, L.-J.; Wang, S.-T.; Jiang, L. Time-Dependent Organization and Wettability of Decanethiol Self-Assembled Monolayer on Au(111) Investigated with STM. *J. Phys. Chem. B* **2006**, *110*, 1794–1799.

[69] Alves, C. A.; Smith, E. L.; Porter, M. D. Atomic Scale Imaging of Alkanethiolate Monolayers at Gold Surfaces with Atomic Force Microscopy. *J. Am. Chem. Soc.* **1992**, *114*, 1222–1227.

[70] Li, F.; Tang, L.; Zhou, W.; Guo, Q. Resolving the Au-Adatom-Alkanethiolate Bonding Site on Au(111) with Domain Boundary Imaging Using High-Resolution Scanning Tunneling Microscopy. *J. Am. Chem. Soc.* **2010**, *132*, 13059–13063.

[71] Dubois, L. H.; Zegarski, B. R.; Nuzzo, R. G. Molecular Ordering of Organosulfur Compounds on Au(111) and Au(100): Adsorption from Solution and in Ultrahigh Vacuum. *J. Chem. Phys.* **1993**, *98*, 678–688.

[72] Hautman, J.; Klein, M. L. Simulation of a Monolayer of Alkyl Thiol Chains. *J. Chem. Phys.* **1989**, *91*, 4994–5001.

[73] G. Haehner; C. Woell; Buck, M.; M. Grunze. Investigation of Intermediate Steps in the Self-Assembly of N-Alkanethiols on Gold Surfaces by Soft X-Ray Spectroscopy. *Langmuir* **1993**, *9*, 1955–1958.

[74] M. Toerker; Staub, R.; Fritz, T.; T. Schmitz-Hübsch; F. Sellam; Leo, K. Annealed Decanethiol Monolayers on Au(111) – Intermediate Phases between Structures with High and Low Molecular Surface Density. *Surf. Sci.* **2000**, *445*, 100–108.

[75] Yan, C.; Yuan, R.; Pfalzgraff, W. C.; Nishida, J.; Wang, L.; Markland, T. E.; Fayer, M. D. Unraveling the Dynamics and Structure of Functionalized Self-Assembled Monolayers on Gold Using 2D IR Spectroscopy and MD Simulations. *Proc. Natl. Acad. Sci.* **2016**, *113*, 4929–4934.

[76] Bumm, L. A.; Arnold, J. J.; Dunbar, T. D.; Allara, D. L.; Weiss, P. S. Electron Transfer through Organic Molecules. *J. Phys. Chem. B* **1999**, *103*, 8122–8127.

[77] Staub, R.; Toerker, M.; Fritz, T.; Schmitz-Hübsch, T.; Sellam, F.; Leo, K. Scanning Tunneling Microscope Investigations of Organic Heterostructures Prepared by a Combination of Self-Assembly and Molecular Beam Epitaxy. *Surf. Sci.* **2000**, *445*, 368–379.

[78] Schönenberger, C.; Jorritsma, J.; J. A. M. Sondag-Huethorst; L. G. J. Fokkink. Domain Structure of Self-Assembled Alkanethiol Monolayers on Gold. *J. Phys. Chem.* **1995**, *99*, 3259–3271.

[79] Zhang, L.; Li, X.; Li, H.; Fan, X. Theoretical Studies on the Electronic Properties of Alkyl Chains. *Comput. Theor. Chem.* **2016**, *1085*, 18–22.

[80] Love, J. C.; Estroff, L. A.; Kriebel, J. K.; Nuzzo, R. G.; Whitesides, G. M. Self-Assembled Monolayers of Thiolates on Metals as a Form of Nanotechnology. *Chem. Rev.* **2005**, *105*, 1103–1170.

[81] Zeng, C.; Li, B.; Wang, B.; Wang, H.; Wang, K.; Yang, J.; Hou, J. G.; Zhu, Q. What Can a Scanning Tunneling Microscope Image Do for the Insulating Alkanethiol Molecules on Au(111) Substrates? *J. Chem. Phys.* **2002**, *117*, 851–856.

[82] Liu, S.; Lü, Y.; Kappes, M. M.; Ibers, J. A. The Structure of the C_{60} Molecule: X-Ray Crystal Structure Determination of a Twin at 110 K. *Science* **1991**, *254*, 408–410.

[83] Yu, J.-J.; Ngunjiri, J. N.; Kelley, A. T.; Garno, J. C. Nanografting versus Solution Self-Assembly of α,ω-Alkanedithiols on Au(111) Investigated by AFM. *Langmuir* **2008**, *24*, 11661–11668.

[84] Kokkin, D. L.; Zhang, R.; Steimle, T. C.; Wyse, I. A.; Pearlman, B. W.; Varberg, T. D. Au–S Bonding Revealed from the Characterization of Diatomic Gold Sulfide, AuS. *J. Phys. Chem. A* **2015**, *119*, 11659–11667.

[85] Xue, Y.; Li, X.; Li, H.; Zhang, W. Quantifying Thiol–Gold Interactions towards the Efficient Strength Control. *Nat. Commun.* **2014**, *5*, 4348.

[86] Delamarche, E.; Michel, B.; Kang, H.; Gerber, Ch. Thermal Stability of Self-Assembled Monolayers. *Langmuir* **1994**, *10*, 4103–4108.

[87] Grzeskowiak, J.; Ventrice, C. A. Low Energy Electron Interactions with 1-Decanethiol Self-Assembled Monolayers on Au(111). *J. Vac. Sci. Technol.* **2019**, *37*, 051401.

[88] Asyuda, A.; Das, S.; Zharnikov, M. Thermal Stability of Alkanethiolate and Aromatic Thiolate Self-Assembled Monolayers on Au(111): An X-Ray Photoelectron Spectroscopy Study. *J. Phys. Chem. C* **2021**, *125*, 21754–21763.

[89] Jadzinsky, P. D.; Calero, G.; Ackerson, C. J.; Bushnell, D. A.; Kornberg, R. D. Structure of a Thiol Monolayer-Protected Gold Nanoparticle at 1.1 a Resolution. *Science* **2007**, *318*, 430–433.

[90] Maksymovych, P.; Sorescu, D. C.; Yates, J. T. Gold-Adatom-Mediated Bonding in Self-Assembled Short-Chain Alkanethiolate Species on the Au(111) Surface. *Phys. Rev. Lett.* **2006**, *97*, 146103.

[91] Maksymovych, P.; Sorescu, D. C.; Jordan, K. D.; Yates, J. T. Collective Reactivity of Molecular Chains Self-Assembled on a Surface. *Science* **2008**, *322*, 1664–1667.

[92] Maksymovych, P.; Dougherty, D. B.; Zhu, X.-Y.; Yates, J. T. Nonlocal Dissociative Chemistry of Adsorbed Molecules Induced by Localized Electron Injection into Metal Surfaces. *Phys. Rev. Lett.* **2007**, *99*, 016101.

[93] Maksymovych, P.; Oleksandr Voznyy; Dougherty, D. B.; Sorescu, D. C.; Yates, J. R. Gold Adatom as a Key Structural Component in Self-Assembled Monolayers of Organosulfur Molecules on Au(111). *Prog. Surf. Sci.* **2010**, *85*, 206–240.

[94] Li, F.-S.; Zhou, W.; Guo, Q. Uncovering the Hidden Gold Atoms in a Self-Assembled Monolayer of Alkanethiol Molecules on Au(111). *Phys. Rev. B* **2009**, *79*, 113412.

[95] Kautz, N. A.; Kandel, S. A. Alkanethiol/Au(111) Self-Assembled Monolayers Contain Gold Adatoms: Scanning Tunneling Microscopy before and after Reaction with Atomic Hydrogen. *J. Am. Chem. Soc.* **2008**, *130*, 6908–6909.

[96] Tsvetanova, M.; Valent; Bertolino, M. C.; Gao, Y.; Siekman, M. H.; Jurriaan Huskens; Harold; Sotthewes, K. Nanoscale Work Function Contrast Induced by Decanethiol Self-Assembled Monolayers on Au(111). *Langmuir* **2020**, *36*, 12745–12754.

[97] Häkkinen, H. The Gold–Sulfur Interface at the Nanoscale. *Nat. Chem.* **2012**, *4*, 443–455.

[98] Evangelina Laura Pensa; Emiliano Cortés; Gastón Corthey; Carro, P.; Vericat, C.; Fonticelli, M. H.; Benítez, G.; Rubert, A. A.; Roberto Carlos Salvarezza. The Chemistry of the Sulfur–Gold Interface: In Search of a Unified Model. *Acc. Chem. Res.* **2012**, *45*, 1183–1192.

[99] Poirier, G. E. Coverage-Dependent Phases and Phase Stability of Decanethiol on Au(111). *Langmuir* **1999**, *15*, 3018–3020.

[100] Poirier, G. E.; Fitts, W. P.; White, J. M. Two-Dimensional Phase Diagram of Decanethiol on Au(111). *Langmuir* **2001**, *17*, 1176–1183.

[101] Qian, Y.; Yang, G.; Yu, J.; Jung, T. A.; Liu, G. Structures of Annealed Decanethiol Self-Assembled Monolayers on Au(111): An Ultrahigh Vacuum Scanning Tunneling Microscopy Study. *Langmuir* **2003**, *19*, 6056–6065.

[102] Busseron, E.; Ruff, Y.; Moulin, E.; Giuseppone, N. Supramolecular Self-Assemblies as Functional Nanomaterials. *Nanoscale* **2013**, *5*, 7098.

[103] Ding, H.; Zhang, X.; Li, B.; Wang, Y.; Xia, C.; Zhao, H.; Yang, H.; Gao, Y.; Chen, X.; Gao, J.; Pan, M.; Guo, Q. Orientational Growth of Flexible van Der Waals Supramolecular Networks. *Small Struct.* **2023**, *5*, 2300230.

[104] Kroto, H. W.; Heath, J. R.; O'Brien, S. C.; Curl, R. F.; Smalley, R. E. C60: Buckminsterfullerene. *Nature* **1985**, *318*, 162–163.

[105] Krätschmer, W.; Lamb, L. D.; Fostiropoulos, K.; Huffman, D. R. Solid C60: A New Form of Carbon. *Nature* **1990**, *347*, 354–358.

[106] Diederich, F.; Whetten, R. L. Beyond C60: The Higher Fullerenes. *Acc. Chem. Res.* **1992**, *25*, 119–126.

[107] Liu, S.; Lü, Y.; Kappes, M. M.; Ibers, J. A. The Structure of the C_{60} Molecule: X-Ray Crystal Structure Determination of a Twin at 110 K. *Science* **1991**, *254*, 408–410.

[108] Girard, C.; Ph. Lambin; Alain Dereux; Lucas, A. Van Der Waals Attraction between Twoc60Fullerene Molecules and Physical Adsorption ofc60. *Phys. Rev. B* **1994**, *49*, 11425–11432.

[109] Sheka, E. F.; Razbirin, B. S.; Nelson, D. K. Continuous Symmetry of c_{60} Fullerene and Its Derivatives. *J. Phys. Chem. A* **2011**, *115*, 3480–3490.

[110] Kim, J.; Yamada, Y.; Kawai, M.; Tanabe, T.; Sato, S. Spectral Change of Simulated X-Ray Photoelectron Spectroscopy from Graphene to Fullerene. *J. Mater. Sci.* **2015**, *50*, 6739–6747.

[111] David, W. I. F.; Ibberson, R. M.; Matthewman, J. C.; Prassides, K.; Dennis, T. J. S.; Hare, J. P.; Kroto, H. W.; Taylor, R.; Walton, D. R. M. Crystal Structure and Bonding of Ordered C60. *Nature* **1991**, *353*, 147–149.

[112] Hedberg, K.; Hedberg, L.; Bethune, D. S.; Brown, C. A.; Dorn, H. C.; Johnson, R. D.; De Vries, M. Bond Lengths in Free Molecules of Buckminsterfullerene, c_{60}, from Gas-Phase Electron Diffraction. *Science* **1991**, *254*, 410–412.

[113] Diana, N.; Yamada, Y.; Syun Gohda; Ono, H.; Kubo, S.; Sato, S. Carbon Materials with High Pentagon Density. *J. Mater. Sci.* **2020**, *56*, 2912–2943.

[114] Lu, X.; M. Grobis; Khoo, K. H.; Louie, S. G.; Crommie, M. F. Charge Transfer and Screening in Individualc60Molecules on Metal Substrates: A Scanning Tunneling Spectroscopy and Theoretical Study. *Phys. Rev. B* **2004**, *70*, 115418.

[115] McKenzie, D. R.; Davis, C. A.; Cockayne, H.; Muller, D. A.; Vassallo, A. M. The Structure of the C70 Molecule. *Nature* **1992**, *355*, 622–624.

[116] Hedberg, K.; Hedberg, L.; Bühl, M.; Bethune, D. S.; Brown, C. A.; Johnson, R. D. Molecular Structure of Free Molecules of the Fullerene C_{70} from Gas-Phase Electron Diffraction. *J. Am. Chem. Soc.* **1997**, *119*, 5314–5320.

[117] Tomiyama, T.; Uchiyama, S.; Shinohara, H. Solubility and Partial Specific Volumes of C60 and C70. *Chem. Phys. Lett.* **1997**, *264*, 143–148.

[118] Rao, C. N. R.; Seshadri, R.; Govindaraj, A.; Sen, R. Fullerenes, Nanotubes, Onions and Related Carbon Structures. *Mat. Sci. Eng. R* **1995**, *15*, 209–262.

[119] Saito, S.; Atsushi Oshiyama. Electronic and Geometric Structures ofc70. *Phys. Rev. B* **1991**, *44*, 11532–11535.

[120] Ding, C.; Jinlong, Y.; Rongsheng, H.; Kelin, W. Formation Mechanism and Structural and Electronic Properties of Metal-Substituted Fullerenesc69M(M=Co. *Phys. Rev. A* **2001**, *64*, 043201.

[121] Lobanov, B. V.; Murzashev, A. I. Electron and Optical Properties of Fullerene C70 within the Conception of a Strongly Correlated State. *Phys. Solid State* **2017**, *59*, 423–427.

[122] JK Gimzewski; Modesti, S.; Schlittler, R. Cooperative Self-Assembly of Au Atoms and C60 on Au(110) Surfaces. *Phys. Rev. Lett.* **1994**, *72*, 1036–1039.

[123] Bonifazi, D.; Kiebele, A.; Meike Stöhr; Cheng, F.; Jung, T. A.; Diederich, F.; Hannes Spillmann. Supramolecular Nanostructuring of Silver Surfaces via Self-Assembly of [60]Fullerene and Porphyrin Modules. *Adv. Funct. Mater.* **2007**, *17*, 1051–1062.

[124] Ogawa, A.; Tachibana, M.; Kondo, M.; Yoshizawa, K.; Fujimoto, H.; Hoffmann, R. Orbital Interactions between a C_{60} Molecule and Cu(111) Surface. *J. Phys. Chem. B* **2003**, *107*, 12672–12679.

[125] T. Orzali; Forrer, D.; M. Sambi; A. Vittadini; M. Casarin; E. Tondello. Temperature-Dependent Self-Assemblies of c_{60} on (1 × 2)-Pt(110): A STM/DFT Investigation. *J. Phys. Chem. C* **2007**, *112*, 378–390.

[126] Pussi, K.; Li, H. I.; Shin, H.; Serkovic Loli, L. N.; Shukla, A. K.; Ledieu, J.; Fournée, V.; Wang, L. L.; Su, S. Y.; Marino, K. E.; Snyder, M. V.; Diehl, R. D. Elucidating the Dynamical Equilibrium of C60 Molecules on Ag(111). *Phys. Rev. B* **2012**, *86*, 205406.

[127] Wang, H.; Zeng, C.; Wang, B.; Hou, J. G.; Li, Q.; Yang, J. Orientational Configurations of the C60 Molecules in the(2×2)Superlattice on a Solid. *Phys. Rev. B* **2001**, *63*, 085417.

[128] Vaezi, M.; Nejat Pishkenari, H.; Nemati, A. Mechanism of C60 Rotation and Translation on Hexagonal Boron-Nitride Monolayer. *J. Chem. Phys.* **2020**, *153*, 234702.

[129] Jung, M.; Shin, D.; Sohn, S.-D.; Kwon, S.-Y.; Park, N.; Shin, H.-J. Atomically Resolved Orientational Ordering of C60 Molecules on Epitaxial Graphene on Cu(111). *Nanoscale* **2014**, *6*, 11835–11840.

[130] Schull, G.; Berndt, R. Orientationally Ordered (7×7) Superstructure ofc60on Au(111). *Phys. Rev. Lett.* **2007**, *99*, 226105.

[131] Daughton, D. R.; Gupta, J. A. Orientation Dependence of Charge Transfer for C60 on Cu(100). *Appl. Phys. Lett.* **2011**, *98*, 133303.

[132] Wang, X.-D.; V. Yu. Yurov; Hashizume, T.; Shinohara, H.; Sakurai, T. Imaging of C70 Intramolecular Structures with Scanning Tunneling Microscopy. *Phys. Rev. B* **1994**, *49*, 14746–14749.

[133] Niu, G.; Geng, J.; Wang, X.; Yang, X.; Xiong, W.; Zhang, H.; Ruan, Z.; Zhang, Y.; Gao, L.; Lu, J.; Cai, J. Adsorption Configurations and Electronic Properties of Self-Assembled C_{60} and C_{70} Molecules on a Semiconductor CuSe Monolayer with Periodic Nanopores. *Nanotechnology* **2023**, *34*, 395602–395602.

[134] Altman, E. I.; Colton, R. J. Nucleation, Growth, and Structure of Fullerene Films on Au(111). *Surf. Sci.* **1992**, *279*, 49–67.

[135] Altman, E. I.; Colton, R. J. The Interaction of C60 with Noble Metal Surfaces. *Surf. Sci.* **1993**, *295*, 13–33.

[136] J.K. Gimzewski; Modesti, S.; Gerber, C.; Schlittler, R. R. Observation of a New Au (111) Reconstruction at the Interface of an Adsorbed C60 Overlayer. *Chem. Phys. Lett.* **1993**, *213*, 401–406.

[137] Zhang, X.; Yin, F.; Palmer, R. E.; Guo, Q. The C60/Au(111) Interface at Room Temperature: A Scanning Tunnelling Microscopy Study. *Surf. Sci.* **2008**, *602*, 885–892.

[138] Shin, H.; Schwarze, A.; Diehl, R. D.; K. Pussi; A. Colombier; Gaudry, É.; J. Ledieu; McGuirk, G. M.; Loli, S.; V. Fournée; Wang, L. L.; Schull, G.; Berndt, R. Structure and Dynamics of c60 Molecules on Au(111). *Phys. Rev. B* **2014**, *89*, 245428.

[139] Altman, E. I.; Colton, R. J. Interaction of C60 with the Au(111) 23×√3 Reconstruction. *J. Vac. Sci. Technol. B* **1994**, *12*, 1906–1909.

[140] Tzeng, C.-T. .; Lo, W.-S. .; Yuh, J.-Y. .; Chu, R.-Y. .; Tsuei, K.-D. . Photoemission, Near-Edge X-Ray-Absorption Spectroscopy, and Low-Energy Electron-Diffraction Study ofc60on Au(111) Surfaces. *Phys. Rev. B* **2000**, *61*, 2263–2272.

[141] Rogero, C.; Pascual, J. I.; Gómez-Herrero, J.; Baró, A. M. Resolution of Site-Specific Bonding Properties of C60 Adsorbed on Au(111). *J. Chem. Phys.* **2002**, *116*, 832–836.

[142] Shamloo, A.; Bakhtiari, M. A.; Tohidloo, M.; Seifi, S. Investigation of Fullerene Motion on Thermally Activated Gold Substrates with Different Shapes. *Scientific Reports* **2022**, *12*, 14397.

[143] M. Pedio; K. Hevesi; Zema, N.; M. Capozi; Perfetti, P.; R. Gouttebaron; J.-J. Pireaux; R. Caudano; Rudolf, P. C60/Metal Surfaces: Adsorption and Decomposition. *Surf. Sci.* **1999**, *437*, 249–260.

[144] Wragg, J. L.; Chamberlain, J. E.; White, H. W.; W. Krätschmer; Huffman, D. R. Scanning Tunnelling Microscopy of Solid C60/C70. *Nature* **1990**, *348*, 623–624.

[145] Gimzewski, J. K.; Modesti, S.; David, T.; Schlittler, R. R. Scanning Tunneling Microscopy of Ordered C60 and C70 Layers on Au(111), Cu(111), Ag(110), and Au(110) Surfaces. *J. Vac. Sci. Technol. B* **1994**, *12*, 1942–1946.

[146] Wang, X.-D.; Xue, Q.; Hashizume, T.; Shinohara, H.; Nishina, Y.; Sakurai, T. STM Study on the Interactions of C70 with the Si(100)2×1 Surface. *Phys. Rev. B* **1994**, *49*, 7754–7758.

[147] Goldoni, A.; Cepek, C.; Larciprete, R.; Sangaletti, L.; Pagliara, S.; Floreano, L.; Gotter, R.; Verdini, A.; Morgante, A.; Luo, Y.; Nyberg, M. C70 Adsorbed on Cu(111): Metallic Character and Molecular Orientation. *J. Chem. Phys.* **2002**, *116*, 7685–7690.

[148] Katsonis, N.; Marchenko, A.; Fichou, D. Adsorption and Self-Assembly of C70 Molecules at the Au(111)/N-Tetradecane Interface: A Scanning Tunneling Microscopy Study. *Adv. Mater.* **2004**, *16*, 309–312.

[149] Chen, T.; Howells, S.; Gallagher, M.; D. Sarid; Lamb, L. D.; Huffman, D. R.; Workman, R. K. Scanning-Tunneling-Microscopy and Spectroscopy Studies of C70 Thin Films on Gold Substrates. *Phys. Rev. B* **1992**, *45*, 14411–14414.

[150] Kaya, D.; Wang, Y.; Mustafa Akyol; Faruk Karadag; Ahmet Ekicibil; Guo, Q. Self-Defined Transition State in Hybrid C70–Au Clusters Created by the Scanning Tunneling Microscope Tip. The *J. Phys. Chem. C* **2019**, *123*, 27945–27950.

[151] Arkadij Popović; Goran Dražič; Jože Marsel. Mass Spectrometric Investigations of Fullerenes. I. Vapour Pressure over the C_{60}/C_{70} Binary System. *Rapid Commun. Mass Spectrom.* **1994**, *8*, 985–990.

[152] Atkins, P. W. *Physical Chemistry : A Very Short Introduction*; Oxford University Press: Oxford, United Kingdom, 2014.

[153] Mcquarrie, D. A.; Simon, J. D. *Physical Chemistry : A Molecular Approach*; University Science Books, Cop: Sausalito, Calif., 1997.

[154] Pepper, I. L.; Gerba, C. P.; Gentry, T. J. *Environmental Microbiology*, 3rd ed.; Elsevier/Academic Press: San Diego, Ca., 2015.

[155] Israelachvili, J. N. *Intermolecular and Surface Forces*; Elsevier/Academic Press: Amsterdam, 2011.

[156] Levine, I. N. *Physical Chemistry*; Mcgraw-Hill: Boston, 2009.

III. Experimental Instruments

1. Low Temperature Scanning Tunnelling Microscope

Scanning Tunnelling Microscopy (STM) is a technique for imaging surfaces at the atomic level, which is widely used in nanotechnology. STM represents a cornerstone of modern surface science, enabling the visualization and manipulation of surfaces at the atomic scale. The STM was invented in 1981 by Gerd Binnig and Heinrich Rohrer at IBM Zurich Research Laboratories, and their work earned them the Nobel Prize in Physics in 1986[1,2].

The STM used in our group is a low temperature scanning tunnelling microscope (LT-STM) from Scienta Omicron (Serial number: 122), equipped with an ultra-high vacuum (UHV) system. The LT-STM is a dedicated instrument for scanning probe microscopy (SPM) experiments at very low temperatures. A successful thermal shielding concept together with the fact that the entire SPM stage is kept at sample temperature results in an outstanding thermal stability. Theoretically, the sample temperature is possible down to 2.5 K.

Figure 2.1 Scienta Omicron LT-STM in UHV system.

The sensitivity for this STM at room temperature (RT) is: Z: -6.7 nm/V; |X±| : 20.0 nm/V; |Y±| : 20.0 nm/V. Sensitivity at 77 K: Z: -2.0 nm/V; |X±| : 6.0 nm/V; |Y±| : 6.0 nm/V. Sensitivity at 5 K: Z: -1.2 nm/V; |X±| : 3.6 nm/V; |Y±| : 3.6 nm/V.

1.1 Components of Low Temperature Scanning Microscopy

1.1.1 Sample Preparation Chamber

The preparation chamber is mainly used for preparing various samples. The sample can be transferred into the chamber from the load lock through a magnetic rod, and then be picked by the manipulator. The manipulator is a movable and rotatable rod. Through adjusting the position and rotation angle of the manipulator, the sample can be exposed to any port on the chamber. Samples can also be treated with the radiation annealing and the direct current annealing on the manipulator, and the temperature of sample will be reflected through the thermocouple connected to the manipulator.

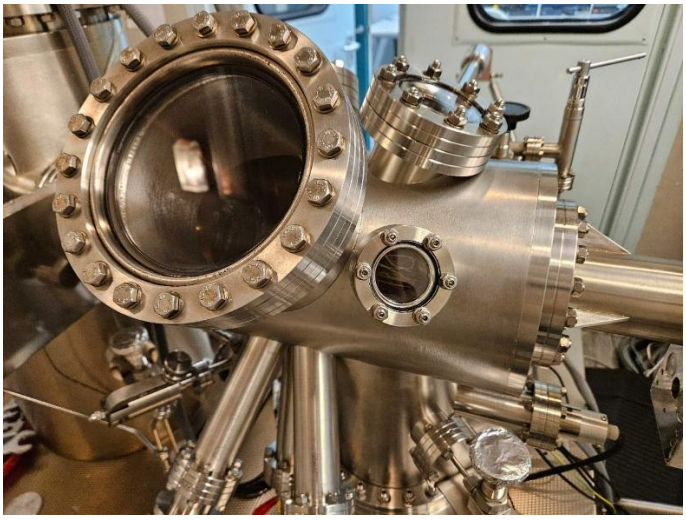

Figure 2.2 Preparation chamber of LT-STM.

There are several alternative ports left on the chamber, which can be installed with the extra evaporation sources, ion gun, RGA, etc. The tip/sample carousel within the chamber has positions available for up to 6 sample boards or tip carriers.

1.1.2 Sample Analysis Chamber

The scanning of the sample is conducted in the analysis chamber of LT-STM, where the sample can be transferred into the scanning stage with the wobble stick. The scanning stage is equipped with the vibration isolation elements to block most of noise caused by the mechanical vibration, as shown in **Figure 2.3** (a).

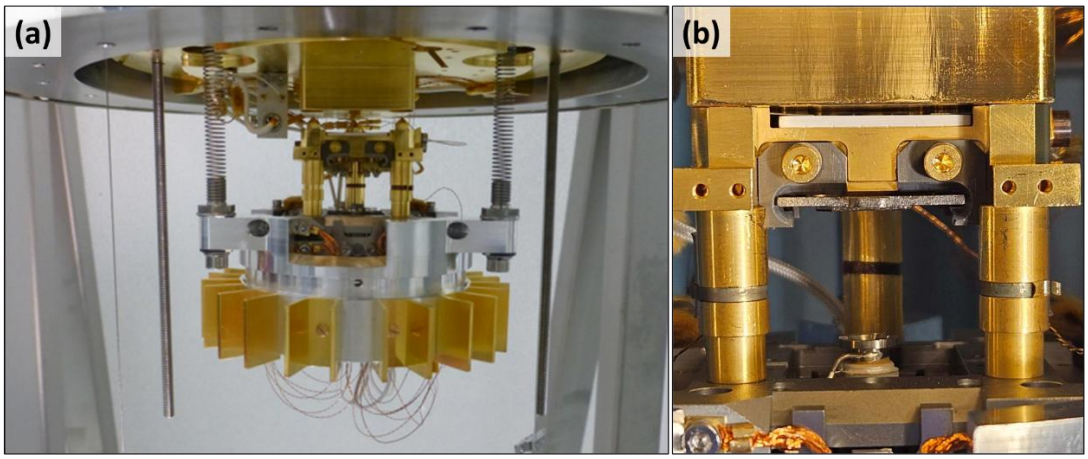

Figure 2.3 (a) Scanning stage of LT-STM, held by springs form the sides. (b) The scanning stage with a sample inserted at the scanning position.

When the sample is inserted onto the scanning stage, it is held by the spring flakes on the two sides. Meanwhile, the spring flakes also make the sample grounded and in contact with the sliding pins (Saphir Al_2O_3), which can help the sample effectively cool down when conducting the LT experiment. There are also some copper wires below the scanning stage connected from the bottom of the cryostat to the scanner, which are for the tip cooling during LT scanning.

1.1.3 Cryogenic Equipment

The cryogenic equipment of LT-STM consists of two concentric bath cryostats. The outer one is filled with LN_2 and serves for shielding. The inner one can be filled with either LN_2 or LHe and serves for cooling the STM.

Figure 2.4 Cryogenic equipment of LT-STM. The LN_2 and LHe can be filled from the top.

To cool down the system, the outer cryostat need to be filled with LN_2 first. And then when the inner cryostat is also filled with LN_2 or LHe, the sample and tip begin to cool down simultaneously. The sample is cooled down through the direct contact with the cooling pins, which is highly efficient. However, the tip and piezoelectric scanner is cooled down through the copper wires, which makes the cooling process less effective than that of the sample. Thus, there will be a tiny temperature difference between the tip and sample during the scanning, which is likely to cause the thermal drift. Each time the tip is moved to other areas on the sample, it requires about 30 minutes for temperature of the tip to stabilise.

1.1.4 Control Units

The control units in this LT-STM system include two parts: i) Nanonis SPM controller; ii) UHV system controller. As shown in **Figure 2.5**.

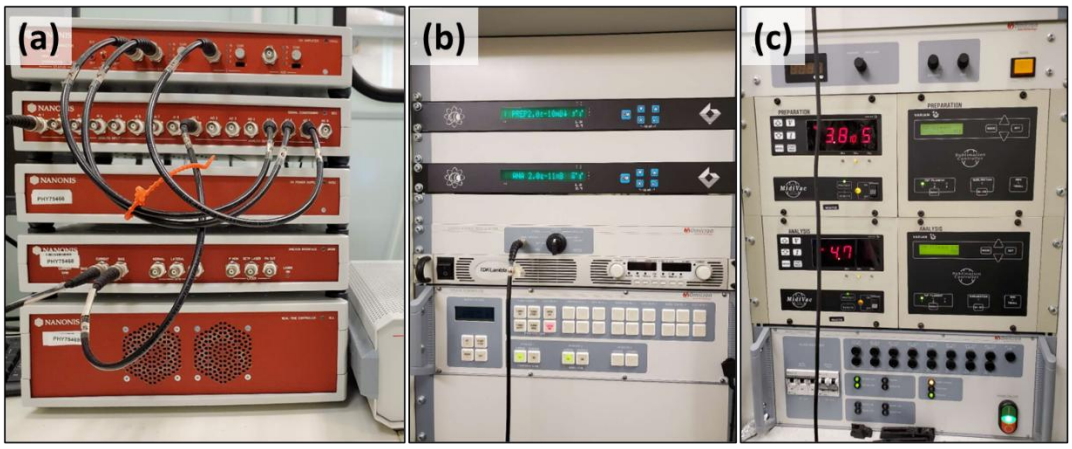

Figure 2.5 Control units of LT-STM in UHV system. (a) Nanonis SPM Controller. (b) The UHV control panel, controlling the ion gauge, PBN heater, turbo pump and gate valve. (c) The UHV control panel, controlling the ion pump, ion sputtering gun and the titanium sublimation pump.

Figure 2.5 (a) shows the Nanonis SPM controller system. After setting the scan parameters in the software, the controller sends the corresponding instructions to the piezoelectric scanner of STM to adjust the scan conditions. Meanwhile, the signals sent back form the STM are also converted by the controller, so that the software can further process these signals and transfer them into the graphic information.

The control panel shown in **Figure 2.5** (b) and (c) integrates all the switches for the pumps that maintain UHV. In addition, the switches of the ion sputtering gun, PBN annealing and the bakeout are also integrated in this panel.

1.2 Basic Components for STM Scanning

A complete STM system requires multiple components to work together, typically including:

i) Scanning Tip

The scanning tip is a crucial element, typically prepared from tungsten or platinum-iridium due to their conductive properties and ability to form a sharp end. The sharpness of the tip is vital, as the resolution of the STM image depends on it. Tungsten tips are often electrochemically etched in sodium hydroxide (NaOH) solution to create a sharp end, though they are prone to oxidation over time. Pt-Ir tips, preferred for air operation due to the resistance of platinum to oxidation. The Pt-Ir

tips are usually shaped by cutting with a wire cutter. The choice of material and preparation method ensures the tip effectively contributes to the tunnelling current.

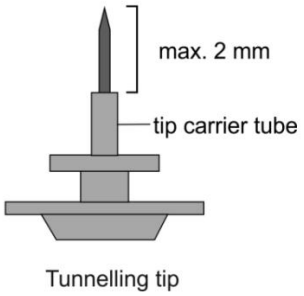

Figure 2.6 Standard tip carrier with a tip inserted in the carrier tube.

ii) Piezoelectric Scanner

This component enables precise movement of the tip in three dimensions (x, y, and z axes) with sub-angstrom accuracy. Typically, a piezoelectric tube scanner is used, which expands or contracts in response to applied voltages, allowing the tip to raster across the sample surface and maintain a constant tunnelling current by adjusting its height. A common piezoelectric material used is lead zirconate titanate (PZT).

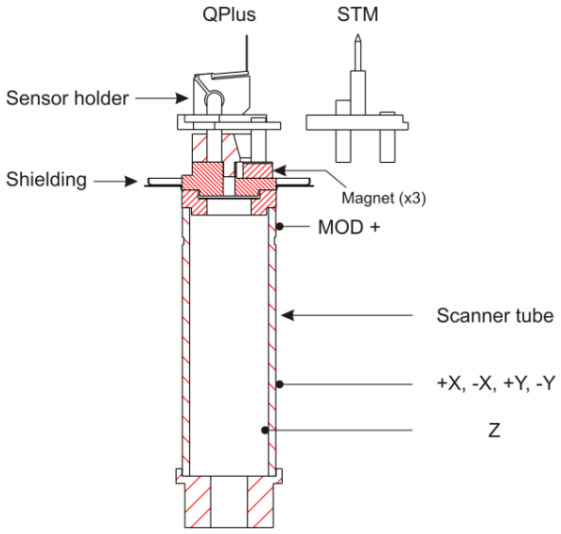

Figure 2.7 Piezoelectric scanner of LT-STM.

iii) Coarse Approach

Before the auto approach of the piezoelectric scanner, a remoting box is used to manually control the movement of the scanner base plate, so that tip position relative to the sample can be adjusted quickly.

Figure 2.8 The remoting box for manually coarse approach.

iv) Feedback Control System

A feedback system monitors the tunnelling current and adjusts the height of the tip to maintain a constant current setpoint. This feedback loop is essential for generating a 3D topographic map of the surface. In constant current mode, the tip height varies to keep the current steady, while in constant height mode, the current is measured at a fixed height, suitable for flatter surfaces.

v) Control Unit and Computer Interface

The Nanonis SPM controller controls the voltages applied to the piezoelectric scanner and process the tunnelling current signals. Users can adjust the scanning parameters (bias voltage, tunnelling current, loop gain, scanning speed, etc) through the Nanonis SPM Controller software, as shown in **Figure 2.9**.

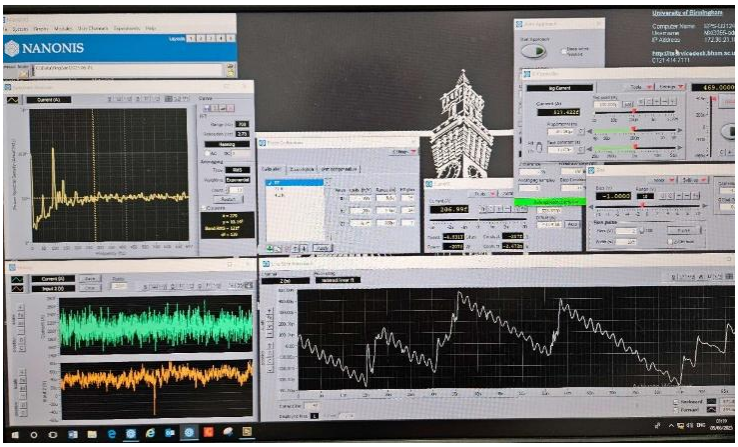

Figure 2.9 The interface of the Nanonis SPM Controller software.

1.3 Working Principle of Scanning Tunnelling Microscopy

1.3.1 Basic Working Process of STM

The core mechanism of STM is rooted in a fundamental quantum mechanical phenomenon of electron tunnelling, where particles, such as electrons, penetrate a potential energy barrier despite having insufficient energy to overcome it classically. This behaviour comes from the wave-particle duality of quantum mechanics, where the wavefunction of the particle, governed by the time-independent Schrödinger equation, extends into and through the barrier, resulting in a non-zero probability of finding the particle on the opposite side. The tunnelling probability is derived from solving the Schrödinger equation for a potential barrier, often approximated using the Wentzel-Kramers-Brillouin (WKB) method, which yields an exponential dependence on the barrier width and height[3]. In STM, this principle is applied to measure tunnelling currents between a sharp metallic tip and a conductive sample separated by a vacuum gap (typically 0.5-2 nm). A bias voltage V drives electrons to tunnel through the vacuum barrier, with the current I proportional to $e^{-2\kappa d}$, making it exquisitely sensitive to the tip-sample distance (a 1 Å change alters the current by an order of magnitude)[4]. The tunnelling current also depends on the electronic states of the tip and sample, as formalized by Bardeen's tunnelling theory, which treats the process as a transition between initial and final states across the barrier[5]. This formalism accounts for the overlap of wavefunctions and the density of states, providing a framework for understanding tunnelling in complex systems. Beyond STM, tunnelling governs phenomena like field emission, tunnel

junctions in semiconductors, and quantum devices, with applications in tunnel diodes and superconducting Josephson junctions[6].

The local density of states (LDOS) complements the tunnelling process by describing the spatial and energy distribution of electronic states available for tunnelling. In STM, the tunnelling current is proportional to the LDOS of the sample at the Fermi level, integrated over the energy window set by the bias voltage, as described by the Tersoff-Hamann model[4]. This model approximates the STM tip as a point source with an s-wave wavefunction, simplifying the tunnelling current to $I \propto \int_{E_F}^{E_F+eV} \rho_s(\mathbf{r}, E)dE$, where $\rho_s(\mathbf{r}, E)$ is the LDOS of sample at position $\mathbf{r}$ and energy E, and E_F is the Fermi energy[4]. The LDOS reflects the electronic structures of different materials, including contributions from surface states, impurities, or band edges, and is sensitive to perturbations like defects or magnetic fields. By measuring differential conductance (dI/dV), STM probes the energy-resolved LDOS, revealing features like superconducting gaps or vibrational modes[7]. The Bardeen formalism further refines this by considering the matrix element for tunnelling between tip and sample states, incorporating both LDOS and wavefunction overlap[5]. Advanced STM techniques, such as inelastic tunnelling spectroscopy, exploit LDOS variations to study electron-phonon interactions or spin excitations, making tunnelling a versatile probe of quantum phenomena[7].

The basic working process of Scienta Omicron LT STM is shown in **Figure 2.10**. The users give out the commands in the software, and the control unit then convert these commands into the corresponding voltage information to control the piezoelectric scanner. The current and height information of the sample is then transferred to the amplifier, and further transferred back to the control unit. The software can finally convert the current and height information into the STM images.

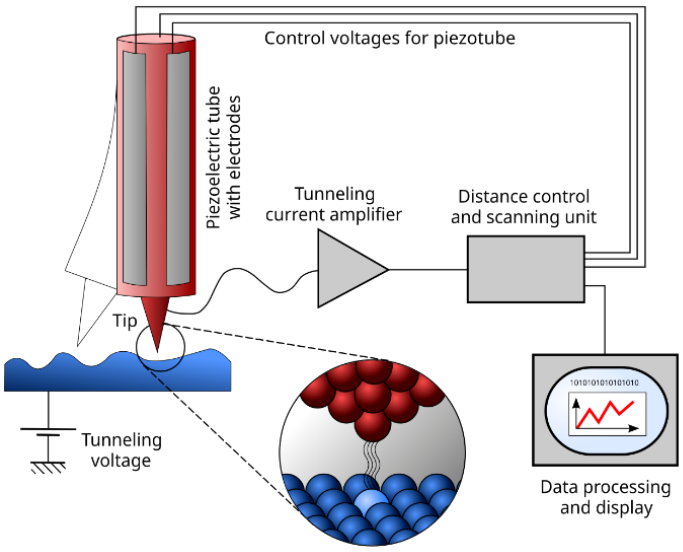

Figure 2.10 Illustration for the working principle of STM (copied from Scienta Omicron LT STM III Manual V6.0 (PN06897)).

1.3.2 Rectangular Barrier Model

The Rectangular Barrier Model describes the quantum mechanical phenomenon where electrons tunnel through a thin insulating barrier, such as in a metal-insulator-metal junction. This model simplifies the potential barrier as a rectangular shape with constant height and width, allowing for analytical treatment of the tunnelling process.

The barrier is modelled as a region of constant potential energy V_0 (barrier height) over a finite width d. The potential outside the barrier is zero or lower than V_0. Then the electrons with the energy $E < V_0$ can penetrate the barrier due to their wave-like nature. And the tunnelling current I_t arises from the net flow of the electrons tunnelling through this barrier, which is driven by an applied bias voltage. The tunnelling probability T is given by the Wentzel-Kramers-Brillouin (WKB) approximation or exact solutions to the Schrödinger equation for a rectangular barrier:

$$T \approx \exp\left(-2\int_0^d \sqrt{\frac{2m}{\hbar^2}(v_0 - E)}\,dx\right)$$

For a rectangular barrier, this equation simplifies to:

$$T \approx \exp\left(-2\,d\sqrt{\frac{2m}{\hbar^2}(v_{0-E})}\right)$$

where m is the electron mass, $\hbar$ is the reduced Planck constant, V_0 is the barrier height, E is the electron energy, d is the barrier width.

The tunnelling current I_t is proportional to the tunnelling probability, the density of states, and the applied bias voltage V. So the current is often approximated as:

$$I_t \propto V \cdot \exp\left(-2\,d\sqrt{\frac{2m}{\hbar^2}(v_0 - E_F)}\right)$$

where E_F is the Fermi energy of the electrodes, and V is the applied bias voltage.

I_t in the Rectangular Barrier Model has several key features:

i) Exponential dependence on barrier width: The current decreases exponentially with increasing barrier width d, making I_t highly sensitive to small changes in d. This is critical in applications like STM, where atomic-scale variations in distance affect the current significantly.

ii) Barrier height sensitivity: The current also depends exponentially on the barrier height V_0, which is related to the material properties of the insulator or vacuum gap.

iii) Linear voltage dependence: For small biases, I_t is approximately linear with V, but nonlinear effects arise at higher voltages due to changes in the effective barrier shape.

iv) Temperature Independence: In the ideal case, tunnelling is a quantum process and I_t is largely temperature-independent, unlike thermionic emission.

2. Ultra-High Vacuum System

In UHV systems, the pressure range is typically between 10^{-7} and 10^{-11} mbar. To maintain a good vacuum level within the whole STM chamber, a system consists of several types of pumps is designed and installed to the chamber. The pumps used in our UHV system include: rotary pump, turbo pump, ion pump and titanium sublimation pump (TSP).

Rotary pump is the very initial part of the UHV system. Through changing the volume of the suction chamber inside the pump periodically, the gas in the container is continuously expanded to the suction chamber through the pump inlet and then discharged from the pump through the exhaust port by compression. The rotary pump can reduce the pressure in the chamber down to about 10^{-2} mbar, which is low enough for turbomolecular pump to work.

Turbomolecular pumps are the most commonly used pump in UHV systems, due to their ability to reduce the pressure down to about 10^{-9} mbar. The gas molecules entering the molecular pump collided by the rotating vanes, gaining more momentum and starting to move in a directional manner. Eventually these molecules are discharged out of the chamber. However, if there are some molecules which are too large or too small inside the chamber, such as H_2O and H_2, it would be hard for the turbomolecular pumps to pump them out.

Ion pump works by continuously ionizing the ions and accelerating them with a high voltage (3 - 7 kV). The gas molecules will be trapped by these ions and finally being physically trapped at the adsorption surface of the ion pump. With the ion pump, the pressure can be reduced to about 10^{-11} mbar, which has met the requirements for UHV system.

TSP works through periodically applying the current to the titanium wire to bring it to sublimation temperature. The sublimated titanium will then form a titanium film on the inner surface of the chamber, which has a strong adsorption on the reactive gases, such as CO. When the TSP works together with an ion pump, the pressure of the chamber can be reduced to below 10^{-11} mbar.

3. Sample Preparation and Tip Etching Instruments

3.1 Molecular Evaporation Source

Molecular evaporation source is a specialized device used in vacuum deposition techniques, such as thermal evaporation and molecular beam epitaxy (MBE)[8], to deposit thin films of materials onto substrates. As the temperature of material increases, the atoms or molecules gain sufficient kinetic energy to overcome intermolecular forces, transitioning into the vapor phase. This process occurs under high vacuum conditions to prevent unwanted reactions and ensure a mean free path long enough for the vapor to travel to the substrate without collisions.

Usually, there are several mostly used types of molecular evaporation source:

i) Resistive Heating: An electric current passes through a resistive element (like a tungsten filament), generating heat that melts and evaporates the material.

ii) Electron Beam (E-Beam) Heating: An electron beam is directed at the material, providing localized heating suitable for materials with high melting points.

iii) Induction Heating: An alternating magnetic field induces eddy currents in the material, generating heat through electrical resistance.

3.2 Ion Gun

Ion gun is a useful tool for sample preparation, as it can deeply clean the sample surface through the ion sputtering. The sputtering process begins with the generation of ions, typically using an inert gas such as Ar. Electrons emitted from a heated filament are accelerated into a chamber containing the Ar gas, ionizing the Ar atoms through collisions. This creates a plasma composed of positive ions and electrons. Then, the Ar^+ ions are extracted from the plasma and accelerated towards the target material by applying a high voltage (1.0 - 2.0 kV). Electrostatic lenses and grids focus and direct the ion beam precisely onto the target surface. When these high-energy Ar^+ collide with the target surface, they transfer momentum to the atoms in the solid. If the transferred energy exceeds the surface binding energy, atoms are ejected from the surface, which is known as sputtering.

3.3 Thermal Annealing and Cooling

3.3.1 Heating

i) Radiation annealing: The thermal annealing for the sample is through the PBN heater on manipulator, which could heat the sample up to 700 °C.

ii) Direct current annealing: The direct current heating is for the sample like silicon, which could rapidly heat the sample up to 1400 °C.

3.3.2 Cooling

The cooling of the sample is through a cooling wire connected to the cooling block, which is installed at the very end of the STM manipulator. To cool down the temperature of the sample, the

cooling wire need to be filled with LN_2 through one end, and the nitrogen is then vented from the other end of the cooling wire. The cooling efficiency is limited through this cooling wire, and the sample temperature can be cooled down to about 100 K.

3.4 Tip Etching Device

The tip etching device is shown in **Figure 2.11** (a). The tungsten wire of 0.25 - 0.4 mm diameter is cut into approximately 5 cm length, and then the tungsten wire is connected to a metal tip holder. The end of the wire is inserted into the 1 mol/L sodium hydroxide solution for about 2 mm to obtain a sufficiently pointed tip by electrolysis, as shown in **Figure 2.11** (b). The electrochemical reaction process for tip preparation is: $W(s) + 2OH^- + 2H_2O \rightarrow WO_4^{2-} + 3H_2(g)$.

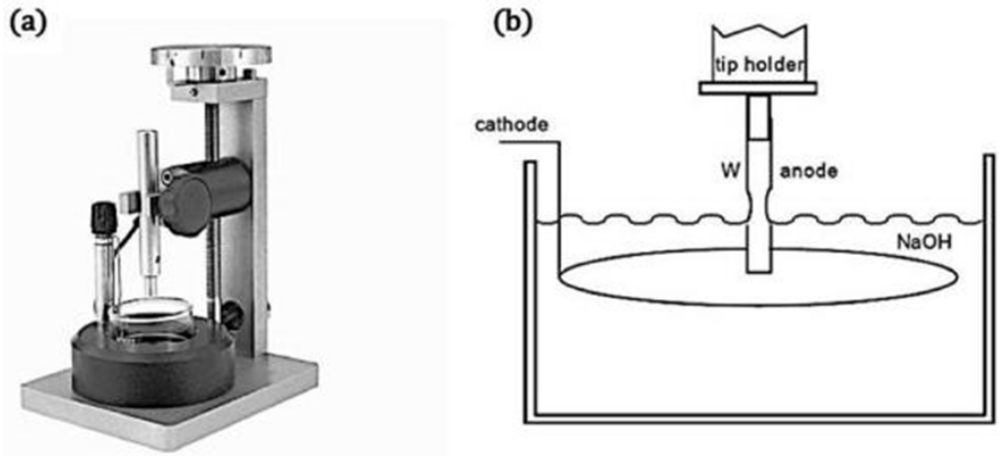

Figure 2.11 (a) The tip etching device. (b) Illustration for the tip etching process.

4. Software

4.1 Scanning Control

The software that supports this controller and the STM system is 'Nanonis SPM Controller' (Version 4.8.181) and 'Scan Inspector' (Version 4.4.10).

4.2 Data Processing

The raw data of STM includes the tunnelling current information and the height information collected from the sample. Usually, the raw data needs to be processed to make the images clear or emphasise certain information in the images.

The software used in our group is 'Gwyddion' (Version 2.61).

References

[1] Wiesendanger, R. *Scanning Probe Microscopy and Spectroscopy*; 1994.

[2] Binnig, G.; Rohrer, H.; Gerber, Ch.; Weibel, E. Surface Studies by Scanning Tunneling Microscopy. *Phys. Rev. Lett.* **1982**, *49*, 57–61.

[3] Griffiths, D. J. *Introduction to Quantum Mechanics*; Cambridge University Press: Cambridge, 2017.

[4] Tersoff, J.; Hamann, D. R. Theory of the Scanning Tunneling Microscope. *Phys. Rev. B* **1985**, *31*, 805–813.

[5] Bardeen, J. Tunnelling from a Many-Particle Point of View. *Phys. Rev. Lett.* **1961**, *6*, 57–59.

[6] Wolf, E. L. *Principles of Electron Tunneling Spectroscopy*; Oxford University Press, 2012.

[7] Feenstra, R. M. Scanning Tunneling Spectroscopy. *Surf. Sci.* **1994**, *299-300*, 965–979.

[8] Meyers, R. A. *Encyclopedia of Physical Science and Technology*, 3rd ed.; Academic Press, Cop: San Diego, 2001.

IV. C_{70}/Decanethiol Self-Assembled Structures at RT

1. Introduction

The self-assembly of bi-component system has been widely studied. Among various molecules used in this system, fullerene molecules and thiol-based compounds are of particular interest due to their electronic properties, superior stability in the ambient and compatibility with gold substrates[1]. In previous studies, it is found that C_{60} can form various two-dimensional self-assembled structures with alkanethiols on Au(111) substrate. Zhang *et al.* reported a kind of C_{60}/octanethiol supramolecular framework[2], Zeng *et al.* reported the formation of the C_{60} bimolecular chains in between the striped phase decanethiol[3], Li *et al.* reported the confined C_{60} islands grown within the octanethiol SAMs[4], Ding *et al.* reported a kind of C_{60}/decanethiol 2D porous network[5].

The C_{70}, which are electronically similar with C_{60}, has a rather different geometry.[6] The difference in molecular shape will strongly affect the final self-assembled structures, as the intermolecular interactions between different molecules vary. C_{70} is an ellipsoid-shaped molecule with a short and a long axis. Its short axis, with the length of 7.178 Å[7], is close to the diameter of C_{60} (7.065 Å)[8], while its long axis is 7.906 Å, which is about 12% longer than the dimeter of C_{60}. And the carbon atoms from the alkane chains of decanethiol (DT) can interact more efficiently with the carbon atoms from C_{70}, because the C_{70} is larger in size, which makes there is relatively more carbon atoms interact with the carbon atoms from DT alkane chains. On the other hand, the binding energies vary when C_{70} contacting the substrate with different faces[9], as different amount of carbon atoms have contributed to the van der Waals force. Overall, C_{70} introduces additional complexity and opportunities for forming unique structures on the Au(111) substrate. Comparative studies of the C_{70}/DT and C_{60}/DT systems can help us to hypothesise the self-assembled structures of other fullerene-alkanethiol systems.

Our work in this chapter investigates the formation mechanisms and the structural details of the C_{70} fullerene and δ phase DT system on the Au(111) surface at RT. Furthermore, these findings

also have implications for understanding the role of van der Waals forces and the weakly interacting nature of the system in determining the final two-dimensional self-assembled architecture.

2. Sample Preparation

The substrate for the sample in this experiment is a (111)-oriented gold thin film grown on highly oriented pyrolytic graphite (HOPG) block. The HOPG used is ZYB grade, and the top few layers are peeled off with adhesive tape to generate a brand-new surface which is sufficiently flat and clean. The gold film is grown on the HOPG substrate using a BOC Edward 306 vacuum evaporator. A piece of gold wire (99.99% pure) placed in the heating boat is heated up to approximately 1100 °C, and the HOPG is also heated to approximately 350 °C before it is exposed to the gold vapor. Heating the HOPG during film growth helps to grow samples with large atomically flat terraces. The vacuum inside the evaporation chamber during sample preparation is around 10^{-5} ~ 10^{-6} mbar. The thickness of the prepared Au(111) film is about 300 nm. Then the Au(111) film is transferred into the preparation chamber of LT-STM in UHV system. This sample transfer process involves exposing the sample to air for a few hours. Once inside the UHV system, the Au(111) film is treated by several cycles of Ar^+ ion sputtering and thermal annealing. Ion sputtering removes contaminants from the Au(111) surface, and the sputtering energy is set to 1.5 keV, lasting for 7 minutes in each cycle. The thermal annealing is conducted on the manipulator in the preparation chamber. The sample is heated up to 550 °C, so that the contaminants in deeper layers of gold film can be brought to the surface, and then be removed through further ion sputtering. The Au(111) film is repeatedly cleaned until the surface is almost free of contaminants, which can be checked with STM imaging at RT.

After the flat clean Au(111) film is prepared, it is taken out from the preparation chamber and then immersed into a 1 mM 1-decanethiol solution in ethanol (99.5%). The sample is left in the solution for 12 hours at RT. Later the Au(111) is taken out from solution and dried through blowing with dry nitrogen. The DT/Au(111) sample is transferred back to the preparation chamber, which needs to be annealed to reduce the coverage of DT before adding C_{70} to the surface. The DT/Au(111) sample is heated to 120 °C for 1 hour on the manipulator while keeping the pressure in the preparation chamber at $< 1.0 \times 10^{-8}$ mbar. Through the partial thermal desorption, the reduction of

DT coverage results in the transition from the closed-packed phase of DT (0.33ML)[10] to a low coverage δ phase (0.23ML)[11].

The C_{70} molecules are subsequently deposited on the δ phase DT/Au(111) sample at RT. The evaporation source of C_{70} is heated up to 409 °C, and the deposition time is 1 minute. About 0.3 ML of C_{70} are deposited on the sample. Finally, the prepared C_{70}/DT/Au(111) sample is transferred to the analysis chamber of the LT-STM for imaging.

3. Results and Discussion

The scanning of the sample is conducted in UHV (~ 1.0×10^{-11} mbar) at RT (~ 290 K) after each step of preparation. **Figure 4.1** (a) shows a 75 nm × 75 nm area on the Au(111) film after several cycles of ion sputtering and thermal annealing, which is clean and flat enough to be used as a substrate for the subsequent deposition. There is nearly no contaminant left on the surface, and the herringbone reconstructions of Au(111) surface can be observed clearly. After the liquid phase deposition of DT, the Au(111) surface is covered by close-packed φ phase DT, and the DT in this φ phase then changed into δ phase due to partial desorption of DT after 120-degrees annealing, as shown in **Figure 4.1** (b). In this area, most of DT arrange into the δ phase, while in some of regions DT still arrange as the φ phase. After roughly calculating the coverage of DT in these two phases in different regions of Au(111) substrate, we found that there are over 90% DT are in δ phase, and the rest of DT are in φ phase. It indicates that there is temperature difference across the sample surface during the thermal annealing, thus the DT do not evenly desorb form the substrate, and the overall coverage of DT after annealing is close to, but still slightly higher than the theoretical coverage of δ phase DT. Fortunately, this coverage of δ phase DT have met our requirement for the further deposition of C_{70}, that there is enough space for C_{70} landing on the Au(111) substrate rather than on the top of DT alkane chains. The C_{70} molecules on the sample are found to be disordered initially after the deposition of C_{70}, as shown in **Figure 4.1** (c). The average coverage for this disordered C_{70} phase is calculated to be about 0.044 ML, and as the amount of C_{70} is higher than we expected, the deposition temperature of C_{70} is reduced for the later sample preparation. After the sample is left at RT for 24 hours, some ordered self-assembled structure started to form, and it takes about 72 hours for the formation of large area of ordered structures. **Figure 4.1** (d) shows the C_{70}/DT/Au(111) sample 72 hours after deposition, and most of C_{70} are stabilised by the

alkane chains of DT, though these chains are not visible at RT in this image due to their mobility and poor charge conductivity[12]. Without the incorporation of DT molecules, C_{70} would collapse into a closed-packed layer. The presence of DT molecules within the C_{70} dimer rows will be revealed with LT imaging in the next chapter. This area contains two types of C_{70}/DT ordered structures, the C_{70}/DT dimer row structure and the C_{70}/DT porous framework.

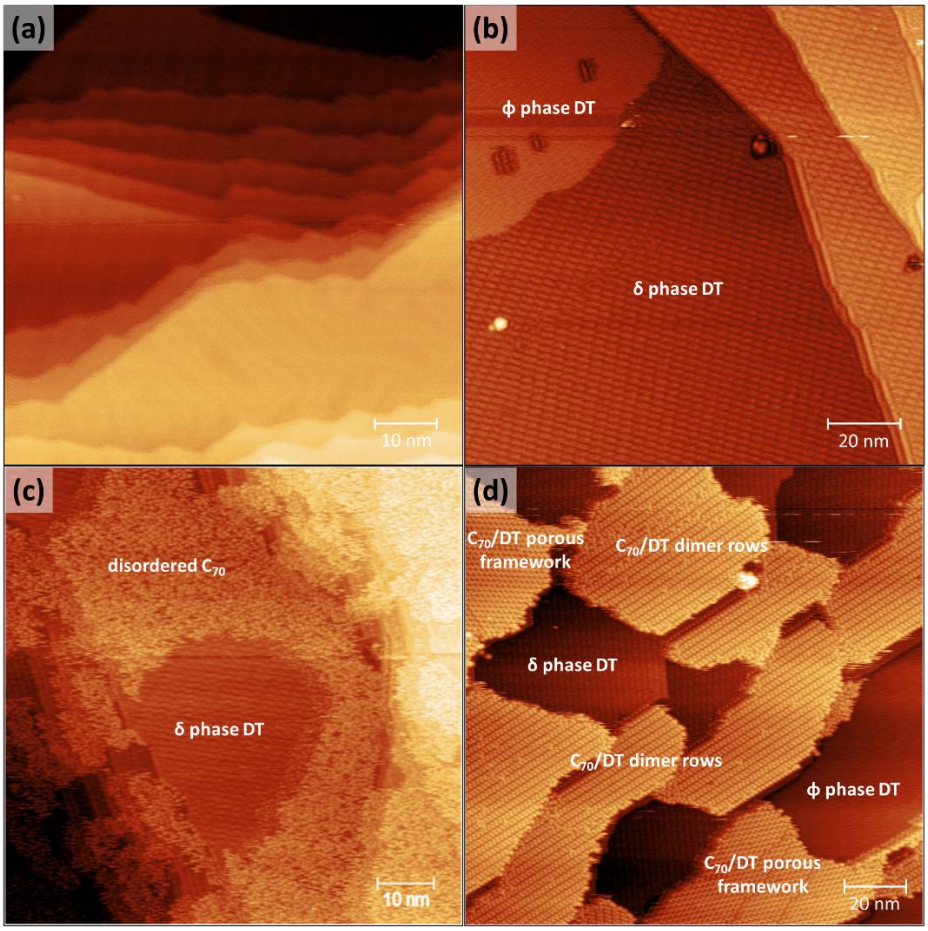

Figure 4.1 (a) The Au(111) substrate after ion sputtering and thermal annealing. (b) The DT/Au(111) sample after annealed at 120 °C for 1 hour. Most of DT arranged into δ phase and some of the DT remained in φ phase. (c) The C_{70}/DT/Au(111) sample 24 hours after the deposition. The scanning parameters are: I = 100 pA, V_{bias} = 1.6 V. No regular structure has been formed yet. The C_{70} molecules are mobile. (d) The C_{70}/DT/Au(111) sample left at RT for over 72 hours. The scanning parameters are: I = 120 pA, V_{bias} = 1.5 V. The C_{70}/DT dimer row structure, the C_{70}/DT porous framework, the δ phase DT and close-packed DT are found coexisting on the sample.

The coverage of these two structures is found to be different, and C_{70}/DT dimer row structure is more common, which indicates that the stabilities or formations of two structures are different. To find out the possible reason for these differences, the sample is then annealed from 60 °C to 120 °C with temperature changing by 10 °C in each step, and the results will be discussed later.

3.1 C_{70}/Decanethiol Dimer Row Phase

3.1.1 Measurements and Details

Figure 4.2 (a) shows a large area of C_{70}/DT dimer row phase. The C_{70}/DT dimer rows are found to be parallel to the $[11\bar{2}]$ direction, which is the same direction as that of the DT rows in the δ phase[13]. It is also found that at some position, the C_{70} and DT form trimers rather than dimers. The existence of C_{70}/DT trimer rows do not affect the overall dimer row phase. While on some narrow terraces, disordered C_{70} domains remain without any sign of the formation of the ordered structure. It appears that a minimum terrace width of ~ 7 nm is required for the formation of stable dimer rows. Between the regular C_{70} dimer row phase and the δ phase of DT, it is interesting to notice that there is a sharp boundary rather than a gradual transition region. The lack of a transition region with a DT coverage higher or lower than that of the δ phase suggest that the number of DT molecules from the δ phase is just about right to construct the regular C_{70}/DT structure. If there are much more DT molecules provided by the δ phase than that are needed for the formation of the dimer rows, excess DT molecules would have been observed to accumulate at the boundaries between the δ phase and the dimer row phase.

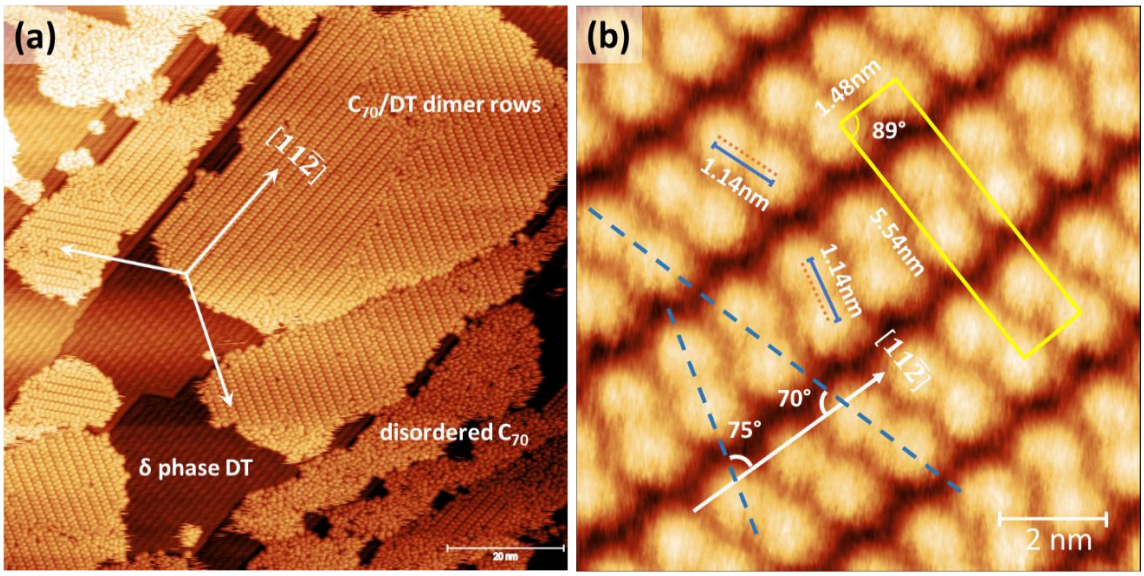

Figure 4.2 (a) The large area of C_{70}/DT dimer row islands. The direction of dimer rows follows the direction of δ phase DT, which is along the [11$\bar{2}$] direction and the other two equivalent directions. Some of disordered C_{70} are observed at right corner of (a). (b) The measured distances of pure C_{70}/DT dimer row structure. The unit cell is marked in yellow, which is close to, but not a rectangular cell as the angle between the short and the long side is 89 degrees. The distance between two C_{70} within the dimer is 1.14 ± 0.02 nm, and that corresponds to the distance between two close-packed C_{70} molecules. The gap in between the C_{70} dimers is filled by DT molecules, but they are not visible at RT.

In order to construct a structural model for the ordered C_{70}/DT phase, we have conducted careful measurements of lattice parameters which are displayed in **Figure 4.2** (b). The distance between two neighbouring C_{70} dimers along the [11$\bar{2}$] direction is 1.48 ± 0.02 nm, which is close to $3\sqrt{3}a$ ($a \approx 2.88$ Å)[14]. The distance between the two C_{70} molecules within the dimer is 1.14 ± 0.02 nm, which is close to the distance between the lying down close-packed C_{70} molecules.[15] At RT, the lying down C_{70} molecule behaves like a free rotor, so its footprint is dominated by the dimension of the long axis. The unit cell of C_{70}/DT dimer row structure is shown by the yellow parallelogram in Fig. 4.2(b), and the parameters are: a = 5.54 nm, b = 1.48 nm, γ = 89°. The cell is pretty close to a rectangular one. Due to experimental uncertainties, we will consider the possibility of a rectangular unit cell later. The C_{70} dimers occupy the Au(111) surface in two different orientations, respectively with the dimer axis keeping an angle of either 70° (clockwise) or 75°

(counterclockwise) off the $[11\bar{2}]$ direction. And the axis of C_{70} dimers within the same dimer row keeps the same orientation.

Different from the C_{60}/DT dimer row structure in which the C_{60} dimer axis in each two adjacent dimer rows can keep the same orientation, the C_{70} dimer axis in adjacent dimer rows always switch directions. That indicates C_{70} from the dimer rows in different orientation may occupy different sites on the Au(111) surface. As the interaction between C_{70} and gold substrate is weak[16,17], to keep a stable and long-range ordered structure with DT molecules, all C_{70} molecules may not take the same adsorption site or orientation in order to optimise their interactions with DT. The other possibility is that C_{70} dimer rows have their preferred spacing distance, while the available binding site between the gaps of dimer rows may be not equivalent for DT molecules as the Au adatoms of RS-Au-SR staples have to occupy the bridge sites of Au(111) substrate. As the occupations of DT are different, which makes the molecular interactions between C_{70} and DT in different gaps inequivalent, one of C_{70} dimer rows may be squeezed by DT and change their orientations. It is hard to find out the reason at RT, as both molecules are still free to rotate and diffuse on the surface. This will be further discussed in chapter V with the LT data.

We then focus on the C_{70}/DT trimer row structure. The C_{70}/DT trimer row structure can always be found within the large dimer row domains, but the trimeric C_{70} does not form a domain consisting only of C_{70} trimers, which behaves differently from the C_{70} dimers. **Figure 4.3** (a) shows a C_{70}/DT trimer row within the dimer row phase. The whole trimer row grows along $[11\bar{2}]$ direction as well, and the two sides of trimers are respectively along 40° (clockwise) and 48° (counterclockwise) off the $[11\bar{2}]$ direction. In comparation with the standard dimer rows, the trimer row occupies less space in $[1\bar{1}0]$ direction. The distance between two standard dimer rows in same orientation is 5.53 ± 0.03 nm (≈ 19a), and for the dimer rows with a trimer row in the middle, that distance is 4.27 ± 0.03 nm (≈ 15a). Though the existence of trimer row changes the local distance of dimer row phase, the overall dimer row structure is not affected.

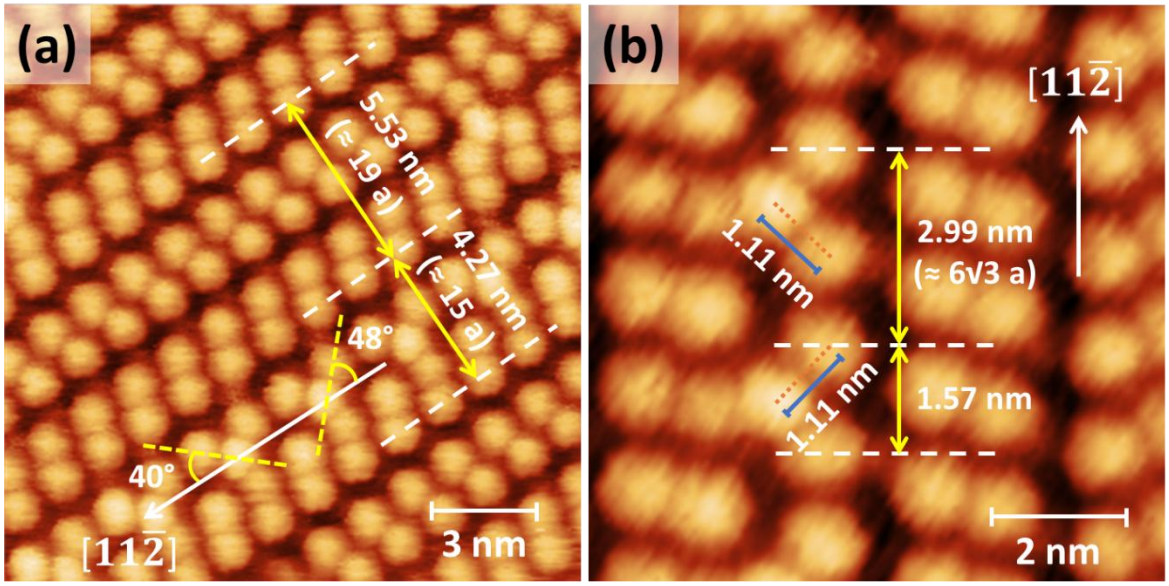

Figure 4.3 The C_{70}/DT dimer row phase with a single trimer row in the middle. The whole dimer row grows along [11$\bar{2}$] direction, and the neighbouring C_{70} within the trimer row keep the angles of 40° (clockwise) and 48° (counterclockwise) to the [11$\bar{2}$] direction. The distance between two dimer rows in the same orientation are found to be different. The standard distance is measured to be 5.53 ± 0.03 nm, and the distance reduce to 4.27 ± 0.03 nm with the formation of trimer row. (b) The details of C_{70}/DT trimers.

The details of C_{70}/DT trimer row structure are shown in **Figure 4.3** (b). As the trimer row does not extend along [1$\bar{1}$0] direction forming a separate phase, we can only measure the repeating distance of C_{70}/DT trimers, which is 2.99 ± 0.02 nm (≈ 6√3a) along [11$\bar{2}$] direction. The distances between two neighbouring C_{70} are both measured to be 1.11 ± 0.02 nm, which are close to the distance between C_{70} in the close-packed phase.[15] And the distance between two C_{70} along [11$\bar{2}$] direction is 1.57 ± 0.02 nm. Compared with the dimer row, the trimer row contains less C_{70} in corresponding area, and the coverages of C_{70} and DT would be different for these two structures. The coverage of C_{70} and DT will be discussed in detail in the next chapter.

3.1.2 Formation of C_{70}/DT Dimer Row Structure

As previously mentioned, it takes about 24 hours for a small area of C_{70}/DT dimer rows to from. These initially formed dimer rows are all found within the large disordered C_{70} regions, as shown in **Figure 4.4** (a) and (b). The region marked in yellow dashed frame in **Figure 4.4** (a) is the smallest dimer row phase we observed. This initial C_{70}/DT dimer row phase is found to consist of

at least three rows, which could be the smallest unit needed to keep this structure in place. **Figure 4.4** (b) shows the larger regions of dimer row phase, and these regions are within the large domains of disordered C_{70}. It indicates that a critical number of dimer rows is requited for the structure to grow, and the coverage of C_{70} in the dimer row phase could be close to the coverage of disordered C_{70} (0.044 ML). However, the formation of the very beginning unit in **Figure 4.4** (a) is not directly observed. We then refer to C_{60}/DT system, which is similar with C_{70}/DT system. According to the formation of C_{60}/DT self-assembled structures[18], it is possible that C_{70} also form the dimer first. Then the dimerized C_{70} rotate and diffuse locally, interacting with the alkane chains of DT molecules. When some of the molecules find their preferred site positions and the C_{70}-DT ratio match with the specific requirement (1 : 3), the C_{70}/DT dimer rows are formed.

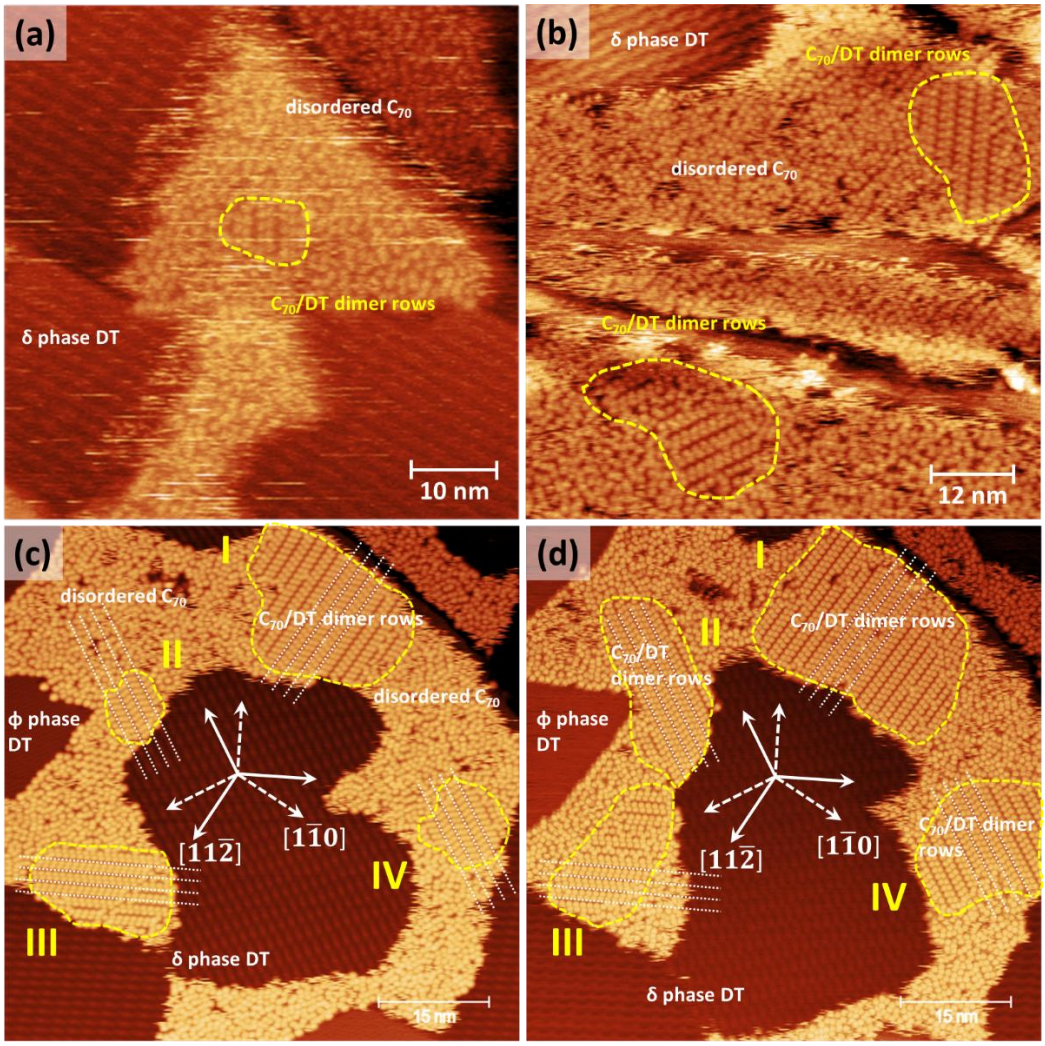

Figure 4.4 (a) The C_{70}/DT/Au(111) sample about 24 hours after deposition of C_{70}. The region marked in yellow dashed frame is the very beginning unit of C_{70}/DT dimer row phase. (b) The STM image took a few hours later than (a). The dimer row phases grow larger and they are all found within the large disordered C_{70} domains. (c) STM image of C_{70}/DT sample at RT about 48 hours after deposition of C_{70}. The ordered dimer row phase marked in yellow dashed frames is observed to coexist with the δ phase of DT and φ phase DT. The white dashed lines in each region are along $[11\bar{2}]$ direction, representing the corresponding positions in (d). (d) The STM image took at the same area 8 hours later. The dimer row phase in each region grows along both the $[11\bar{2}]$ and $[1\bar{1}0]$ directions.

Once the initial dimer row units formed, more rapid growth is observed to form an extended two-dimensional dimer row lattice. **Figure 4.4** (c) and (d) shows the growth of C_{70}/DT dimer rows over

an eight-hour period. The dimer row regions are marked with yellow dashed lines in **Figure 4.4** (c). These regions are different in size, which indicates that the dimer rows in different regions were not formed at the same time. In comparation with **Figure 4.4** (d), the dimer rows in all the corresponding regions expand along either the $[11\bar{2}]$ or the $[1\bar{1}0]$ direction. The white dashed lines represent the corresponding locations in each region. In region I, the dimer row structure expands in the $[1\bar{1}0]$ direction because there is plenty of supply of C_{70} molecules in that direction from the reservoir of the disordered C_{70} phase. In region II, the dimer rows mainly grow along the $[11\bar{2}]$ direction expanding into the region of disordered C_{70}, **Figure 4.4** (c). The expansion of region III is similar with region I, but some of C_{70} form the trimer row in the middle of region III in **Figure 4.4** (d). The possible explanation is that region III is at the boundary of two δ phase DT domains, where the DT behave differently than those within the δ phase, and the final C_{70}/DT structure is also affected. The formation of C_{70}/DT trimer rows will be discussed later. For region IV, as this region in **Figure 4.4** (c) is within the domain of disordered C_{70}, the dimer row phase is available to grow along both the $[11\bar{2}]$ and $[1\bar{1}0]$ directions. The ordered phase will keep growing at RT until most of disordered C_{70} are consumed, as shown in **Figure 4.1** (d).

To find out how exactly the C_{70}/DT dimer row phase grows, we scanned the sample continuously at the boundaries of the dimer row islands. **Figure 4.5** (a) and (b) are the STM images acquired at RT, showing the growth of dimer row phase along the $[11\bar{2}]$ and $[1\bar{1}0]$ directions, respectively. **Figure 4.5** (a) shows the phase growth along the $[11\bar{2}]$ direction. The dimer row marked in yellow dashed frame is the same location of this dimer row domain, and the red dashed frame represents the extension part of the dimer row. It can be found that at the beginning, some free C_{70} already diffuse to the boundary and gather as a single row. Then these C_{70} keep moving along $[11\bar{2}]$ direction and 'drop' to the end of the pre-existing dimer row. The DT molecules at this position are pushed away and rearrange around the extending dimer row, stabilizing the newly added C_{70} through the alkane chains. Then, more of the disordered C_{70} gradually join the dimer row, as highlighted in the red dashed frame in **Figure 4.5** (a). And the expansion of this domain will last until it reaches the terrace of gold substrate or the free C_{70} around are all consumed to form dimer rows.

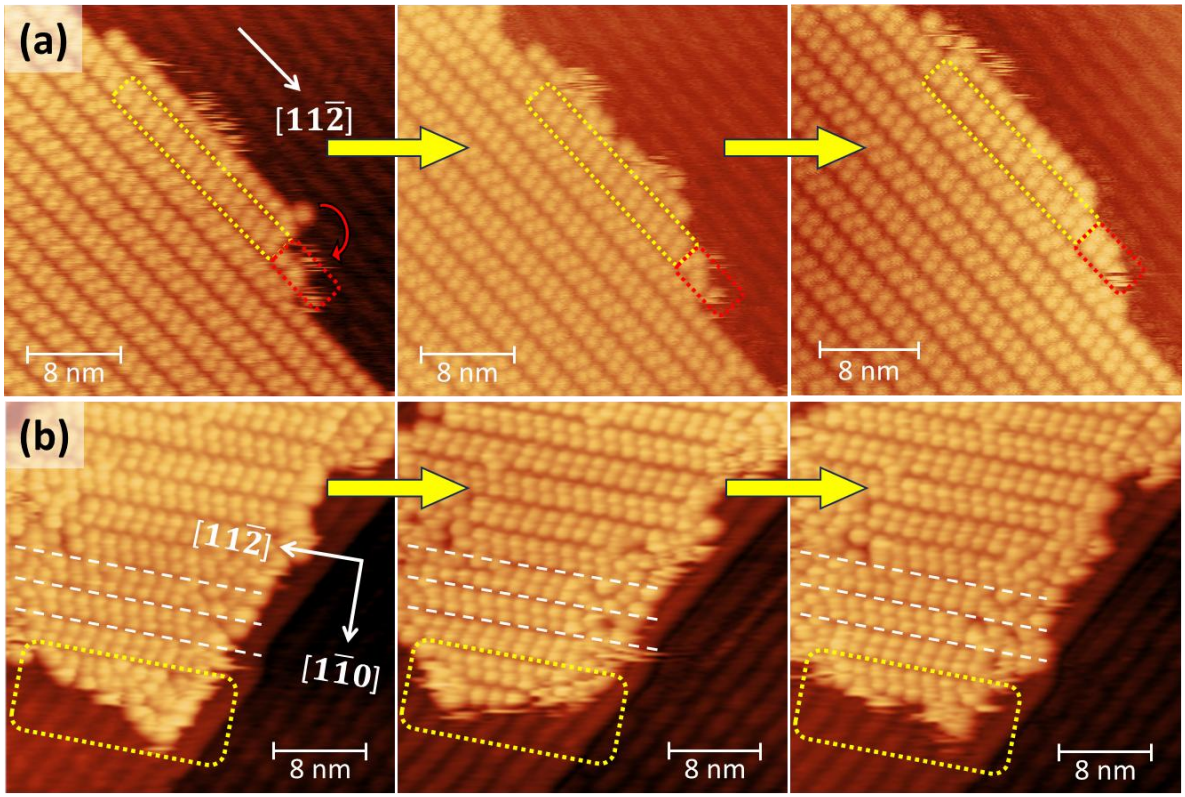

Figure 4.5 (a) The growth of C_{70}/DT dimer row phase along the [11$\bar{2}$] direction. The dimer row marked in yellow dashed frame is the corresponding location. The free C_{70} diffuse to the edge of dimer row domain, forming a single row. These C_{70} then keep moving along the [11$\bar{2}$] direction, and join the pre-existing dimer row, as marked in red dashed frame. (b) The growth of C_{70}/DT dimer row phase along the [1$\bar{1}$0] direction. The white dashed lines represent the corresponding dimer rows in (b). As this dimer row phase is close to the gold terrace, the free C_{70} cannot diffuse further, and then they gather here, forming a new dimer row.

Figure 4.5 (b) shows the phase growth along [1$\bar{1}$0] direction. The white dashed lines represent the corresponding locations of the dimer row region. The free C_{70} molecules contributing to the phase expansion are from the disordered C_{70} domain on the lower left of this dimer row region. When C_{70} diffuse to the boundary of dimer row phase, they are obstructed and gather here as they are close to the gold terrace. As shown in the yellow dashed frame, the disordered C_{70} interact with the DT, forming a short dimer row gradually. And then with more C_{70} involved, the new dimer row grows longer along the [11$\bar{2}$] direction or the other two equivalent directions ([1$\bar{2}$1], [$\bar{2}$11]) till it reaches the edge of gold terrace.

In comparison of the dimer row phase growth in two different directions, the phase growth along the $[11\bar{2}]$ direction seems to be easier, which may be related to the way DT bind to the Au(111) surface and how they diffuse. The DT rows in the δ phase run along the $[11\bar{2}]$ direction[19], and there are some gaps between the two rows of RS-Au-SR staples, where are filled with the high flexibility wobbling alkane chains of DT. When C_{70} are deposited on the δ phase DT/Au(111) surface, some C_{70} directly land into the gaps, whilst others land on top of DT. Due to the mobility of alkane chains at RT[20], the C_{70} land on DT will then drop onto the gold substrate, where the C_{70} can be more stable. These C_{70} will keep diffusing at RT, but not as free as on the pure Au(111) surface. As introduced in chapter II, each AAD unit contains one Au adatom pulled out from the gold substrate, occupying the bridge site of Au(111) substrate. These Au adatoms arrange along the $[11\bar{2}]$ direction, forming regular-spaced tiny Au barriers, of which the height is about 1a (a = 0.288 nm). When C_{70} travel along the $[1\bar{1}0]$ direction (perpendicular to the $[11\bar{2}]$ direction) on the Au(111) substrate, they have to cross over these tiny Au barriers, which indicates that the diffusion of C_{70} in this direction is obstructed. While when C_{70} travel along the $[11\bar{2}]$ direction, there is no such a barrier, thus it is easier for C_{70} to diffuse in this direction. Before the ordered C_{70}/DT phase formed, the disordered C_{70} keep pushing each other, making the diffusion of C_{70} almost evenly in different directions. Later on, with the formation and expansion of the C_{70}/DT dimer row phase, more and more C_{70} are stabilised, and the rest disordered C_{70} gradually diffuse along the boundary of these ordered phase.

Overall, it is easier for the C_{70} to diffuse through the gaps along $[11\bar{2}]$ direction, forming a single row at the boundary of dimer row phase as shown in **Figure 4.5** (a). The phase growth along $[1\bar{1}0]$ direction requires either to overcome the Au barriers, or the diffusion along $[11\bar{2}]$ direction to be obstructed by the boundaries of different DT domains or gold terraces. And that could be the reason for C_{70}/DT dimer row phase grow differently in $[11\bar{2}]$ and $[1\bar{1}0]$ directions.

As mentioned previously, during the formation of the dimer row phase, C_{70} and DT will occasionally form the trimer rows rather than dimer rows. The formation of the trimer row is shown in **Figure 4.6** (a) to (f), marked in yellow dashed frames. It is interesting to note that the formation of this trimer row starts from an unfinished dimer row growing along the $[1\bar{1}0]$ direction, as shown in **Figure 4.6** (a). This dimer row grows from both two sides towards the middle, which may cause a competing between these two 'half' dimer rows. Then in (b), the 'half' dimer row on the right

break into disordered C_{70}, and in (c) they reform as a single row with three C_{70} trimers on the two sides. This single row is broken again in (d) as more disordered C_{70} from the right side diffuse into this region, while the C_{70} trimers on the right are not affected. Later on, the left 'half' dimer row is broken as well, and the C_{70} start to reform as the trimer. Finally, in (f), a whole C_{70}/DT trimer row form in the place of the previous unfinished dimer row. It is also found that in **Figure 4.6** (f), on the other side of C_{70}/DT trimer row, a new dimer row already starts to form, which further indicates that the trimer row structure will not affect the formation of C_{70}/DT dimer rows.

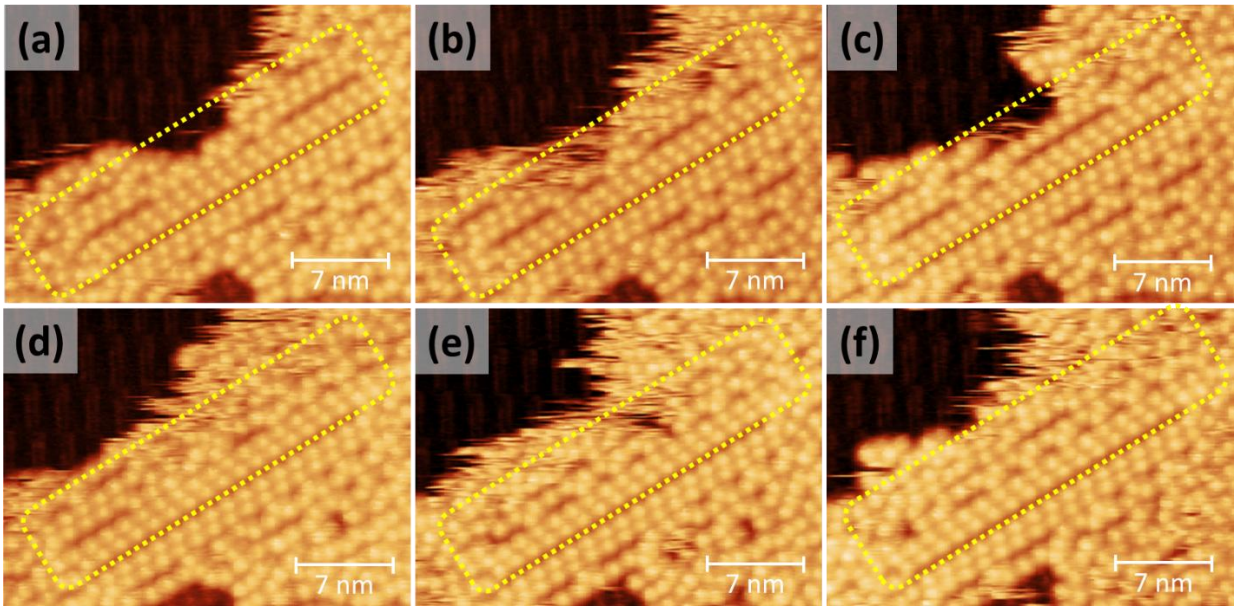

Figure 4.6 The formation of the C_{70}/DT trimer row. The phase change of C_{70}/DT from dimer row to trimer row is shown in the region marked in yellow dashed frame. The structure in this region changes from two 'half' dimer rows to disordered phase, and finally stabilise as a trimer row.

So, what are the factors that drive the C_{70} and DT to form the trimer row structure? Comparing the details of C_{70}/DT dimer row structure and trimer row structure, as shown in **Figure 4.3** (a), it is noticed that the space occupied by trimer row is always less than that of dimer row (about 4a difference in width in $[1\bar{1}0]$ direction). According to this feature, one of the possible explanation is that the formation of the trimer row structure is due to the limited space. As we introduced, the C_{70}/DT dimer row structure is able to form in any suitable domains. When two C_{70}/DT dimer row domains gradually expand and finally reach the boundaries of each other, the space between these domains could not be large enough for a new C_{70}/DT dimer row to exist, and the molecules at the

boundaries would rearrange into trimer row structure, which requires less space to exist. In this way, the space in between different domains is effectively occupied, and the molecules at the boundaries are thus stabilised. In addition, that could also happen within one single large domain, when there is no enough space left in between two C_{70}/DT dimer row regions, the molecules at the boundaries of these regions would also rearrange into the trimer row structure to stabilise the whole domain.

The other possible explanation for the formation of C_{70}/DT trimer row structure is the compression of DT. During the formation of C_{70}/DT dimer row phase, the C_{70} take some place of pre-existing δ phase DT. Some of DT participate in the formation of C_{70}/DT dimer rows, while the other DT are pushed away from their binding sites, diffusing around. However, as we mentioned before, there is no clear boundary between C_{70}/DT dimer row phase and the δ phase DT, which means the pushed away DT are not gathering at the boundaries of dimer row phase. The exceed DT either desorbed from Au(111) surface or occupied some other space inside the dimer row phase. Back to our analysis for C_{70}/DT trimer row, as shown in **Figure 4.3**, there are less C_{70} in corresponding area than in dimer row structure, which creates more space to be occupied by excess of DT. And this trimer row could be the other stable C_{70}/DT self-assembled structure when C_{70} interact with more DT. The differences of the DT and C_{70} coverage will be discussed in later chapter.

Overall, as the C_{70}/DT trimer row appears as a trapped structure, some of the trimer rows may formed during the growth of different C_{70}/DT dimer row domains. For example, when two dimer row islands expand towards each other, the final gap between the two islands may not be large enough for arrangement of a dimer row. According to our measurements in **Figure 4.3** (a), the distance between two normal repeating dimer rows is 19a. While when there is slightly less space in the middle of two domains, the C_{70} could then arrange with DT as a trimer row, which occupies less space, 15a. If the space even less than 15a, the C_{70} may not be able to form any other structure, and there would be a boundary between the two domains. However, we have not observed such a continuous process directly, and we will only consider it as one of the possibilities.

3.1.3 Thermal Stability

After scanning the sample for weeks, the C_{70}/DT dimer row structure is proved to be stable at RT. To find out the thermal stability of this structure, the sample is annealed at several temperatures ranging from 60 °C to 120 °C in steps of 10°C. The annealing lasts for 1 hour each time, and the

vacuum during annealing is kept to below 10^{-9} mbar. The STM images are collected after each annealing. **Table 4.1** shows the summary of the thermal annealing results. The disordered phase images in **Table 4.1** are taken within 24 hours after annealing, and the ordered phase images are taken after 72 hours after annealing. From the set of disordered phase images, we found that the coverage of C_{70} has no obvious changes after annealing, as the maximum annealing temperature is still far lower than the estimated desorption temperature of C_{70} on Au(111) substrate (~ 700 K). The C_{70}/DT ordered phase break into disordered phase and it requires some time for them to reform again.

The ordered phase images in **Table 4.1** are collected 72 hours after annealing, which show the structure when both C_{70} and DT molecules are stabilised. After the 60 °C/ 70 °C/ 80°C/ 90°C/ 100°C annealing, the final stable structure is always the C_{70}/DT dimer rows, and no other new self-assembled structures appearing. It is found that the C_{70} and DT are unable to form any ordered structure when the annealing temperature is above 110 °C, even if the sample is left at RT for over 72 hours. The reason for this change is likely to be the significant desorption of DT. The desorption temperature of DT from Au(111) surface is 120 °C[21], however, as the temperature we read is collected from the thermal couple on the STM manipulator instead directly collected from the sample surface, the actual temperature of sample would be slightly higher than the reading. When the annealing temperature is set as 110 °C, the temperature of sample surface is close to or already reach 120 °C, which makes DT desorb from the surface. With the desorption of DT, the DT remain on sample surface are unable to separate and hold the C_{70} locally, and the C_{70}/DT dimer row structure is not maintained due to the change in C_{70}-DT ratio. When all the DT desorb from the substrate, the C_{70} will gradually form close-packed phase on Au(111) surface. As the C_{70} molecules in image of disordered phase after 120 °C annealing have not form close-packed phase yet, there are still a small amount of DT remain within the disordered C_{70} domains.

Annealing Temperature	60 °C	70 °C	80 °C	90 °C
Ordered Phase	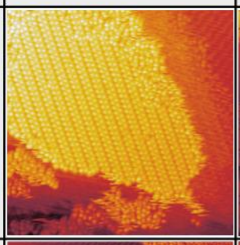	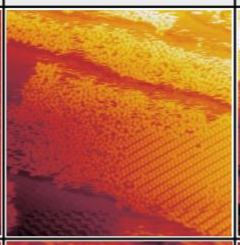	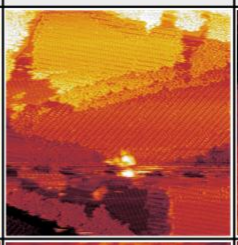	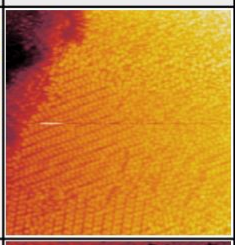
Disordered Phase	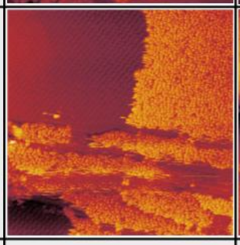	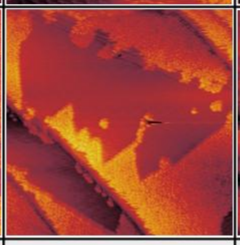	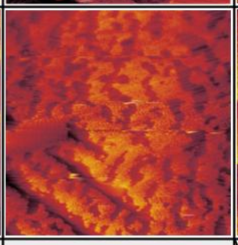	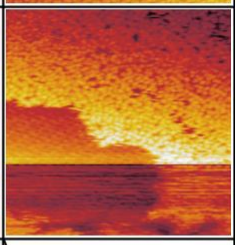
Annealing Temperature	100 °C	110 °C	120 °C	
Ordered Phase	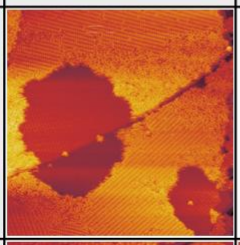	Not found	Not found	
Disordered Phase	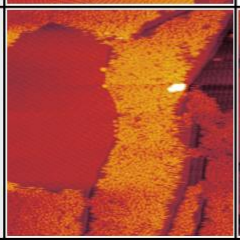	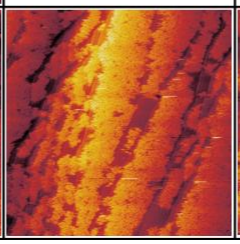	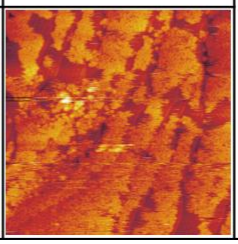	

Table 4.1 The summary of thermal annealing results. The disordered phase data shows the coverage change of C_{70}. The ordered phase data shows the phase difference when C_{70} and DT molecules are stabilised after annealing.

Overall, the C_{70}/DT dimer row structure is a rather stable structure for this system at RT. If both molecules have the right coverage on the Au(111) surface, they will adjust their local molecular ratio, forming a stable long-range ordered dimer row phase. Even if this dimer row phase is broken into disordered phase, as long as there is still a sufficient amount of C_{70} and DT molecules remaining on sample, they are always able to reform this dimer row structure.

3.2 C_{70}/Decanethiol Porous Framework Phase

3.2.1 Measurements and Details

The C_{70}/DT porous framework is found to form simultaneously with the C_{70}/DT dimer row structure on δ phase DT/Au(111) surface after the deposition of C_{70}. In comparation with the C_{70}/DT dimer row phase, the overall coverage of porous framework phase is lower. **Figure 4.7** (a) shows a domain of C_{70}/DT porous framework. The C_{70} dimers within the framework all keep the same orientation along $[11\bar{2}]$ direction, which is the same with the orientation of δ phase DT on Au(111) surface[19]. Similar with the C_{70}/DT dimer row phase, there is a sharp boundary between the porous framework and the δ phase DT. It suggests that the C_{70}/DT porous framework consumes all the DT molecules from δ phase, and even requires more DT as the coverage of porous framework phase is significantly less than dimer row phase. We also find several boundaries within the porous framework domains. The boundaries are deduced to form during the formation of this porous phase. And as the C_{70} dimers along the boundaries are still stable, the boundaries are likely to be filled with DT. The formation details of C_{70}/DT porous framework will be discussed later.

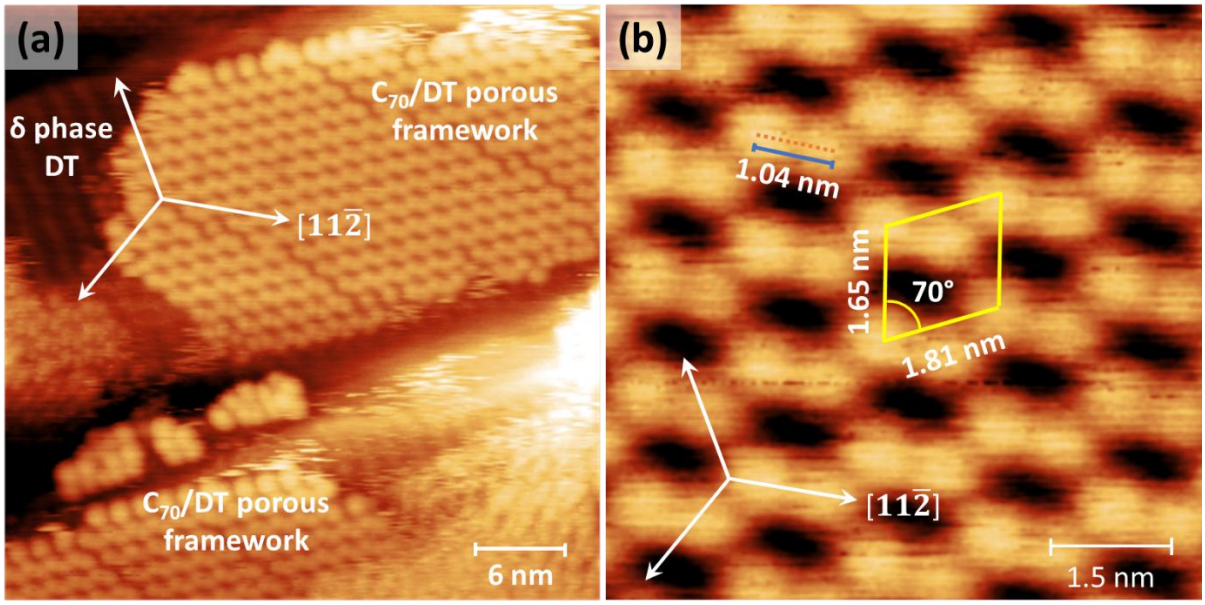

Figure 4.7 (a) The STM image showing the domains of C_{70}/DT porous framework phase, which are found to coexist with the δ phase DT. The C_{70} dimers within the porous framework all have the same orientation, which is along $[11\bar{2}]$ direction. There are two boundaries found inside the large porous framework domain, and it indicates that this large domain is formed with three small porous framework domains. (b) The measurements of C_{70}/DT porous framework structure.

The distance between two C_{70} within the dimer is 1.04 ± 0.02 nm. The parameters of porous framework structure unit cell marked in yellow are a = 1.65 ± 0.07 nm, b = 1.82 ± 0.04 nm, γ = 70.0 ± 0.4°.

The details of C_{70}/DT porous structure are shown in **Figure 4.7** (b). The distance between two C_{70} within the dimer is 1.04 ± 0.02 nm. It is close to the distance of another type of close-packed C_{70} on Au(111) surface, where the C_{70} form the close-packed phase with their long axis perpendicular to the Au(111) surface[15]. The unit cell for C_{70}/DT porous framework is marked in the yellow parallelogram, and the parameters are: a = 1.65 ± 0.07 nm, b = 1.82 ± 0.04 nm, γ = 70.0 ± 0.4°. The DT molecules fill the pores of framework, though they are still not observed at RT. It is possible that the DT occupy the equivalent sites inside each pore, as the pores of framework are all in the same size. Locally, the porous framework seems to be more ordered than the dimer row structure in C_{70}-DT system, as each C_{70} dimer interacts uniformly with the surrounding DT inside the pores. Whereas in the dimer row phase, it is possible that the interactions between C_{70} and DT on two sides of C_{70} dimers are not uniform, resulting in the neighbouring dimer rows having different orientations. The coverage of C_{70}/DT porous framework is expected to be higher than dimer row phase while the result is the opposite. The reason for that will be discussed later.

3.2.2 Formation of C_{70}/Decanethiol Porous Framework

Figure 4.8 shows the growth of a C_{70}/DT porous framework domain. As the expansion of this domain only happens at the boundaries, we mask the stable porous framework region in blue, and focus on the boundaries which are marked with red lines. There is a boundary within the domain, which is marked with a white dotted line, and the boundaries are thus divided into two parts, respectively region I and region II. In **Figure 4.8** (a), it is noticed that several single C_{70} arrange along the boundary in region I, which is similar with the formation of C_{70}/DT dimer row phase. Then in **Figure 4.8** (b) and (c), the single C_{70} keep moving from right to left side of region I, pairing with the pre-existing single C_{70} and forming C_{70} dimers along the boundary. In comparation with the single C_{70} row along the boundaries of C_{70}/DT dimer row phase in **Figure 4.5** (a), the single C_{70} in region I always maintain the same distance with the distance between C_{70} dimers within the porous framework, even they have not formed the dimers. It suggests that the coverage of DT around the porous framework phase is high enough to stabilise the C_{70}, and the binding sites of C_{70} and DT are more compatible with the Au(111) substrate.

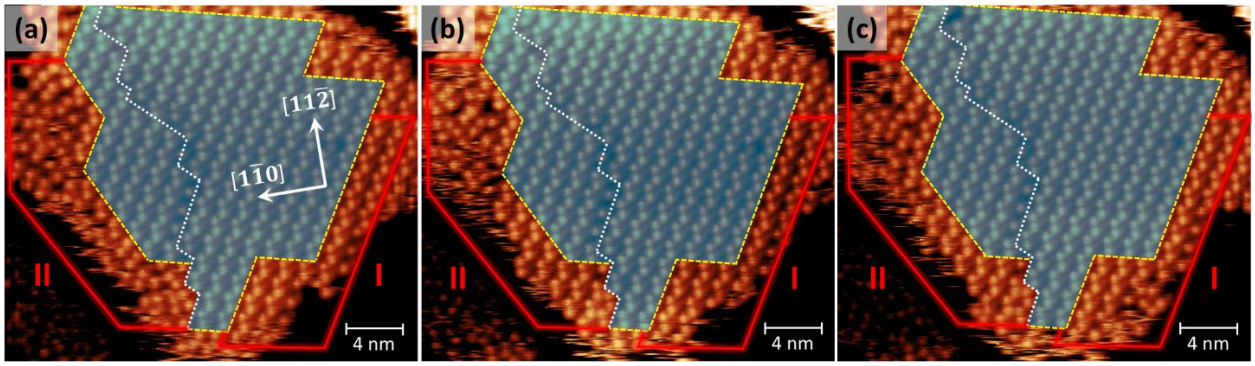

Figure 4.8 The formation of C_{70}/DT porous framework phase. The area in the middle masked in blue is the stable porous framework. The formation of porous structure happens at the boundaries of this domain, which are marked in red lines. There is a boundary within the domain, separating this domain into two parts. And the regions of boundaries on the two sides are respectively marked as region I and II.

With more C_{70} diffusing along the boundary, the porous framework in region I grows gradually. Then in region II, it is interesting to notice that there is one short C_{70}/DT dimer row initially in **Figure 4.8** (a). However, this dimer row soon decomposes into disordered C_{70} in (b). This is consistent with our previous reasoning that the single C_{70}/DT dimer row cannot exist on their own. The disordered C_{70} then reform and join the C_{70}/DT porous framework along the boundary.

According to the structure details and the formation of C_{70}/DT dimer row phase and porous framework phase, there are two possible explanations for the difference in coverage of these two structures. The first possible reason is that the stabilities of C_{70} are different. As we measured, the distance within the C_{70} dimers in dimer row phase is close to the distance between the lying down close-packed C_{70} molecules, while the distance within the C_{70} dimers in porous framework phase is close to the distance between the standing up close-packed C_{70} molecules. It suggests that the C_{70} have different molecular orientations in two phases. When C_{70} binding with the substrate with different orientation, their stabilities vary as it requires different energies to keep C_{70} in the particular orientations[9]. Therefore, if the C_{70} within the porous framework form the dimers in a less stable orientation, this porous framework phase would be not as easy to maintain as dimer row phase. Then this phase gradually breaks down and the C_{70} reform into dimer row phase at RT. The information of C_{70} molecular orientation from RT scanning data is limited, and that will be shown and discussed with the LT scanning data in next chapter.

The second possible reason is that the local coverages of DT in the regions of these two phases are different. Different coverage of molecules can greatly affect the final self-assembled structure, whether it is higher or lower[22]. It is more likely that C_{70}/DT porous framework phase starts to form in the regions where the coverage of DT is higher than the δ phase DT. With more DT molecules occupying the substrate of this region, there is less space for C_{70} to occupy. To fit in this region, the C_{70} bind with the Au(111) substrate with their long axis perpendicular to the surface so that horizontally the C_{70} occupy less space. And with more DT molecules contributing to this framework, the C_{70} within this domain or at the boundaries can be more effectively held by DT, that even the single C_{70} at the boundaries can be held at their binding sites, as shown in **Figure 4.8**. In contrast, the C_{70} at the boundaries of C_{70}/DT dimer row phase in **Figure 4.5** (a) diffuse more freely and will not be held at their binding sites. It is less possible that the C_{70}/DT porous framework phase forms in the region where the coverage of DT is lower than δ phase DT. If there is more space for C_{70} to occupy, they would lie down so that this space could be occupied more effectively, and it is hard to explain why C_{70} occupy the substrate with the standing up orientation. However, we cannot disprove this point based solely on the orientation and distance of C_{70} in porous framework phase at RT. It is helpful to discuss this with the thermal annealing data, as the coverage of DT becomes more uniform and gradually decreases during annealing, and the final C_{70}-DT self-assembled structure changes accordingly.

3.2.3 Thermal Stability

The thermal stability of C_{70}/DT porous framework phase is found to be much weaker than the C_{70}/DT dimer row phase. It is interesting to notice that all the C_{70}/DT porous framework phase disappear after annealing, even after the lowest 60 °C annealing. During the annealing, DT and C_{70} diffuse faster on the Au(111) surface, and all the molecules change into disordered phase. If the temperature of surface reaches 120 °C, DT would directly desorb from the Au(111) substrate[21], and the coverage of DT would decrease rapidly. When the temperature of surface is lower than 120 °C, DT will not directly desorb, but diffuse and occupy the surface more evenly. This can be further proved that the close-packed φ phase DT disappeared on the surface after annealing, which means the coverage of DT either becomes more even or reduces.

The C_{70}/DT porous framework phase disappear completely with the DT covering the Au(111) substrate more evenly, and do not reappear as the annealing temperature continue to rise until the

DT are desorbed form the Au(111) substrate. It indicates that the formation of C_{70}/DT porous framework phase requires the regions having higher local coverage of DT, which only exists on the DT/Au(111) sample prepared after initial annealing. Then with the deposition of C_{70}, more DT are pushed away, and the amount of DT on the sample decreases gradually. Irrespective of the temperature at which the C_{70}/DT/Au(111) sample is annealed, the regions of higher coverage of DT will not reappear.

According to these evidence and analysis, we deduced that there are more DT contribute to the formation of porous framework phase. And once the coverage of DT drops, this C_{70}/DT porous framework phase will disappear.

4. Conclusion

In this Chapter, the bicomponent self-assembly of C_{70}/DT system on Au(111) surface is studied. There are two self-assembled ordered phase observed from the surface, respectively the C_{70}/DT dimer row phase and C_{70}/DT porous framework phase. In some of the regions, the C_{70}/DT dimer row phase is found to transfer into the C_{70}/DT trimer row structure. The detail of C_{70}/DT dimer row structure, C_{70}/DT porous framework structure and C_{70}/DT trimer row structure at RT are revealed, including their structural parameters, formation and thermal stabilities.

The C_{70}/DT dimer row structure is the most common structure of this system observed on the sample surface. This structure is formed with two types of C_{70} dimer rows with the dimer axis keeping an angle of either 70° (clockwise) or 75° (counterclockwise) off the $[11\bar{2}]$ direction, respectively. And each two adjacent dimer rows have the same dimer axis. All the dimer rows observed grow in the direction parallel to the $[11\bar{2}]$ direction or the other two equivalent directions. This dime row structure can be broken through thermal annealing, and will reform when the sample temperature drop to RT.

The C_{70}/DT porous framework structure is the structure observed after the deposition of C_{70}. The porous framework structure is formed with the C_{70} dimers having their dimer axes in the direction parallel to the $[11\bar{2}]$ direction. The arrangement of C_{70} within this structure is more regular than the C_{70} in dimer row phase, while this porous framework phase does not reform after the thermal annealing. Thus, this porous framework structure is deduced to form in the regions where the local

coverage of DT is higher. Once the local coverage of DT drops, the C_{70}/DT porous framework phase will disappear.

References

[1] Gooding, J. J.; Ciampi, S. The Molecular Level Modification of Surfaces: From Self-Assembled Monolayers to Complex Molecular Assemblies. *Chem. Soc. Rev.* **2011**, *40*, 2704.

[2] Zhang, X.; Fan, X.; Zhu, G.; Wang, Y.; Ding, H.; Lin, H.; Li, Y.; Li, Q.; Gao, J.; Pan, M.; Guo, Q. Two-Dimensional van Der Waals Supramolecular Frameworks from Co-Hosted Molecular Assembly and C60 Dimerization. *J. Phys. Chem. C* **2020**, *124*, 12589–12595.

[3] Zeng, C.; Wang, B.; Li, B.; Wang, H.; Hou, J. G. Self-Assembly of One-Dimensional Molecular and Atomic Chains Using Striped Alkanethiol Structures as Templates. *Appl. Phys. Lett.* **2001**, *79*, 1685–1687.

[4] Li, F.; Tang, L.; Zhou, W.; Guo, Q. Formation of Confined c60Islands within Octanethiol Self-Assembled Monolayers on Au(111). *J. Phys. Chem. C* **2009,** *113*, 17899–17903.

[5] Ding, H.; Zhang, X.; Li, B.; Wang, Y.; Xia, C.; Zhao, H.; Yang, H.; Gao, Y.; Chen, X.; Gao, J.; Pan, M.; Guo, Q. Orientational Growth of Flexible van Der Waals Supramolecular Networks. *Small Struct.* **2023**, *5*, 2300230.

[6] Olmstead, M. M.; Costa, D. G.; Maitra, K.; Noll, B. C.; Phillips, S. A.; Van, P. M.; Balch, A. L. Interaction of Curved and Flat Molecular Surfaces. The Structures of Crystalline Compounds Composed of Fullerene (c_{60}, $c_{60}O$, c_{70}, and $c_{120}O$) and Metal Octaethylporphyrin Units. *J. Am. Chem. Soc.* **1999**, *121*, 7090–7097.

[7] Hedberg, K.; Hedberg, L.; Bühl, M.; Bethune, D. S.; Brown, C. A.; Johnson, R. D. Molecular Structure of Free Molecules of the Fullerene c70 from Gas-Phase Electron Diffraction. *J. Am. Chem. Soc*. **1997**, *119*, 5314–5320.

[8] Liu, S.; Lü, Y.; Kappes, M. M.; Ibers, J. A. The Structure of the C60 Molecule: X-Ray Crystal Structure Determination of a Twin at 110 K. *Science* **1991**, *254*, 408–410.

[9] Niu, G.; Geng, J.; Wang, X.; Yang, X.; Xiong, W.; Zhang, H.; Ruan, Z.; Zhang, Y.; Gao, L.; Lu, J.; Cai, J. Adsorption Configurations and Electronic Properties of Self-Assembled C_{60} and C_{70} Molecules on a Semiconductor CuSe Monolayer with Periodic Nanopores. *Nanotechnology* **2023**, *34*, 395602–395602.

[10] Dubois, L. H.; Zegarski, B. R.; Nuzzo, R. G. Molecular Ordering of Organosulfur Compounds on Au(111) and Au(100): Adsorption from Solution and in Ultrahigh Vacuum. *J. Chem. Phys.* **1993**, *98*, 678–688.

[11] Poirier, G. E. Coverage-Dependent Phases and Phase Stability of Decanethiol on Au(111). *Langmuir* **1999**, *15*, 1167–1175.

[12] Bumm, L. A.; Arnold, J. J.; Dunbar, T. D.; Allara, D. L.; Weiss, P. S. Electron Transfer through Organic Molecules. *The journal of physical chemistry. B* **1999**, *103*, 8122–8127.

[13] Balzer, F.; Gerlach, R.; Polanski, G.; Horst-Günter Rubahn. Chain Length Dependence of the Structure of Alkane Thiol Films on Au(111). *Chem. Phys. Lett.* **1997**, *274*, 145–151.

[14] Rai, A.; Singh, V. K.; Nayak, J.; Roy Barman, S. Parameter Dependent Fabrication of Chromium Nano-Structures on Au(111) Surface. *Surf. Sci.* **2019**, *679*, 169–173.

[15] Katsonis, N.; Marchenko, A.; Fichou, D. Adsorption and Self-Assembly of C70 Molecules at the Au(111)/N-Tetradecane Interface: A Scanning Tunneling Microscopy Study. *Adv. Mater.* **2004**, 16, 309–312.

[16] Shamloo, A.; Bakhtiari, M. A.; Tohidloo, M.; Seifi, S. Investigation of Fullerene Motion on Thermally Activated Gold Substrates with Different Shapes. *Sci. Rep.* **2022**, *12*, 14397.

[17] Kaya, D.; Wang, Y.; Mustafa Akyol; Faruk Karadag; Ahmet Ekicibil; Guo, Q. Self-Defined Transition State in Hybrid C70–Au Clusters Created by the Scanning Tunneling Microscope Tip. *J. Phys. Chem. C* **2019**, *123*, 27945–27950.

[18] Guo, Q.; Li, F. Self-Assembled Alkanethiol Monolayers on Gold Surfaces: Resolving the Complex Structure at the Interface by STM. *Phys. Chem. Chem. Phys.* **2014**, *16*, 19074.

[19] Maksymovych, P.; Oleksandr Voznyy; Dougherty, D. B.; Sorescu, D. C.; Yates, J. R. Gold Adatom as a Key Structural Component in Self-Assembled Monolayers of Organosulfur Molecules on Au(111). *Prog. Surf. Sci.* **2010**, *85*, 206–240.

[20] Suresh, R.; Venkataraman, N.; Vasudevan, S.; Ramanathan, K. V. Conformational Mobility in Alkyl-Chains of an Anchored Bilayer. *J. Phys. Chem. C* **2006**, *111*, 495–500.

[21] Sotthewes, K.; Kap, Ö.; Wu, H.; Thompson, D.; Jurriaan Huskens; Harold. Ordering of Air-Oxidized Decanethiols on Au(111). *J. Phys. Chem. C* **2018**, *122*, 8430–8436.

[22] Sridhar, D. B.; Gupta, R.; Rai, B. Effect of Surface Coverage and Chemistry on Self-Assembly of Monolayer Protected Gold Nanoparticles: A Molecular Dynamics Simulation Study. *Phys. Chem. Chem. Phys.* **2018**, *20*, 25883–25891.

V. C_{70}/Decanethiol Self-Assembled Structures at 77K

1. Introduction

In the previous chapter, we discussed the structure of the C_{70}/DT mixture formed at RT on Au(111). The positions of C_{70} molecules and the intermolecular distances between C_{70} molecules were measured with RT scanning data. However, the molecular orientations of C_{70} can only be roughly estimated from RT data. Apart from that, due to the mobility of the alkane chains at RT, no clear signals from the DT can be found in the STM images. This significantly affected our ability to establish a reliable structural model.

When the sample is cooled down to LN_2 temperature (~ 77 K) or LHe temperature (~ 5 K), the diffusion of C_{70} and DT on Au(111) surface stops, the molecules are all frozen in their places while they can still be moved by tip during scanning[1]. The flipping of DT alkane chains and the rotation of C_{70} at low temperatures are restricted as well[2]. Thus, the intramolecular structure of C_{70}, as well as the locations of the DT molecules, can be resolved with STM. The extra information acquired at low temperatures is valuable for refining our structural model by reducing the number of unknown parameters. Though there are still some uncertainties about DT as the signals we captured are from the terminal group of alkane chains[3], we can come up with more realistic models that are closer to the actual physical structure.

The work in this chapter focus on the molecular orientation of C_{70} and the location of DT inside the unit cell. Structural models proposed in the last chapter have been refined based on the low temperature STM data. Several structural models are proposed in this chapter, and the advantages and disadvantages of these models will be discussed.

2. Result and Discussion

A new C_{70}/DT/Au(111) sample is prepared for LT scanning. The preparation of the δ phase DT/Au(111) sample is the same as described in the last chapter. While as the amount of C_{70} on the first sample is more than we expected, we deposited fewer C_{70} molecules this time by reducing the

temperature of the evaporation source. The C_{70} is deposited on the sample at 370 °C for 4 minutes, and the C_{70}/DT/Au(111) sample is left at RT for over 72 hours before it is cooled down. The sample is then cooled down with LN_2 to 77 K, and it takes about 5 hours for the temperatures of both sample and tip to stabilise. The LN_2 is regularly filled into the cryostat of LT-STM, and the temperature of C_{70}/DT/Au(111) sample fluctuates from 77 K to 79 K during the whole LT experiment.

2.1 C_{70} Molecular Orientations

2.1.1 C_{70} Molecular Orientations in the C_{70}/Decanethiol Dimer Row Phase

Figure 5.1 shows the C_{70}/DT dimer row phase at 77 K, and it seems that cooling down from RT to 77 K causes no change to the overall geometric structure of the dimer row phase. The C_{70}/DT dimer row phase coexists with close-packed φ phase DT in this area, which is similar to the first sample before annealing. The main difference between RT scanning data and the LT scanning data below is that there are more structural details shown within the C_{70}. The C_{70} molecules shown in RT data look like spherical particles, as the thermal energy keeps the C_{70} molecules rotating. The scanning speed of the STM is much slower than the speed of molecular rotation. Thus, the STM image shows a time averaged signal lacking information on molecular orientation. A single frame of an STM image can take as long as 15 minutes to collect. When the sample is cooled down, the rotations of C_{70} gradually stop, and the C_{70} within the dimers adjust their orientations so that they can finally freeze in a specific more stable orientation which can be observed with the STM.

In the STM images shown in **Figure 5.1**, each molecule exhibits some internal structure. The most common feature is two or three parallel bars. The observation of intramolecular structure is a piece of evidence that the molecule at 77 K has a fixed orientation. These bright bars could be associated with tunnelling of electrons into the pentagonal faces of fullerene which are known to be electron deficient (each pentagonal face is consisting of five C-C single bonds)[4]. When scanning with a '+' bias voltage, the electrons tunnel from the STM tip to the sample surface, and they prefer to choose the path where the unsaturated C-C single bond is located. Thus with different faces of fullerene facing up, we can observe different features[5].

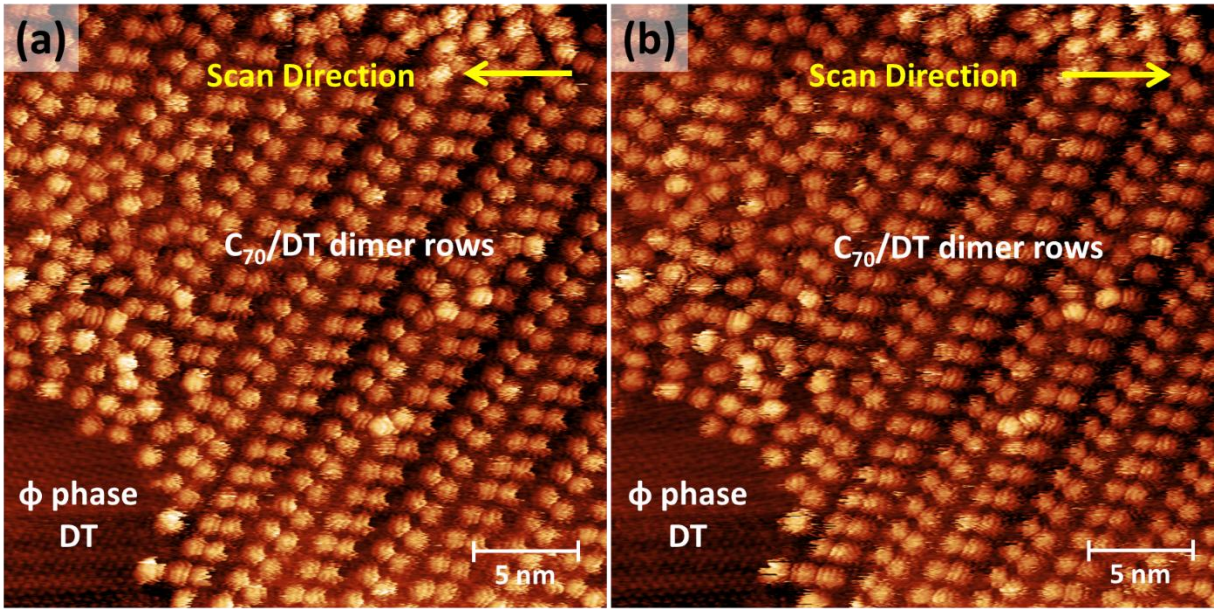

Figure 5.1 The LT scanning data of C_{70}/DT/Au(111) sample, and the scanning parameters are: I = 40 pA, V_{bias} = 400 mV. C_{70}/DT dimer row phase is found coexist with the φ phase DT, which is the feature of C_{70}/DT/Au(111) sample without annealing. In this area, (a) is the image collected during backward (leftward) scanning, and (b) is collected during forward (rightward) scanning.

Figure 5.1 (a) and (b) show respectively the backward (tip moving from right to left) and forward (tip moving from left to right) scanning data in a single scan. The resolution of molecular orientations seems to be affected during scanning in both directions, leading to rather noisy signals. Comparing the details in **Figure 5.1** (a) and (b), it is found that on the right side of C_{70}/DT dimer rows in (a), the signals of C_{70} seems to be covered by some regularly located spot-like signals, and the similar feature also happens on the left side of dimer rows in (b). It is noticed that the positions of these features are related to the scan direction of the sample. According to the scan directions in (a) (backward) and (b) (forward), this covering of the C_{70} signal could be caused by the wobbling of the alkane chains, that the alkane chains can be attracted by tip through the tip-surface interaction when the tip get closer to the sample surface during scanning. This observation suggests the existence of DT in between the C_{70} dimer rows. Overall, the C_{70} molecules within the C_{70}/DT dimer row phase keep the same orientation.

We then collect the data showing the C_{70} molecular orientation with higher resolution, as shown in **Figure 5.2** (a). It is clearly found that there are three bright bars shown in one C_{70}, which means three pentagonal faces of C_{70} are facing up in this orientation. We then compare this feature with published results, and this orientation looks similar with the C_{70} lying flat with their long axis parallel to the substrate[5]. However, there is still difference between the two results, that the three bright bars of completely flat lying C_{70} are evenly spaced and parallel to each other, while the bright bars we observed from the C_{70} dimers seems to have a tiny shift towards one side. And in **Figure 5.2** (a), the three bright bars shift towards top right direction.

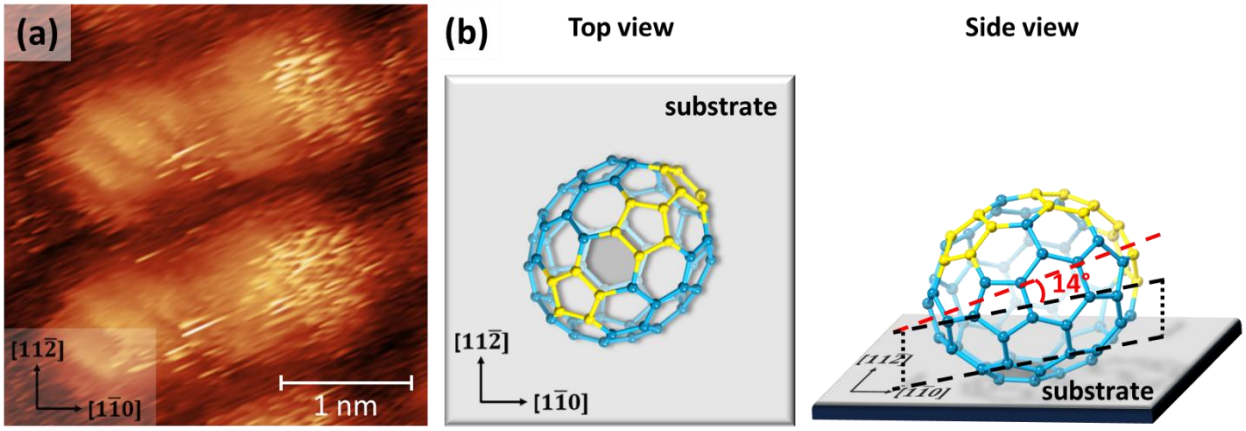

Figure 5.2 (a) Molecular orientation of C_{70} within the dimer row phase. The three bright bars inside the C_{70} correspond to three pentagonal faces of C_{70} which are electron deficient. Scanning parameters: V_{bias} = 400 mV, I = 50 pA. (b) The illustration of C_{70} binding on the substrate, and the model is shown in both top view and side view. The three yellow pentagonal faces correspond to three bright bars in (a), and the C_{70} lies down with a hexagonal face (filled in dark grey) in contact with gold substrate. The binding directions of C_{70} in different dimer rows and porous framework vary, and the binding direction shown in (b) corresponds to the C_{70} in (a).

With the assistance of a ball-and-stick model that we constructed, we come up with a relatively reasonable binding scheme, as shown in **Figure 5.2** (b). The C_{70} molecule in this binding scheme is lying down with a hexagonal face in contact with the Au(111) substrate, but its long axis makes 14° angle off the substrate plane. The hexagonal face of C_{70} in contact with substrate is shaded in dark grey, and the three pentagonal faces marked in yellow corresponds to the three bright bars in **Figure 5.2** (a), which are the electron deficient parts. When C_{70} binds with the substrate in this

way, the three bright pentagonal faces will shift towards one side, and we can also identify the binding direction of C_{70} on the Au(111) substrate according to this shifted direction.

2.1.2 C_{70} Molecular Orientations in the C_{70}/decanethiol Porous Framework Phase

An LT scanning image for the C_{70}/DT porous framework phase is shown in **Figure 5.3** (a). In this area, the porous framework phase is found to coexist with the C_{70}/DT dimer row phase. By directly comparing the two phases, we find that the C_{70} dimer axis within the porous framework is parallel to the $[11\bar{2}]$ direction. Similar with the C_{70}/DT dimer row phase, there is no change to the geometric structure during the cooling process, and the intramolecular details of several C_{70} molecules are revealed. However, the signals from porous framework are found to be more flickering and the resolution of C_{70} within the porous framework phase is lower than that for the dimer row phase. Fortunately, we can still distinguish the orientations for C_{70} molecules.

Similar with the features shown in the C_{70} within the dimer rows, several bright parallel bars are found inside the C_{70}, which means that these C_{70} are also lying down on the Au(111) substrate. What different is that these bar-like features from C_{70} within the porous framework phase look more even having no specific shift towards any side. It indicates that those C_{70} molecules are likely to be lying flat with their long axis parallel to the Au(111) substrate[5]. To show the details of C_{70} molecular orientation more clearly, we select the area marked in the yellow dashed frame, and the zoomed-in image is shown in **Figure 5.3** (b).

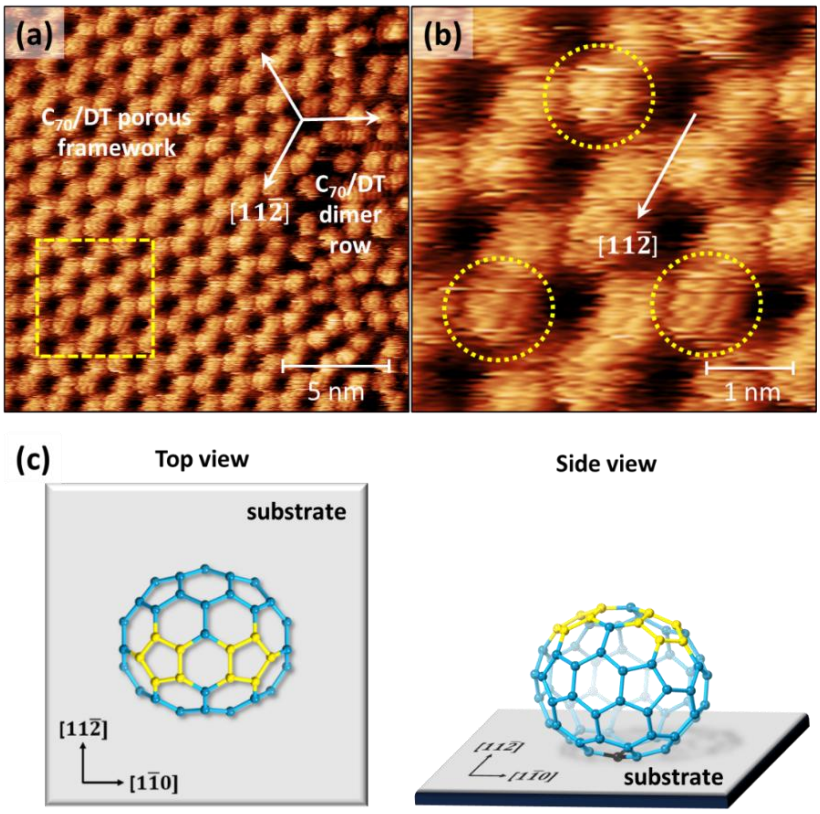

Figure 5.3 (a) The LT data showing the coexistence of C_{70}/DT porous framework phase and C_{70}/DT dimer row phase, and the orientation of C_{70} dimer within the porous framework is parallel to the [11$\bar{2}$] direction. The scanning parameters for this image are: I = 50 pA, V_{bias} = 700 mV. (b) The zoom in of the area marked in yellow dashed frame in (a), which shows the details of C_{70} molecular orientation within the porous framework phase. The parallel bright bars inside the C_{70} are contributed by the pentagonal rings of C_{70}. These features can only be observed from one of C_{70} within the C_{70} dimers. (c) The illustration of C_{70} binding on the substrate in porous framework phase, and the model is shown in both top view and side view. The pentagonal rings marked in yellow correspond to the parallel bright bars in (a) and (b). The C_{70} flatly lies down with a carbon atom (filled in dark grey) in contact with the substrate, and its short axis and long axis parallel to the [11$\bar{2}$] direction and the [1$\bar{1}$0] direction respectively.

The circled C_{70} molecules in **Figure 5.3** (b) are found to have similar features. After careful comparison, the feature of the circled C_{70} is close to the feature of C_{70} lying flat on the substrate with a carbon atom facing up[5]. Only one of the molecules in each dimer shows internal structure. The other molecule in the dimer does not show resolved features. For different dimers, it is always

the molecule on the same side of the dimer exhibits internal structures. This suggests that molecules showing the same internal structure have the same orientation. To ensure that these intramolecular features are not affected by the scanning conditions, we then scanned this area in different scanning parameters (tunnelling current, bias voltage, scanning directions, etc), and the features we observed are still the same as shown in **Figure 5.3** (a). It is possible that those regularly arranged C_{70} with no clear molecular orientation observed are less stable as they could be pushed away from their preferred binding sites. As we discussed before, the local coverage of DT within the porous framework phase is likely to be higher than the DT coverage in dimer row phase. If so, the DT within the pores could over press the neighbouring C_{70} and lead to the shift of C_{70}. However, as there is no direct observation of the DT within the pores, we can only analyse it with the theoretical models, and this will be further discussed in the later section.

In **Figure 5.3** (c), we show the illustration for this type of C_{70} molecular orientation. The C_{70} bind on the surface with a carbon atom in contact with the Au(111) substrate. The yellow pentagonal rings contribute to the parallel bright bars in **Figure 5.3** (a) and (b). The molecular direction of this C_{70} is more ordered than the C_{70} in dimer row phase, which has its short axis parallel to the $[11\bar{2}]$ direction, and long axis parallel to the $[1\bar{1}0]$ direction.

2.2 Direct Observation of Decanethiol within the C_{70}/Decanethiol Dimer Row Phase

In addition to the binding type of C_{70}, the binding details of DT on Au(111) substrate is also necessary for modelling C_{70}/DT ordered phases. However, due to the relatively low tunnelling conductivity of alkanethiol on the gold surface[6], it is still a challenge to find the details of DT even if they are stabilised at 77 K. We then choose several areas containing stable C_{70}/DT dimer row phase, scanning each area with different tunnelling currents and bias voltages, and the details are shown in **Figure 5.4**.

Firstly, we try to use the same tunnelling current and different bias voltages during scanning. As shown in **Figure 5.4** (a), there is a significant difference when the bias voltage is changed from 500 mV to 100 mV, that some regular arranged spots are becoming visible in between the dimer row gaps along the $[11\bar{2}]$ direction, and these features appear to have a repeating distance which is the same as that of C_{70} molecules along the $[11\bar{2}]$ direction. As there are only C_{70} and DT

involved in this system, these extra features are likely to be contributed by DT molecules. For the overall structure, there is no geometric changing of C_{70}/DT dimer row phase when the bias voltage is changed. And then when the bias voltage is changed back to 500 mV, these features become invisible again, which indicates that the change of this feature is reversible and related to bias voltage. The bias voltage affects which electronic states contribute to the tunnelling current during scanning, so changing it can highlight different features of the surface electronic structure[7,8]. Meanwhile, the change of bias voltage will also affect the tip-surface distance, leading to different tip-surface interactions. With the effect of this interaction, the scanning tip mechanically brushes the flexile parts of molecules (such as the alkane chains of DT), causing temporary changes of the features during scanning.

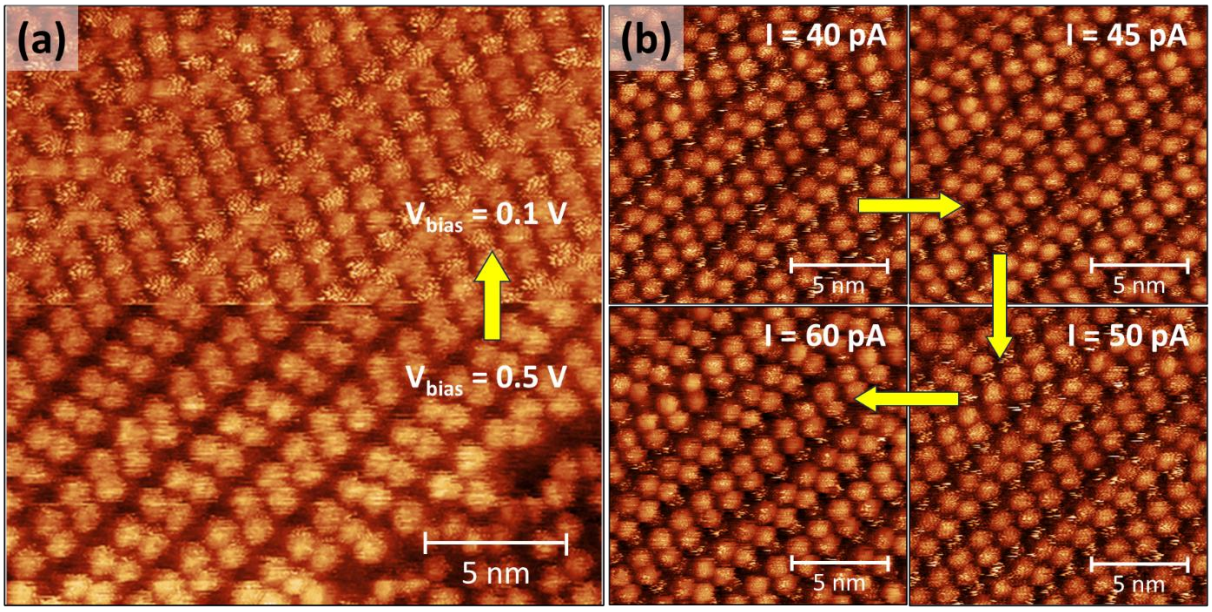

Figure 5.4 (a) The scanning of C_{70}/DT dimer row phase with bias voltage change from 500 mV to 100 mV, and tunnelling current is maintained at 40 pA. Some extra features in the gaps between C_{70} dimer rows become obvious at 100 mV, which are probably contributed by DT molecules. (b) The scanning of C_{70}/DT dimer row phase with tunnelling current change from 40 pA to 60 pA, and the bias voltage is maintained at 400 mV. Some similar features are found in between the C_{70} dimer rows, while there is no obvious difference when the tunnelling current changes.

To gather more details of this feature, we then decide to find out how it performs when scanned with different tunnelling currents. However, different from the change of bias voltage, the tip-

surface distance decreases significantly with the rising of tunnelling current, which leads to excessively strong tip-surface interactions and makes the C_{70}/DT self-assembled structure more likely to be disrupted by tip during scanning. On the other hand, if the tip is too far away from the sample surface when the tunnelling current is set lower, some details of the sample such as molecular orientations of C_{70} would not be captured. Therefore, we can only change the tunnelling current in a rather limited range, from 30 pA to 60 pA. The results of current-changing scanning are shown in **Figure 5.4** (b). This time we keep the bias voltage at 400 mV and scan the sample with different tunnelling current of, respectively 40 pA, 45 pA, 50 pA, and 60 pA. It is found that the similar regular arranged spots shown in between the dimer row gaps, and the repeating distance of these spots along $[11\bar{2}]$ direction is the same as that observed in **Figure 5.4** (a). However, these features of DT do not seem to change obviously when the tunnelling current is risen from 40 pA to 60 pA. When we change the tunnelling current from 40 pA to 60 pA, to estimate with a tungsten tip scanning a DT monolayer on Au(111) surface, the tip-surface distance reduces by approximately 0.3 ~ 0.4 Å, which may not be sufficient to cause a significant change in the tip-surface interactions. Though there is no obvious change found in **Figure 5.4** (b), we notice that these features have tendency to wobble in between the dimer row gaps, which matches with the behaviour of DT as we expected. And we can deduce that the appearance of these features in both **Figure 5.4** (a) and (b) is related to DT in the C_{70}/DT dimer row phase.

However, because of the rapid flickering of the signal in **Figure 5.4**, it is not certain if each rounded feature is from a single DT chain or more. We then change the parameters of scanning (tunnelling current, bias voltage, loop gain, time constant), trying to find out exactly what are contained in these features. **Figure 5.5** (a) is the C_{70}/DT dimer row phase scanned at: I = 50 pA, V_{bias} = 200 mV, and the features in between the dimer rows are similar with those in **Figure 5.4**. Then when we scan the sample with: I = 50 pA, V_{bias} = 800 mV, more details of these features are revealed, as shown in **Figure 5.5** (b). In the circled region II, several small spots become visible in one of the gaps. These spots come in groups of three or four, and the repeating distance of these groups is the same with distance between C_{70} dimers along $[11\bar{2}]$ direction. When we scan this area in **Figure 5.5** (b) with a higher bias voltage, the tunnelling current is mainly contributed by the C_{70} lowest unoccupied molecular orbital (LUMO)[9], which makes C_{70} appears much taller than DT. Meanwhile, as the tip is also relatively far away from the surface, these DT in between the C_{70} dimer row gaps are supposed to be invisible as shown in the bottom half of **Figure 5.4** (a). Based

on our previous experience, we speculate that one or more molecules (C_{70} or DT) may have adsorbed onto the very front of the tip during scanning, which enhances the tip (e.g. CO enhanced tip), and the resolution of the localised area is then improved. When we further check the data, we found that it is hard to observe clear bright spots in the image scanned in the opposite direction, which partially confirms our speculation. However, the molecules absorbed on tip are not stable enough at 77 K, and their positions are likely to change during the scanning, making the resolution of the image unstable as shown in **Figure 5.5** (b).

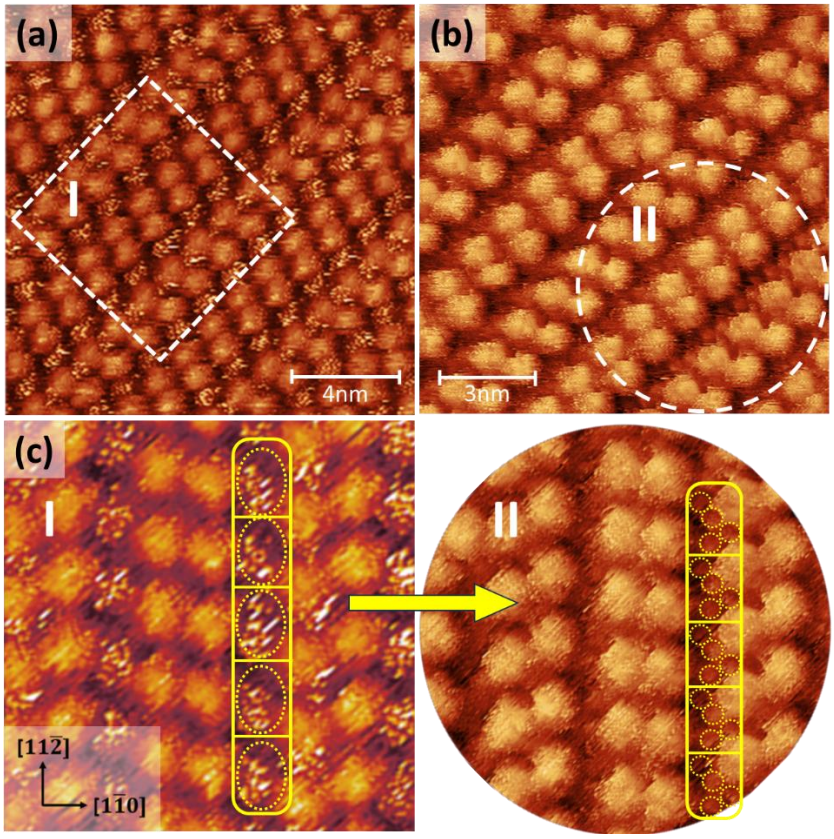

Figure 5.5 (a) Image acquired at: I = 50 pA, V_{bias} = 200 mV. The flickering signal in between the C_{70} dimers arises from the contribution of the DT molecules. (b) Image acquired at: I = 50 pA, V_{bias} = 800 mV. Individually resolved DT chains at some locations. These features remain when the bias voltage is changed to 700 mV and 600 mV. (c) Magnified views of the marked square area I in (a) and the circular area II in (b).

To compare these features more clearly, we choose two corresponding regions from **Figure 5.5** (a) and (b), and the related details are shown in **Figure 5.5** (c). The gaps marked in yellow frame

represent the corresponding positions in regions I and II. In region I, the signal from DT alkane chains looks flickering and mixing into larger round spots. In region II, the signal from DT alkane chains looks more stable and discrete, and each four small spots correspond to one larger spot in region I. From the signals in region II, we can deduce that these discrete DT alkane chains are oriented nearly perpendicular to the Au(111) substrate so that they can be observed simultaneously with C_{70}. If a DT molecule is tilted significantly from the surface normal, it may not be observed in STM. We also notice that these observed DT chains are closer to right side of the dimer rows, rather than in the middle. Though there is nothing observed on the other side, it is likely that there are some tilted DT molecules, otherwise the dimer rows on the left side could not be stabilised without the supporting of DT chains. According to what we observed that these discrete signals of DT chains can only be viewed in the forward (rightward) scanning, the possible explanation is that the available site positions for RS-Au-SR staple (with Au adatom occupying the bridge site of Au(111) substrate)[10] in those gaps are closer to the left side of 70°- tilted C_{70} dimer rows. When tip scanned forward, due to the obstruction of C_{70} on the right, the alkane chains are held standing up. And when tip scanned backward, there is larger space for DT chains to lie down, which makes the signals of DT blurry. We will discuss about different possible site positions of DT later with more straightforward models of C_{70}/DT dimer row phase.

Overall, the direct observation of DT alkane chains provides us more useful details of DT in C_{70}/DT dimer row phase. Though there are still some uncertainties, it gives us guidance for model building and improves the reliability of the models.

2.3 Models for C_{70}/Decanethiol Dimer Row Structure

With the relatively sufficient details of both C_{70} and DT within the C_{70}/DT dimer row phase, we tried to build up possible structural models for this structure. First, we draw a diagram representing the close-packed Au(111) surface. We then place C_{70} molecules onto Au(111) using all the measured parameters shown in **Figure 5.6** (a). In this model, the grey circles represent closed-packed Au atoms on Au(111). The C_{70} molecules are shown with wire-frame ovals. The size of C_{70} has been calibrated with the Au(111) unit cell constant (a = 0.288 nm)[11] so that all drawings here are to scale. The orientation of C_{70}, as we mentioned in **Figure 5.2**, is lying down with a hexagonal face in contact with Au(111) substrate. Here, in **Figure 5.6** (a), we also considered about the

different binding directions of C_{70} within the dimer rows in two directions, and that has been reflected in the model. We moved the four dimer rows around by translation and tried to find the bonding site. We expect C_{70} to sit on a high symmetry site. Moreover, the structure should be commensurate with the Au(111) substrate and show the correct periods. However, we found that it is hard to match this arrangement of C_{70} with the binding sites of Au(111) substrate properly. If the C_{70} in dimer row 1 occupy the three-fold (left) / bridge (right) sites of substrate, then the C_{70} in repeating dimer row 3 would occupy the bridge (left) / three-fold (right) sites of substrate, which is inequivalent. And in dimer row 4, the C_{70} have to occupy the top sites of Au(111) substrate. Though it is possible for C_{70} occupying the substrate in this way, it seems not stable enough for a highly ordered structure.

In the previous chapter, we mentioned that the unit cell we measured for C_{70}/DT dimer row phase is close to, but not a rectangular cell. However, even if we minimise the measurement errors by taking a large number of measurements, it is inevitable that there will still be errors during the scanning process, such as the uncertainty in X/Y movement of the STM scanning head, the thermal drift of the tip and the sample. Since the errors always exist, we then considered modifying the unit cell for C_{70}/DT dimer row phase into a rectangular cell, and the corresponding model is shown in **Figure 5.6** (b). The unit cell parameters for this rectangular cell are: a = 5.47 nm, b = 1.48 nm, γ = 90.0°. The C_{70} in this model have the identical molecular orientations with the C_{70} shown in **Figure 5.6** (a), and the only difference is the site position of C_{70} on Au(111) substrate. With a rectangular unit cell, the C_{70} in two repeating dimer rows 1 and 3 are available to occupy exactly the same binding sites of Au(111) substrate, as the distance between each two repeating dimer rows is an integral number of the Au(111) unit cell constant (19a). For dimer rows 2 and 4 in **Figure 5.6** (b), the C_{70} in these dimer rows can also occupy the three-fold hollow site, which is the same binding site with C_{70} in dimer row 1 and 3. It is interesting to notice that the diagonal direction of this rectangular unit cell is the same with the direction of C_{70} dimer axis in the row 2, that $b/a = 19/3\sqrt{3} \approx \tan 75°$. And there could be some relationship between these two angles. However, we are unable to find more correlations or probable evidence from the models in **Figure 5.6**, and this will be discussed later with the adding of DT to this model.

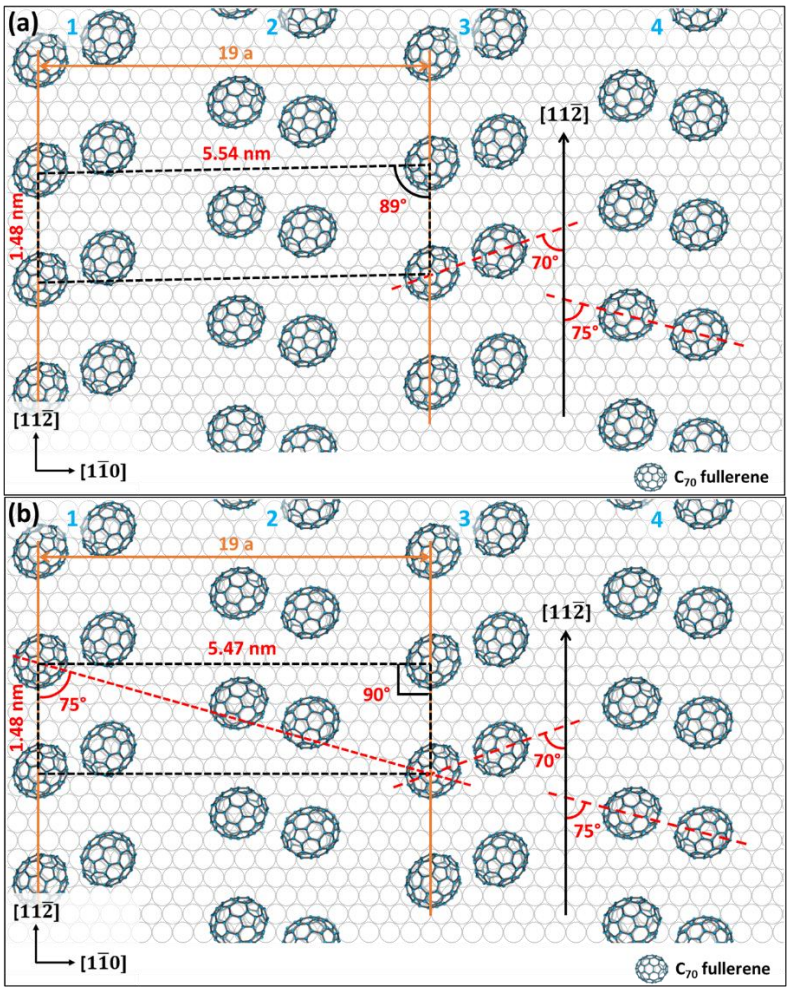

Figure 5.6 (a) The model of C_{70} within the C_{70}/DT dimer row phase on the Au(111) substrate. The unit cell parameters in this model are: a = 5.54 ± 0.02 nm, b = 1.48 ± 0.02 nm, γ = 89.2 ± 0.6°. The distance between each two repeating dimer rows, such as row 1 and row 3, is 19a. The C_{70} within different dimer rows occupy the different binding sites of Au(111) substrate. (b) The revised model for C_{70}/DT dimer row phase. The unit cell parameters for this rectangular cell are: a = 5.47 nm, b = 1.48 nm, γ = 90.0°. The C_{70} within each dimer row occupy the three-fold hollow sites of Au(111) substrate, which shows a higher symmetry.

Comparing these two models in **Figure 5.6** (a) and (b), the arrangement of C_{70} in (b) is obviously more regular, which makes the whole structure having a higher symmetry. In this arrangement, as the C_{70} from two repeating dimer rows with the same dimer axis occupy the same binding sites, the repeating distance is then 19a. While in the arrangement of C_{70} in (a), the repeating distance has to be 38a, so that the C_{70} from two repeating dimer rows with same dimer axis would occupy

the same binding sites of Au(111) substrate. If we only consider the arrangement of C_{70} on Au(111) substrate, the model in **Figure 5.6** (b) would be more reasonable. However, C_{70} would not form this structure spontaneously, and we have to consider the interactions between C_{70} and DT. The arrangement of DT on Au(111) surface also plays an essential role in the formation of C_{70}/DT dimer row phase. Therefore, the arrangement of C_{70} still need to be determined by considering how DT molecules fit into the structure.

The DT molecules, different from C_{70} molecules, have specific binding sites on the Au(111) substrate. As we mentioned earlier, the DT molecules bind to the substrate in the form of RS-Au-SR staples, and the Au adatoms occupy the bridge sites of Au(111)[10]. Though we are unable to directly observe the RS-Au-SR staples from our data, we can still derive the approximate number of RS-Au-SR staples within each unit cell based on the coverage of δ phase DT and the available binding sites among C_{70} dimers. The coverage of δ phase DT on Au(111) substrate is 0.23 ML before adding C_{70}. Then with the adsorption of C_{70}, some of the available binding sites of DT are occupied by C_{70}, and the DT coverage within the unit cell of C_{70}/DT dimer row phase is likely to be lower than that of δ phase DT. In additional, the local DT coverage cannot be higher than that of close-packed φ phase DT, which is 0.33 ML on Au(111) substrate. On the other hand, the DT coverage cannot be too low either, otherwise the C_{70} molecules cannot be effectively separated and the C_{70}/DT dimer row phase will be less stable.

According to this information mentioned above, we came up with several possible models by incorporating DT molecules, as shown in **Figure 5.7** and **Figure 5.8**. Firstly, in **Figure 5.7** (a) and (b), we show two models for the C_{70}/DT dimer row phase with the parallelogram unit cell. In the models below, the S-Au-S axis of the RS-Au-SR staple is represented with a horizontal bar, and the midpoint of the bar is where the Au adatom is located and it is above the bridge site of the Au(111) substrate. The illustration for this simplified model is shown in **Figure 5.7** (c).

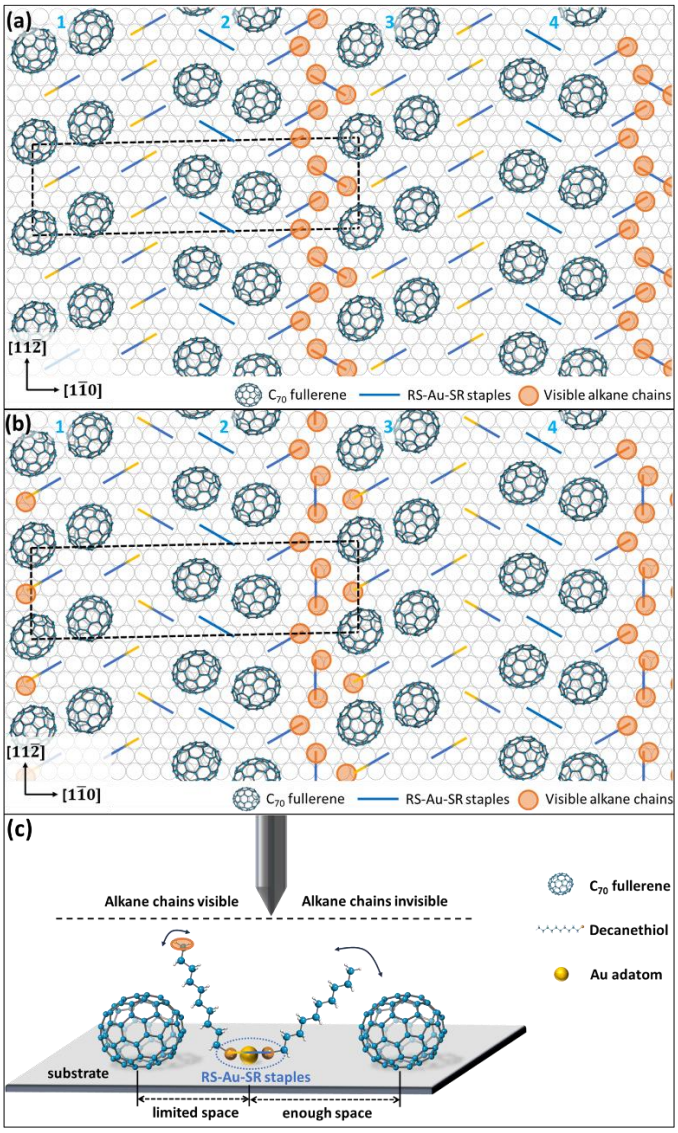

Figure 5.7 The possible models for C_{70}/DT dimer row phase with the parallelogram unit cell. The short bars in the dimer row gaps are the simplified model for RS-Au-SR staples, the centre of this simplified staple is located at the bridge site of Au(111) substrate. The highlighted orange spheres represent the single alkane chains we observed. (a) The model with fourteen DT molecules contained in each unit cell, and the coverage of DT is thus 0.142 ML. (b) The model with twelve DT molecules contained in each unit cell, and the coverage of DT is thus 0.122 ML. (c) Illustration of the simplified RS-Au-SR staple model. This RS-Au-SR staple is placed closer to the C_{70} on the left, thus there is less space for DT alkane chain to tilt, and the tail of alkane chain (highlighted in orange sphere) then becomes visible during scanning. While on the other side, the space between RS-Au-SR staple and C_{70} on the right is large enough, and it allows the

DT alkane chain to tilt with a larger range of angle, which is subject to a large uncertainty. And the alkane chain remains invisible during scanning. These two conditions correspond to the blue (invisible) and yellow (visible) parts of the bars in (a) and (b) respectively. The alkane chains marked in orange spheres are not only visible but can be individually distinguished.

In **Figure 5.7** (a), the staples are placed evenly into the gaps between each two dimer rows and the gaps between each two C_{70} dimers along $[11\bar{2}]$ direction. According to the positions of the visible DT alkane chains we observed in **Figure 5.5**, these blue bars are partly filled in yellow, suggesting that the alkane chains at these positions have significant different tilt angles. And the individually distinguished DT alkane chains are marked in orange spheres, as shown in the gap between dimer rows 2 and 3. Then following the positions of single alkane chains, we came up with this possible arrangement of RS-Au-SR staples in this gap and the other equivalent gaps. As we have no direct observation of DT alkane chains in the other type of gaps, considering about the stability of the C_{70}/DT dimer row phase, we place the DT in a row similar to the arrangement of DT within close-packed φ phase on Au(111) substrate. Overall, in this arrangement of both molecules, there are four C_{70} molecules and fourteen DT molecules in one unit cell, and the C_{70}-DT ratio is thus 2:7. The coverage of C_{70} within the dimer row phase is 0.041 ML, and the coverage of DT is 0.142 ML. As the DT alkane chains only have van der Waals interaction with C_{70} molecules, the carbon atoms from two different molecules have to keep a distance larger than the van der Waals diameter. The van der Waals radii of carbon atom is 0.170 nm[12], and in this model there is enough space for these two kinds of molecules. The DT alkane chains tilt with different angles, effectively filling the space and keeping C_{70} from joining together into close-packed phase.

However, in the model of **Figure 5.7** (a), the amounts of DT in two types of dimer row gaps are different, that there are two more DT molecules in the gap between dimer rows 2 and 3 (including the other equivalent gaps) in one unit cell. This will make the local coverage of DT in different gaps vary, which will further affect the stability of different C_{70} dimer rows. While we have not observed such a difference from our LT or RT data, this indicates that the local coverage of DT is supposed to be more equivalent. To make the local coverage of DT more equivalent, we have to adjust the number of RS-Au-SR staples in each unit cell, either by adding one staple to the gap between dimer row 1 and 2 or reducing one staple from the gap between dimer row 2 and 3. As the DT in the gap between dimer row 2 and 3 in **Figure 5.7** (a) is a little overcrowded (local

coverage = 0.231 ML, which is slightly higher than the coverage of δ phase DT before adding C_{70}), we removed one staple and rearrange the rest of staples, and the model is shown in **Figure 5.7** (b).

In the second model, with fewer DT are included in each unit cell, there are more possibilities for the arrangement of RS-Au-SR staples. Here in **Figure 5.7** (b), we present one of the most evenly placed DT arrangements. In this arrangement, the number of DT in the gaps of any two adjacent dimer rows is the same, which indicates that the C_{70} dimers can interact more uniformly with the surrounding DT alkane chains. Overall, there are four C_{70} molecules and twelve DT molecules in one unit cell, and the C_{70}-DT ratio is thus 1:3. The coverage of C_{70} within this second model for C_{70}/DT dimer row phase is 0.041 ML, and the coverage of DT is 0.122 ML. In each gap between dimer rows, the local coverage of DT is calculated to be 0.154 ML, which is in a reasonable range. Then, we also tried to add a staple into the gap between dimer row 1 and 2, but we are unable to find suitable and equivalent binding sites for all the staples in this gap.

In comparation of these two C_{70}/DT dimer row phase models in **Figure 5.7** (a) and (b), the first model contains more of DT molecules, and the enough amount of DT molecules can ensure that there are strong enough interactions between C_{70} and DT. While for the second model, the RS-Au-SR staples occupy the Au(111) substrate more evenly, and the equivalent arrangement of DT can ensure that the interactions between C_{70} and DT are uniform. Both of these two points mentioned are important factors for a long-range ordered self-assembled structure. Due to the lack of additional evidence of this structure, both models are considered to be possible.

As we mentioned in **Figure 5.6**, the unit cell of C_{70}/DT dimer row phase can be revised into a rectangular cell. Though there is only a tiny shift of C_{70} within the revised unit cell, the available binding sites of DT could be different. Similar with the process we built the first two models, we add the simplified RS-Au-SR staples into the gaps of C_{70} dimer rows, and the possible models are shown in **Figure 5.8**.

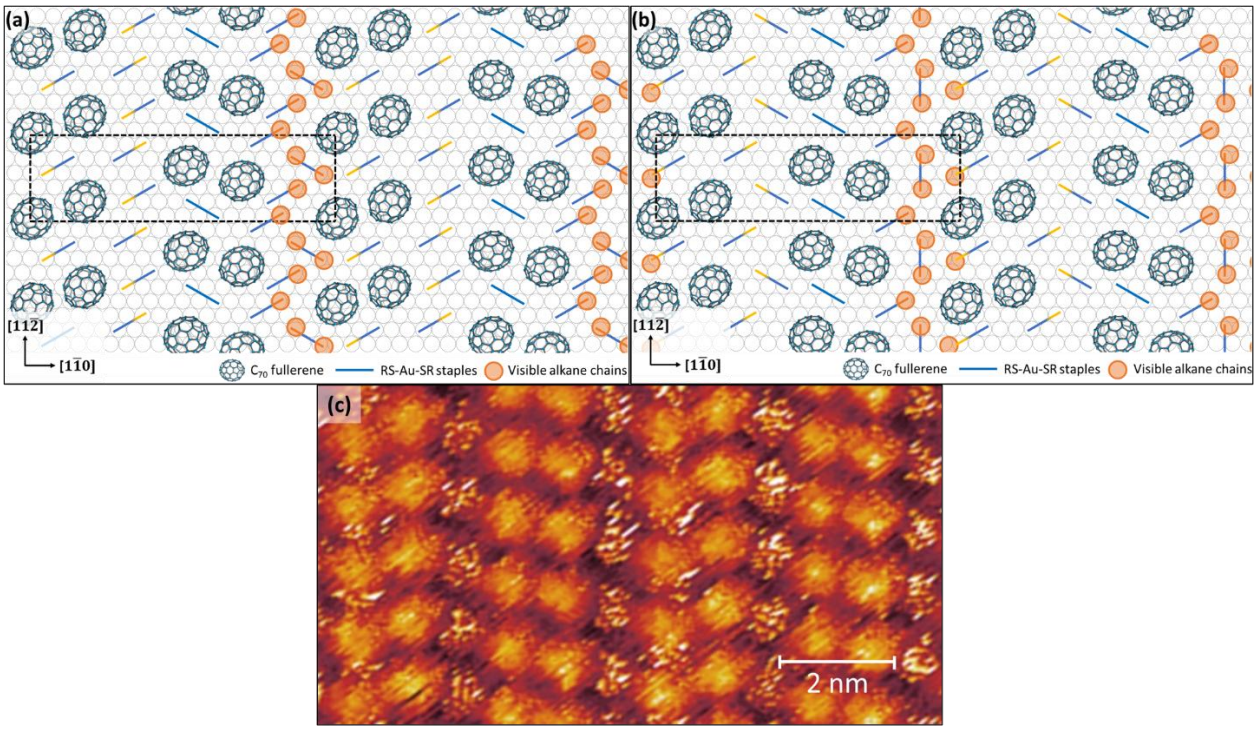

Figure 5.8 The possible models for C_{70}/DT dimer row phase with the rectangular unit cell. The RS-Au-SR staples are shown in short bars as well, the centre of this simplified staple is located at the bridge site of Au(111) substrate. The yellow parts of the bars represent the alkane chains here having limited space to tilt. (a) The model with fourteen DT molecules contained in each unit cell, and the coverage of DT is thus 0.142 ML. (b) The model with twelve DT molecules contained in each unit cell, and the coverage of DT is thus 0.122 ML. (c) The STM image from the C_{70}/DT dimer stripes for direct comparison with the structural model.

When we place the RS-Au-SR into the gaps, it is found that the arrangement of the staples can be exactly the same with the arrangement in **Figure 5.7** (a) and (b). In further comparison with the C_{70} arrangement in **Figure 5.6**, the corresponding C_{70} dimers have a maximum shift of 0.5a ($\approx$ 0.144 nm) in the [11$\bar{2}$] direction. However, due to the flexibility of the DT alkane chains, this tiny shift of C_{70} does not seem to be large enough to affect the arrangement of RS-Au-SR staples. And the distances between C_{70} and DT alkane chains can still be kept within a reasonable range ($>$ 0.170 nm)[12]. In **Figure 5.8** (c), an STM image of C_{70}/DT dimer row phase including signals from both C_{70} and DT molecules is displayed for direct comparison with the models we built. There is a good agreement between the model and the features shown in the STM image.

Overall, we have come up with four possible models for the C_{70}/DT dimer row phase, and each model has its justifications and limitations. For C_{70} molecules, if the C_{70}-Au interaction is much weaker than the S-Au interaction on C_{70}/DT/Au(111) sample, then the arrangement of C_{70} would be strongly affected by the arrangement of DT, and C_{70} could arrange into a parallelogram unit cell. Otherwise, they would arrange into a rectangular unit cell as the C_{70} in this arrangement have higher symmetry. Though there are references introducing the C_{70}-Au and DT-Au systems separately, we cannot directly compare them with these parameters, as there is also interaction between C_{70} and DT, which would also affect the C_{70}-Au and S-Au interactions. For DT molecules, though we can roughly derive the positions of DT according to the signals from the terminal groups of DT alkane chains, we still lack the direct observation of the head groups of DT, which leads to a large uncertainty about the coverage of DT in the C_{70}/DT dimer row phase.

2.4 Models for C_{70}/DT Trimer Row Structure

Similar to the procedures we applied to build the models for the C_{70}/DT dimer row phase, we firstly placed the C_{70} onto the Au(111) substrate according to our measurements in **Figure 4.3**, and the initial model is shown in **Figure 5.9** (a). As we have not directly observed the clear molecular orientations of C_{70} within the C_{70} trimers, we use the same orientation for these C_{70} as the orientation in C_{70} dimers. And we place these C_{70} on the Au(111) substrate with their short axis parallel to the $[11\bar{2}]$ direction, so that the distances between C_{70} in the model would not be too close and they would match better with our previous measurements. The C_{70} within the C_{70} trimers are highlighted in orange, which occupy the bridge sites of Au(111) substrate. For the C_{70} within the dimer rows in this model, they are arranged into the parallelogram unit cell as shown in **Figure 5.6** (a) so that the overall arrangement of C_{70} is more consistent with our measurements. The repeating distance of C_{70} trimers along the $[11\bar{2}]$ direction is $6\sqrt{3}$a, and parameters specifying the internal structure of the trimer of C_{70} trimers are: a = 1.11 ± 0.02 nm, b = 1.11 ± 0.02 nm, c = 1.57 ± 0.05 nm, γ = 93.2 ± 0.4°. In this arrangement, the local coverage of C_{70} is calculated to be 0.044 ML.

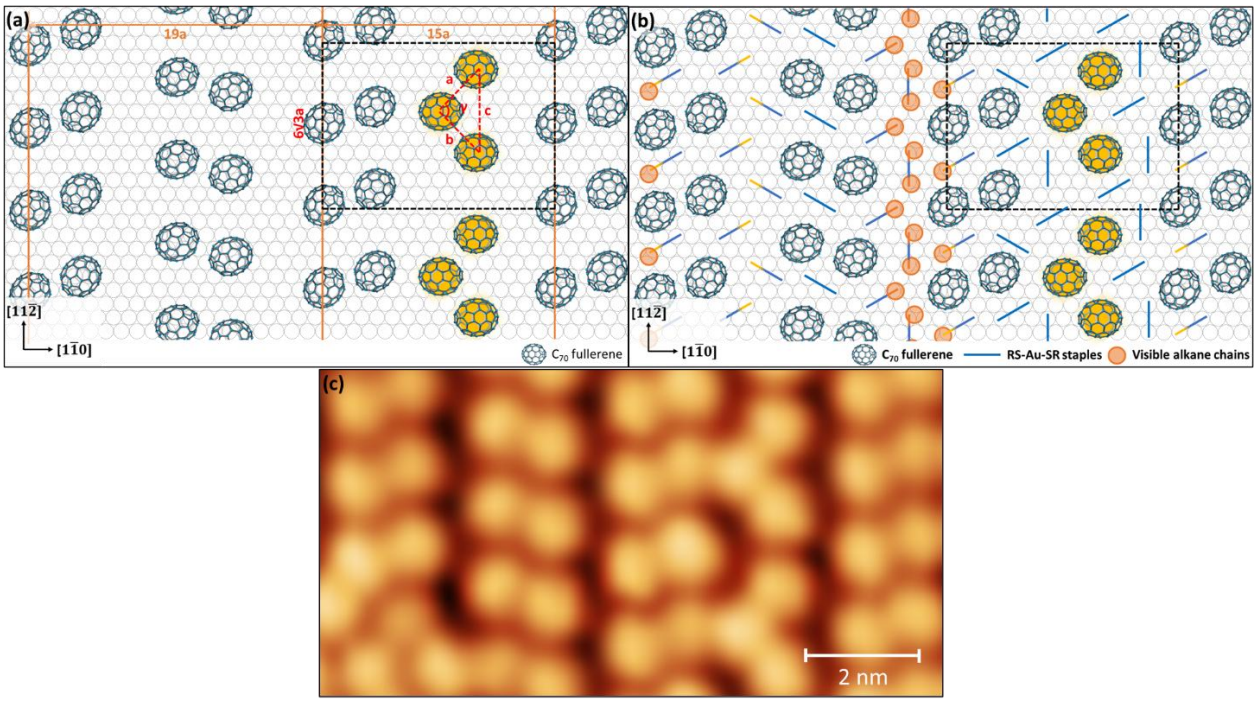

Figure 5.9 (a) The model showing the arrangement of C_{70} within the trimer row in between two dimer rows with 70-degree dimer axis on Au(111) substrate. The C_{70} trimers are highlighted in orange, and the local coverage of C_{70} is 0.044 ML. (b) The possible arrangement of RS-Au-SR staples around the C_{70} trimer row. The RS-Au-SR staples are still shown in blue bars. The local coverage of DT is 0.128 ML. (c) STM image of C_{70} trimer row for direct comparation with the model.

Then we tried to add the RS-Au-SR staples into the gaps between C_{70} molecules. The staples around the dimer rows have the same arrangements as shown in **Figure 5.7** (b). As the space around the C_{70} trimers is relatively larger, there are more possible arrangements of the RS-Au-SR staples. Considering that the C_{70} trimer rows always coexist with the C_{70} dimer rows, which indicates that the coverage of DT within the two structures is similar, we then present a model in **Figure 5.9** (b) of which the DT coverage around C_{70} trimers is close to the coverage in dimer row phase. In this arrangement, the DT coverage of C_{70} trimer row is 0.128 ML, which is higher than the coverage of dimer rows (0.122 ML). A STM image of the C_{70} trimer row is shown in Figure 5.9 (c), which corresponds to the model we built.

In addition to the C_{70}/DT trimer row shown above, which formed in between the dimer rows with 75-degree dimer axis, we also find the other type of C_{70} trimer row formed in between the dimer

rows with 70-degree dimer axis. **Figure 5.10** (a) shows the arrangement of C_{70} within this type of C_{70}/DT trimer row. The C_{70} within the trimers in **Figure 5.10** (a) have the same molecular orientation, and they occupy the bridge sites of the Au(111) substrate as well. In comparison with the arrangement of C_{70} in **Figure 5.9** (a), there is no other difference except for the dimer axis orientation of the neighbouring C_{70} dimer rows. The local coverage of C_{70} is still 0.044 ML.

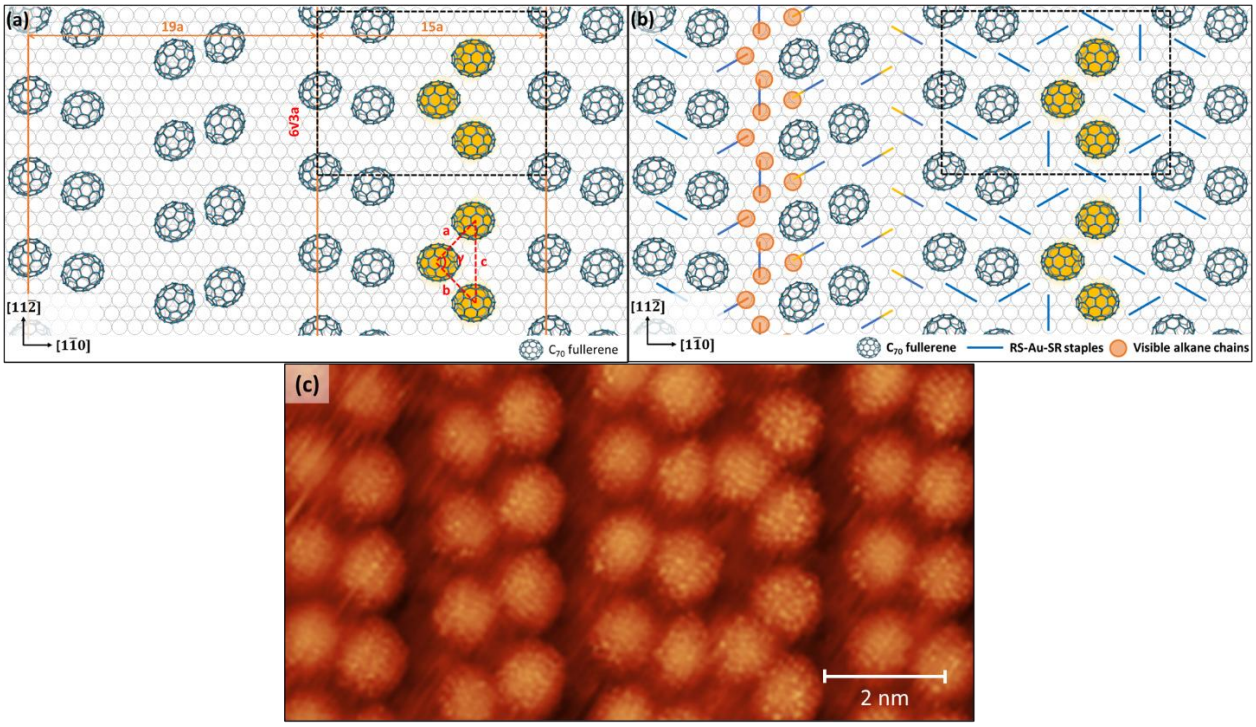

Figure 5. 10 (a) The model showing the arrangement of C_{70} within the trimer row in between two dimer rows with 75-degree dimer axis on Au(111) substrate. The C_{70} trimers are highlighted in orange. (b) The possible arrangement of RS-Au-SR staples around the C_{70} trimer row. (c) STM image of C_{70} trimer row for direct comparation with the model.

For the arrangement of DT, due to the different occupations of C_{70} in 75-degree and 70-degree oriented dimer rows, the available binding sites in the gaps between C_{70} and C_{60} dimer rows are different. After roughly counting the number of the two types of C_{70} trimer rows, since they appear with similar probabilities on the sample, we then place the same number of RS-Au-SR staples into the gaps evenly. **Figure 5.10** (b) shows the arrangement of RS-Au-SR staples around the second type of C_{70} trimer row, and the local coverage of DT molecules is 0.128 ML. The STM image in **Figure 5.10** (c) shows the area corresponding to this type of C_{70} trimer row.

2.5 Models for C_{70}/Decanethiol Porous Framework Structure

Though the C_{70}/DT porous framework phase is not as frequently observed as the C_{70}/DT dimer row phase, there is still enough information for us to build up a reasonable model for this structure. According to our observation in **Figure 5.3**, the C_{70} within each C_{70} dimer can be divided into two types. In order to distinguish between these two types of C_{70}, we define the C_{70} that the molecular orientation can be clearly observed as type 1 and the C_{70} for which we cannot observe the orientation as type 2. As we previously discussed, the type 1 C_{70} are likely to occupy the equivalent binding sites on Au(111) surface. Since type 1 C_{70} have specific molecular orientation and seem to have a regular arrangement, we placed these C_{70} on to the model for Au(111) substrate first. Then for the type 2 C_{70}, though their relative site positions can be derived from the positions of neighbouring type 1 C_{70}, we still need to find out the possible molecular orientation of them. According to the distance between type 1 and 2 C_{70} within each dimer (1.04 ± 0.02 nm), as we mentioned in **Figure 4.7** (b), which is close to the distance between two standing up C_{70}[13], we then derived that type 2 C_{70} is standing up with its long axis perpendicular to the Au(111) surface.

By adjusting the binding sites of two types of C_{70} on Au(111) substrate, we finally came up with a relatively reasonable model for the arrangement of C_{70} within the C_{70}/DT porous framework phase, as shown in **Figure 5.11** (a). In this model, the two types of C_{70} within a dimer, as marked in red dashed frame, are filled in yellow and blue respectively. For the type 1 C_{70} in yellow, they occupy the three-fold hollow sites with a carbon atom in contact with the Au(111) substrate. For the type 2 C_{70} in blue, they occupy the bridge sites with a pentagonal ring in contact with the Au(111) substrate. The distance between the type 1 and 2 C_{70} is 1.04 ± 0.02 nm, which is closer than that of the C_{70} dimer within C_{70}/DT dimer row phase. Though the type 1 C_{70} is also lying down on Au(111) substrate, its long axis is parallel to the $[1\bar{1}0]$ direction and perpendicular to the C_{70} dimer axis which is parallel to the $[11\bar{2}]$ direction. Thus in this arrangement, the distance between the type 1 and 2 C_{70} can be almost the same with the distance between two standing up C_{70}. The unit cell of C_{70}/DT porous framework phase is marked in black dashed parallelogram, and the unit cell parameters are: a = 1.81 ± 0.03 nm, b = 1.65 ± 0.05 nm, γ = 70.0 ± 0.5°.

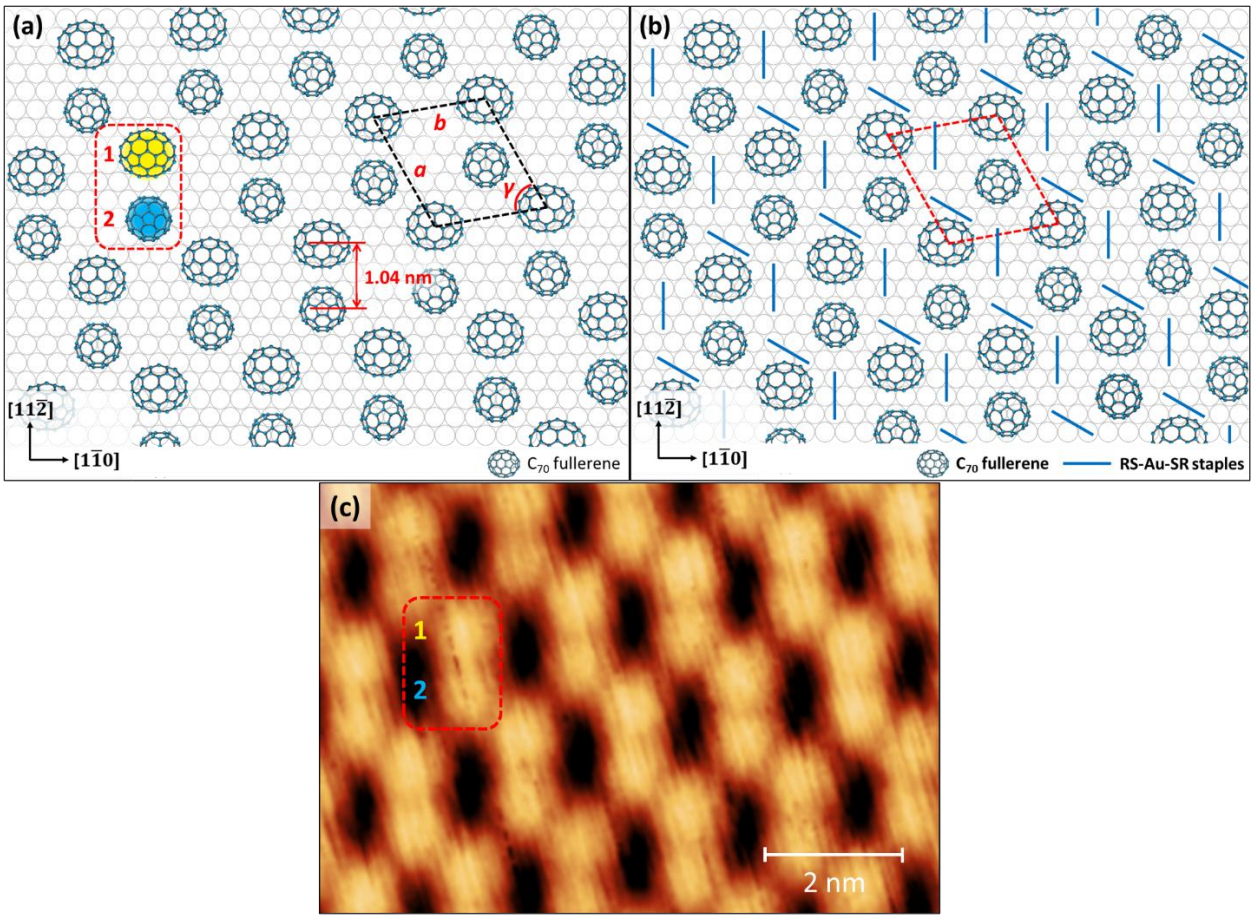

Figure 5.11 (a) The arrangement of C_{70} within C_{70}/DT porous framework phase. The type 1 C_{70} marked in yellow occupy the three-fold hollow sites of Au(111) substrate in the molecular orientation with a carbon atom facing up. The type 2 C_{70} marked in purple occupy the bridge sites of Au(111) substrate in the molecular orientation with a pentagonal ring facing up. The distance between type 1 and 2 C_{70} within each C_{70} dimer is 1.04 ± 0.02 nm. The unit cell parameters of C_{70}/DT porous framework structure are: a = 1.81 ± 0.03 nm, b = 1.65 ± 0.05 nm, γ = 70.0 ± 0.5°. The coverage of C_{70} in this arrangement is 0.070 ML. (b) The possible arrangement of DT within C_{70}/DT porous framework phase. There are two RS-Au-SR staples contained in each unit cell, and the coverage of DT is 0.140 ML. (c) The STM image of C_{70}/DT porous framework phase for direct comparison. The C_{70} molecules marked in red dashed frame correspond to the type 1 and 2 C_{70} in (a).

Due to the lack of direct observation of DT inside the pores, the arrangement of DT could only be deduced through simplified modelling analysis. According to our previous inference, the porous

framework phase requires higher coverage of DT to be maintained. However, comparing with the regular gaps in between the C_{70} dimer rows, the space in the pores of this framework is relatively more separated due to the arrangement of C_{70}, and thus the available binding sites in each pore are more limited. After careful adjustment, we came up with a reasonable arrangement of RS-Au-SR staples in C_{70}/DT porous framework phase, as shown in **Figure 5.11** (b). When we place two RS-Au-SR staples in one unit cell in this arrangement, the space inside the pores can be filled more evenly and sufficiently by the DT alkane chains. If we add one more staple into the pore, the distance between alkane chains and C_{70} would be too close, which could cause a strong competition between C_{70} and DT. On the other hand, if we only place one staple into the pore, there would be enough space for DT alkane chains to tilt freely with a large angle, and that they could not be able to stabilise all the surrounding C_{70}. In this arrangement of DT, the type 2 C_{70} could be pushed out from a more preferred binding site by the surrounding DT alkane chains, which makes them bind less stably on the Au(111) substrate. Overall, there are two C_{70} molecules and four DT molecules included in one unit cell, and the C_{70}-DT ratio is thus 1:2. The coverage of C_{70} within this C_{70}/DT porous framework phase model is 0.070 ML, and the coverage of DT is 0.140 ML, which are both higher than the coverages of C_{70} and DT in the dimer row phase. And that may help to explain the difference in thermal stability between these two structures.

Before we conducted the thermal annealing for the C_{70}/DT/Au(111) sample, the distribution of C_{70} is not even as they are deposited randomly on to the DT/Au(111) surface. And even for DT molecules on Au(111) surface, though we have annealed the sample to reduce the DT coverage, the DT do not evenly desorb from the surface due to the tiny temperature differences in different regions of sample, and some of DT still shown in close-packed φ phase as we mentioned in **Figure 4.1** (d). This uneven distribution makes it possible for various phases appearing on the Au(111) sample simultaneously (DT in φ phase and δ phase, C_{70}/DT in dimer row phase, porous framework phase and disordered phase). Though the C_{70} and DT molecules are still available to diffuse on the substrate at RT, they are both unable to travel a long distance due to their interactions with the surrounding molecules. C_{70} are mainly obstructed by the van der Waals interaction between them and DT alkane chains. For DT, they are not only obstructed by the van der Waals interaction with the neighbouring C_{70} and DT alkane chains, but also be held in the RS-Au-SR staples by the S-Au bond[10]. The thermal annealing, however, provides both molecules with sufficient thermal energy to overcome the energy barrier and diffuse more freely across the sample surface[14]. Then after

thermal annealing, C_{70} and DT molecules both have a more even distribution on Au(111) substrate, and those phases which require higher local molecular coverage (e.g. φ phase DT) are not available to reform. According to the analysis above, it is likely that the C_{70}/DT porous framework phase formed in the regions where the molecular coverage is relatively higher, and this phase disappeared when the molecular coverage dropped. This is consistent with our results in thermal annealing experiment and prove that the model we built for C_{70}/DT porous framework is reasonable.

3. Conclusion

In this chapter, the details of C_{70} and DT within the C_{70}/DT self-assembled structures are revealed through LT scanning at 77 K. The C_{70}/DT dimer row structure, C_{70}/DT porous framework structure and the C_{70}/DT trimer row structure are analysed in detail, and possible models of each structure showing the arrangements of C_{70} and DT on Au(111) substrate are established.

In the C_{70}/DT dimer row structure, C_{70} molecules are found arrange into two kinds of dimer rows of which having the dimer axes in two different directions. With the DT molecules efficiently filling in the gaps, some local C_{70} dimer rows are thus stabilised and expand into a long-range ordered dimer row phase. The C_{70} within the dimer rows have specific molecular orientation, which occupy the Au(111) substrate with their long axes almost parallel to the surface. The DT molecules form as a RS-Au-SR unit, and they are stabilised by the S-Au bond with Au adatoms, which occupy the bridge sites of Au(111) substrate. In addition, for the single C_{70}/DT trimer row appearing within the C_{70}/DT dimer row phase, though we have not observed clear molecular orientations of these C_{70} molecules, we still come up with a relatively reasonable model for C_{70}/DT trimer row structure according to the distance and the shape of C_{70}.

The C_{70} dimers in C_{70}/DT porous framework structure have a more regular arrangement, as the dimer axes of all the C_{70} dimers are in the same direction. The arrangement of C_{70} is this structure is thus considered to be more compatible with the binding sites of Au(111) substrate. With no direct observation of DT molecules within the pores, we derived the possible arrangement of DT according to the features of C_{70}/DT porous framework structure introduced in the pervious chapter. To meet with the feature that this structure has the weaker thermal stability than dimer row structure, a model of C_{70}/DT porous framework structure with more DT molecules filled in the gap is thus established.

Reference

[1] Meyer, G.; S. Zöphel; Rieder, K. H. Manipulation of Atoms and Molecules with a Low Temperature Scanning Tunneling Microscope. *Appl. Phys. A* **1996**, *63*, 557–564.

[2] Hao, Y.; Wang, Y.; Vasilii Dubrovin; Avdoshenko, S. M.; Popov, A. A.; Liu, F. Caught in Phase Transition: Snapshot of the Metallofullerene $Sc_3N@c_{70}$ Rotation in the Crystal. *J. Am. Chem. Soc.* **2020**, *143*, 612–616.

[3] Guo, Q.; Li, F. Self-Assembled Alkanethiol Monolayers on Gold Surfaces: Resolving the Complex Structure at the Interface by STM. *Phys. Chem. Chem. Phys.* **2014**, *16*, 19074.

[4] Wang, H.; Zeng, C.; Wang, B.; Hou, J. G.; Li, Q.; Yang, J. Orientational Configurations of the C_{60} Molecules in the (2×2) Superlattice on a Solid. *Phys. Rev. B* **2001**, *63*, 085417.

[5] Niu, G.; Geng, J.; Wang, X.; Yang, X.; Xiong, W.; Zhang, H.; Ruan, Z.; Zhang, Y.; Gao, L.; Lu, J.; Cai, J. Adsorption Configurations and Electronic Properties of Self-Assembled C_{60} and C_{70} Molecules on a Semiconductor CuSe Monolayer with Periodic Nanopores. *Nanotechnology* **2023**, *34*, 395602–395602.

[6] Bumm, L. A.; Arnold, J. J.; Dunbar, T. D.; Allara, D. L.; Weiss, P. S. Electron Transfer through Organic Molecules. *J. phys. chem. B* **1999**, *103*, 8122–8127.

[7] Binnig, G.; Rohrer, H.; Gerber, Ch.; Weibel, E. Surface Studies by Scanning Tunnelling Microscopy. *Phys. Rev. Lett.* **1982**, *49*, 57–61.

[8] Wiesendanger, R. *Scanning Probe Microscopy and Spectroscopy: Methods and Applications*; Cambridge University Press, 1994.

[9] Chen, T.; Howells, S.; Gallagher, M.; D. Sarid; Lamb, L. D.; Huffman, D. R.; Workman, R. K. Scanning-Tunneling-Microscopy and Spectroscopy Studies ofc70Thin Films on Gold Substrates. *Phys. Rev. B* **1992**, *45*, 14411–14414.

[10] Maksymovych, P.; Oleksandr Voznyy; Dougherty, D. B.; Sorescu, D. C.; Yates, J. R. Gold Adatom as a Key Structural Component in Self-Assembled Monolayers of Organosulfur Molecules on Au(111). *Prog. Surf. Sci.* **2010**, *85*, 206–240.

[11] Rai, A.; Singh, V. K.; Nayak, J.; Roy Barman, S. Parameter Dependent Fabrication of Chromium Nano-Structures on Au(111) Surface. *Surf. Sci.* **2019**, *679*, 169–173.

[12] Bondi, A. Van Der Waals Volumes and Radii. *J. Phys. Chem.* **1964**, *68*, 441–451.

[13] Guo, L.; Wang, Y.; Kaya, D.; Palmer, R. E.; Chen, G.; Guo, Q. Orientational Epitaxy of van Der Waals Molecular Heterostructures. *Nano Lett.* **2018**, *18*, 5257–5261.

[14] Wang, S.; Kyriakos Komvopoulos. Structure Evolution during Deposition and Thermal Annealing of Amorphous Carbon Ultrathin Films Investigated by Molecular Dynamics Simulations. *Sci. Rep.* **2020**, *10*, 8089.

VI. C_{60}/C_{70}/Decanethiol Multicomponent Self-Assembly

1. Introduction

In the previous chapters, we introduced the bicomponent self-assembly of C_{70}/DT system on Au(111) substrate. In comparation with the self-assembly of C_{60}/DT system previously reported by our group[1,2], the self-assembly of C_{70}/DT system seems to be rather different, as there are obviously less self-assembled structures observed in C_{70}/DT system. This difference is considered to be strongly related to the geometric shape of C_{60} and C_{70} molecules[3,4], which have been introduced in chapter II. To further understand the difference between C_{60}/DT self-assembly and C_{70}/DT self-assembly, it would be more straightforward to observe and compare their self-assembled structures on the same sample.

Considering that the pre-existing self-assembled structure could affect the self-assembly process of the later added fullerene, we plan to prepare three such samples where the amount of C_{60} and C_{70} deposited onto the substrate is close, but they are deposited in different ways. For the first sample, the C_{60} molecules are firstly deposited onto the δ phase DT/Au(111) substrate. When the C_{60} have formed their stable self-assembled structures with DT, the C_{70} are then add to the C_{60}/DT/Au(111) sample. For the second sample, the C_{70} are deposited onto the δ phase DT/Au(111) substrate firstly and then followed by C_{60}. These first two samples are also treated with thermal annealing, so that both fullerene and DT molecules are well mixed and distribute more evenly on the substrate. For the third sample, the C_{60} and C_{70} are simultaneously deposited onto the δ phase DT/Au(111). Both C_{70} and C_{60} molecules are thus well mixed on the sample after deposition, while the distribution of DT remains uneven, which makes it possible for more fullerene/DT self-assembled structures to appear.

Through the RT scanning of these samples, our work in this chapter reveal a special property of the fullerene/DT self-assembly, that the fullerene molecules with different symmetries have the ability to arrange into any self-assembled structures of the other fullerene by adjusting their molecular orientations and binding sites on Au(111) substrate. With the guidance of the pre-

existing self-assembled structural inertia and the proper fullerene-DT ratio, the C_{60} and C_{70} at the boundaries are both observed to join and form into the C_{60}-C_{70} ordered phases.

2. Sample Preparation

As we planned, for this experiment, three fullerene/DT/Au(111) samples were prepared for comparison. The substrates used for these samples were the (111)-oriented gold thin films grown on ZYB grade HOPGs. The gold films were prepared through vapour deposition, and the thickness of each gold film was about 300 nm. The details of gold film preparation were the same as we mentioned in Chapter IV. Later on, each sample was treated with several cycles of Ar^+ ion sputtering (1.5 keV, 7 minutes) and thermal annealing (550 °C) under UHV conditions. All the prepared Au(111) films were then transferred out and immersed into a 1 mM 1-decanethiol solution in ethanol (99.5%) for 12 hours at RT. The Au(111) films covered by close-packed φ phase DT were transferred back into UHV chamber for thermal annealing (120 °C, 1 hour). The annealing for each sample was conducted on the same manipulator with the same annealing parameters, and the vacuum within the UHV chamber was kept at the same level (< 1.0×10^{-8} mbar). Through the partial thermal desorption, the reduction of DT coverage results in the transition from the closed-packed φ phase DT (0.33ML)[5] to a low coverage δ phase (0.23ML)[6].

After the preparation of these same δ phase DT/Au(111) samples, we used three different ways to deposit the C_{60} and C_{70} fullerenes.

i) C_{60} were firstly deposited onto the DT/Au(111) sample. The evaporation source of C_{60} was heated up to 410 °C, and the deposition time was 10 minutes. After the deposition, the C_{60}/DT/Au(111) sample was left at RT for 72 hours, during which most of the C_{60} formed various self-assembled structures with DT. When we observed from the STM images that most of C_{60}/DT arranged into ordered phases, the sample was then deposited with C_{70}. As we previously mentioned that the coverage of C_{70} after 1 minute of deposition at 409 °C is higher than expected, we reduced the temperature of C_{70} evaporation source to 370 °C and increased the deposition time to 5 minutes, and the coverage of C_{70} reduced to two thirds of previous coverage.

ii) C_{70} were firstly deposited onto the DT/Au(111) sample. In order to keep the same coverages of C_{60} and C_{70} on both samples, we used the same parameters for deposition. The evaporation source of C_{70} was heated up to 370 °C, and the deposition time was 5 minutes. After the deposition, the

C_{70}/DT/Au(111) sample was left at RT for 72 hours, during which most of the C_{70} formed dimer row phase and porous framework phase with DT. The C_{60} were then deposited onto the C_{70}/DT/Au(111) sample at 410 °C for 10 minutes.

iii) The evaporation sources of C_{60} and C_{70} were heated up to 410 °C and 370 °C respectively at the same time, and the DT/Au(111) sample was exposed simultaneously to the C_{60} and C_{70} sources for 10 minutes and 5 minutes respectively.

3. Results and Discussion

The scanning of the sample in this experiment is conducted in UHV (~ 1.0×10^{-11} mbar) at RT (~ 290 K) after each step of preparation. **Figure 6.1** (a) shows a 300 nm × 300 nm area on one of the Au(111) substrates used for this experiment, and the other two Au(111) substrates have the same qualities. The herringbone reconstructions of Au(111) surface can be clearly observed.

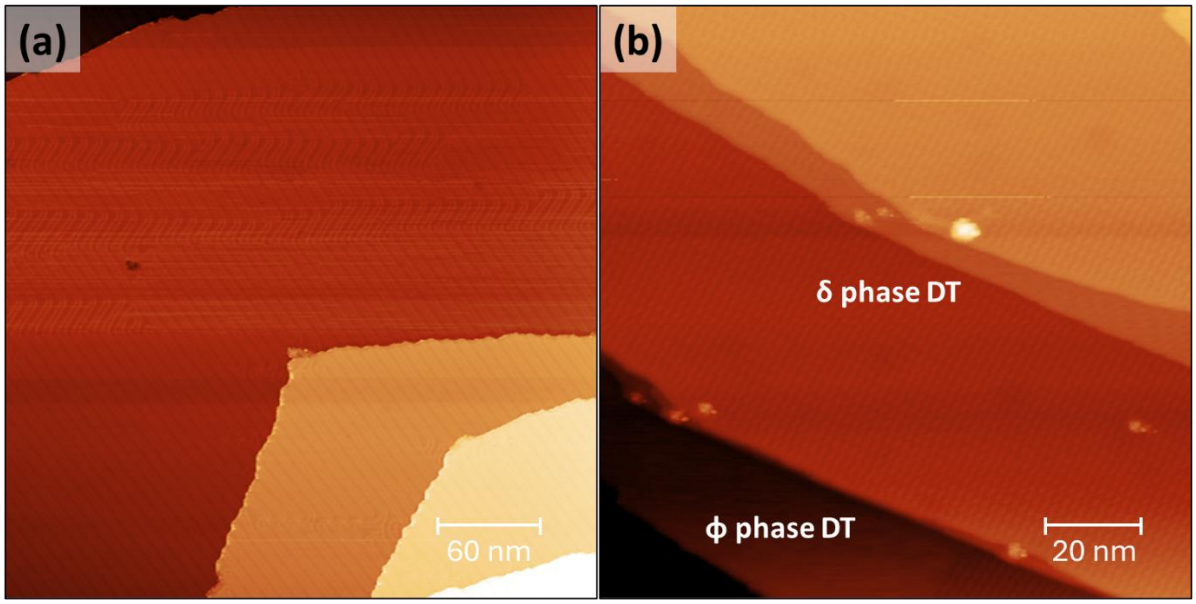

Figure 6.1 (a) The clean Au(111) substrate after several cycles of ion sputtering and thermal annealing. (b) The δ phase DT on Au(111) substrate.

Figure 6.1 (b) shows the DT on Au(111) substrate after annealed at 120 °C for 1 hour. Similar with the DT/Au(111) sample we observed in **Figure 4.1** (b), over 90% of DT changed from close-packed φ phase into the δ phase after annealing, and the rest of DT remained in φ phase. The single bright spots on the DT/Au(111) surface are likely to be the contaminants absorbed on the Au(111)

substrate during the liquid phase deposition process. After we have confirmed from the STM images that the Au(111) substrate is ready for further preparation, the gold film is transferred into the ambient atmosphere first and then into the decanethiol solution, during which a small amount of contaminants will be absorbed onto the sample surface. Though thermal annealing at 550 °C could effectively remove most of these contaminants, we are only able to anneal the sample up to 120 °C, which is the minimum temperature for DT desorption from Au(111) substrate. Fortunately, these contaminants would not affect our observation of fullerene molecules, as they appear much taller than the contaminants.

3.1 Au(111)-Decanethiol-C_{60} + C_{70}

3.1.1 C_{60}/Decanethiol Dimer Frameworks on Au(111)

The C_{60}/DT/Au(111) sample has been left at RT for 72 hours before scanning. And after rough calculations, it is found that over 90% of C_{60} have formed stable self-assembled structures with DT. **Figure 6.2** (a) shows the self-assembled phases of C_{60}/DT system on Au(111) substrate. In this area, the C_{60} form various dimer frameworks with the participation of DT, which is consistent with the C_{60}/DT self-assembled structures introduced in the previous works[1,2,7]. In comparation with the self-assembled structures of C_{70}/DT system, the self-assembly of C_{60}/DT system is more complicated, which may be due to the higher symmetry of the C_{60} molecules. The spherical structure of C_{60} molecule makes it possible for two C_{60} to form dimers in various ways. Though some of these C_{60} dimers are less stable, they could still arrange on the Au(111) substrate with the supporting of DT alkane chains. The C_{70}, however, have a lower symmetry than C_{60}[8,9], and due to the ellipsoidal structure of C_{70}, the binding energy varies obviously when C_{70} bind to the substrate in different ways[10]. As we mentioned in Chapter IV, that the C_{70} dimers are not found to exist on their own, and it requires at least three C_{70} dimer rows to stabilise all the C_{70} dimers in their positions. While for C_{60}, we could easily find the individual C_{60} dimers within both ordered and disordered C_{60}/DT domains. And then those individual C_{60} dimers with different or same dimer axis further arrange into different dimer frameworks with the participation of DT on Au(111) substrate, as shown in **Figure 6.2** (a).

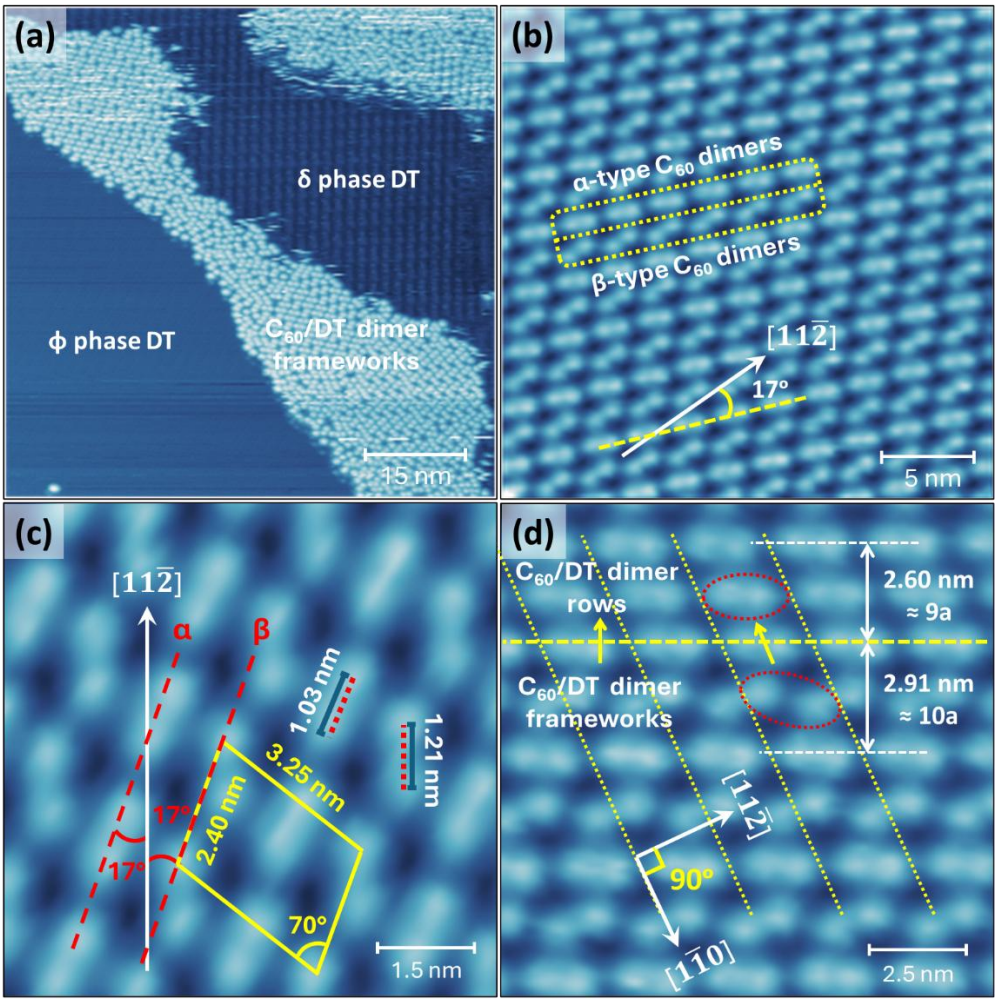

Figure 6.2 (a) The STM image of C_{60}/DT dimer framework phase collected 72 hours after deposition of C_{60}. The C_{60}/DT dimer frameworks coexist with DT in both δ phase and φ phase. The C_{60} dimers arrange into various frameworks within this domain. (b) One of the C_{60}/DT dimer frameworks. The C_{60} dimers within this framework have two arrangements, where the β-type C_{60} dimer has its dimer axis parallel to the $[11\bar{2}]$ direction, and the α-type C_{60} dimer has its dimer axis 17.0 ± 0.5° off the $[11\bar{2}]$ direction. Both types of C_{60} dimers arrange on Au(111) substrate in the direction 17.0 ± 0.5° off the $[11\bar{2}]$ direction. (c) The measurements for C_{60}/DT dimer framework phase. The distances of two C_{60} molecules within the α-type dimer and β-type dimer are respectively 1.03 ± 0.02 nm and 1.21 ± 0.02 nm. The unit cell parameters for this framework are: a = 3.25 ± 0.06 nm, b = 2.40 ± 0.05 nm, γ = 70.0 ± 0.5°. (d) The STM image showing the phase changing from C_{60}/DT dimer framework structure to C_{60}/DT dimer row structure.

Among several of these C_{60}/DT dimer framework structures, we mainly focused on this particular structure shown in **Figure 6.2** (b), which is found strongly relate to the mixed fullerene self-assembled structures we will discuss later. In this dimer framework, the C_{60} dimers have two different arrangements on Au(111) substrate, thus we divide the C_{60} dimers into α-type and β-type, as marked in the yellow dotted frames. The α-type C_{60} dimer has its dimer axis 17° off the $[11\bar{2}]$ direction, and the β-type C_{60} dimer has its dimer axis parallel to the $[11\bar{2}]$ direction. Both two types of C_{60} dimers arrange in the direction 17.0 ± 0.5° off the $[11\bar{2}]$ direction.

In **Figure 6.2** (c), the measurements of this C_{60}/DT dimer framework are shown in detail. For the α-type C_{60} dimers, since the direction of their dimer axes is parallel to the arrangement direction of C_{60} dimers, the distance of C_{60} within the α-type dimer is measured to be 1.03 ± 0.02 nm, which is close to the distance of C_{60} in close-packed phase. However, as there are some DT alkane chains filling the gaps of C_{60} dimers, the α-type C_{60} dimers cannot assemble together along the $[11\bar{2}]$ direction to form close-packed C_{60} chains but remain separate. For the β-type C_{60} dimers, the distance of C_{60} is measured to be 1.21 ± 0.02 nm. This distance is relatively large, and the term "dimer" in this case is used mainly to reflect that the two molecules are paired. With their dimer axes in the direction 17.0 ± 0.5° off the arrangement direction of C_{60} dimers, there is more space that can be occupied by the β-type C_{60} dimers, which leads to different spacing of the C_{60} molecules in α-type and β-type. The unit cell of this dimer framework is shown in yellow parallelogram in **Figure 6.2** (c). Each unit cell contains four C_{60} molecules, and the number of DT molecules within each unit cell will be discussed later with the model of this structure. The unit cell parameters of this C_{60}/DT dimer framework are: a = 3.25 ± 0.06 nm, b = 2.40 ± 0.05 nm, γ = 70.0 ± 0.5°.

In addition, we also notice the phase changing from C_{60}/DT dimer framework structure to C_{60}/DT dimer row structure in some regions, as shown in **Figure 6.2** (d). The C_{60}/DT dimer rows, as highlighted in yellow dotted lines, have their directions of 90.2 ± 0.4° off the $[11\bar{2}]$ direction, which is parallel to the $[1\bar{1}0]$ direction of Au(111) substrate. When we observe these two structures along the $[1\bar{1}0]$ direction, it is found that the C_{60}/DT dimer framework structure actually can be considered as a special C_{60}/DT dimer row structure which has a larger gap in between each two C_{60} dimers. According to our measurement, the gap of dimer framework structure is approximately 0.31 ± 0.03 nm (≈ 1a) larger than that of dimer row structure, which indicates that there are more DT molecules distributed within the gaps of dimer framework structure. While, if there is not

enough DT molecules filling in the gap of C_{60}/DT dimer frameworks, the two separated C_{60} would get closer and dimerize, as highlighted in red dotted circles, which would further lead to a phase changing to C_{60}/DT dimer row structure. And more details of C_{60}/DT dimer row structure will be introduced later.

3.1.2 Phase Changing after C_{70} Added to C_{60}/Decanethiol/Au(111) Sample

When the C_{60} are stabilised on DT/Au(111) surface, C_{70} molecules are then directly deposited to the C_{60}/DT/Au(111) sample. To find out the effect of the C_{60}/DT dimer frameworks on the formation of C_{70}/DT self-assembled structures, we scanned the sample in different periods after the deposition of C_{70}. **Figure 6.3** (a) shows the STM image collected within 24 hours after the deposition. In this area, there is clear boundary between the C_{60}/DT dimer framework phase and the disordered C_{70}/DT phase, which is highlighted in a yellow dotted line. For the C_{70} deposited on pure δ phase DT/Au(111) substrate, as we mentioned in **Figure 4.4**, it takes about 24 hours for the C_{70}/DT dimer rows to initially form and stabilise. In comparison with the C_{70} deposited on C_{60}/DT/Au(111) sample, there appears to be no significant difference in the behaviour of the C_{70} molecule. It indicates that the C_{60}/DT dimer framework does not directly guide or accelerate the self-assembly process of the disordered C_{70}, and the C_{60}/DT phase and C_{70}/DT phase are relatively independent of each other. It is also noticed that there are some brighter molecules randomly arrange within the C_{60}/DT domain, which are likely to be the C_{70} molecules landing directly into the gaps of C_{60}/DT dimer frameworks. As the space within the gaps of framework is limited, the C_{70} could be forced to standing up with their long axes perpendicular to the Au(111) substrate due to the compression of surrounding C_{60}, and thus those individual C_{70} looks brighter than the C_{60} within the C_{60}/DT dimer frameworks.

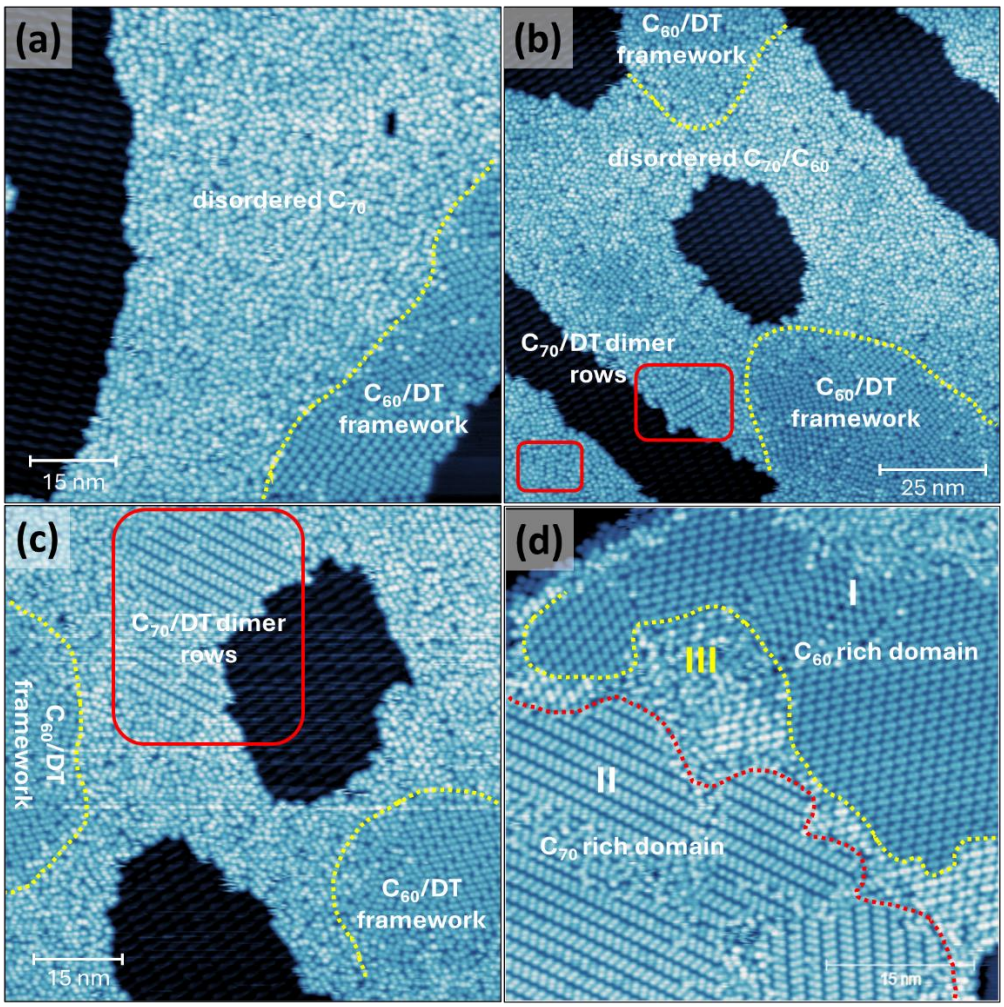

Figure 6.3 (a) The STM image of C_{70}+C_{60}/DT/Au(111) sample collected within 24 hours after the deposition of C_{70}. The boundary of C_{60}/DT and C_{70}/DT is highlighted in yellow dotted line. The C_{70}/DT remains in disordered phase. (b) The STM image collected 24 hours after the deposition of C_{70}. In the middle region, C_{60} and C_{70} gradually diffuse together into a large disordered mixture domain. However, the heights of C_{70} with different molecular orientations exhibit obvious difference (brightness of the molecule), making it difficult to distinguish between C_{60} and C_{70} in this region. In the C_{70} rich regions, as highlighted in red frames, The C_{70} start to form dimer row phase. The regions of C_{60}/DT framework phase in yellow dotted lines have no obvious change. (c) The STM image collected 48 hours after the deposition of C_{70}. The C_{70}/DT dimer row phase grows larger. (d) The STM image collected 72 hours after the deposition of C_{70}. Most of the C_{70} in region II have been consumed to form the C_{70}/DT dimer row phase. At the

boundary of C_{60} rich region I and C_{70} rich region II, a C_{60}-C_{70} strained layer is found in region III, where the C_{70} join the C_{60}/DT dimer framework phase in the same arrangement as the C_{60}.

Similar with our observation for the C_{70}/DT system, the molecules start to form and stabilise into some small regions of C_{70}/DT dimer row phase about 24 hours after the deposition, as highlighted in red frames in **Figure 6.3** (b). The C_{60}/DT dimer framework phases, as marked in yellow dotted lines, have no obvious change. The C_{60} and a few numbers of C_{70} remain their arrangements in this framework. While some of C_{60} at the boundaries of C_{60}/DT regions are found to diffuse into the disordered C_{70}/DT region, forming a large C_{60}-C_{70}/DT mixed domain. However, we have not observed any new structures formed in this domain. Then, when the C_{70}+C_{60}/DT/Au(111) sample is left at RT for over 48 hours after deposition of C_{70}, the C_{70}/DT dimer row phase is found grow larger gradually, as shown in **Figure 6.3** (c), and it remains relatively independent from the C_{60}/DT phase. Finally, after 72 hours of C_{70} deposition, most of C_{70} have joined the C_{70}/DT dimer row phase, as shown in **Figure 6.3** (d).

According to the coverage and arrangements of C_{60} and C_{70} in **Figure 6.3** (d), this large domain is divided into three regions. Region I, as marked in the yellow dotted line, is the C_{60} rich domain, where the C_{60} and DT arrange into their standard dimer frameworks, and there are still several bright individual C_{70} arrange within this region. Region II, as marked in the red dotted line, is the C_{70} rich domain, where most of the C_{70} and DT arrange into the dimer rows. It is also noticed that there are some dimmer molecules arrange randomly within the C_{70}/DT dimer row phase, which are likely to be the C_{60} joining in the C_{70}/DT dimer row phase, and we will further discuss about it with the height measurements of these molecules. In region III, it is interesting to notice that there is a structure resembling that of region I, but the fullerene molecules in this region show different heights, a clear indication of coexistence of C_{60} and C_{70}. The brighter molecules within this dimer framework in region III seem to have the similar heights with the individual bright molecules in region I, and it is possible that these bright molecules are the C_{70} molecules in the same specific molecular orientation. More of details will be revealed with the height measurements.

3.1.3 C_{70}-C_{60}/Decanethiol Mixture Strained Framework Phase

To identify these molecules in different brightness, we plotted height profiles of the fullerene molecules across the boundaries of each two regions. In **Figure 6.4** (a), the yellow dashed line across the region I and III corresponds to the height profile 1 in **Figure 6.4** (b), which shows the

height difference between the C_{60} and the brighter fullerene in dimer frameworks. According to profile 1, the brighter molecules in region III are 0.088 ± 0.006 nm (read from the Gwyddion) taller than C_{60} molecules in Region I. The red dashed line in **Figure 6.4** (a) across the region II and III corresponds to the height profile 2 in **Figure 6.4** (b), showing the height difference between the lying down C_{70} and the brighter fullerene. From the profile 2, we find that the brighter molecules are also taller than the lying down C_{70} molecules in region II by 0.078 ± 0.007 nm (read from the Gwyddion).

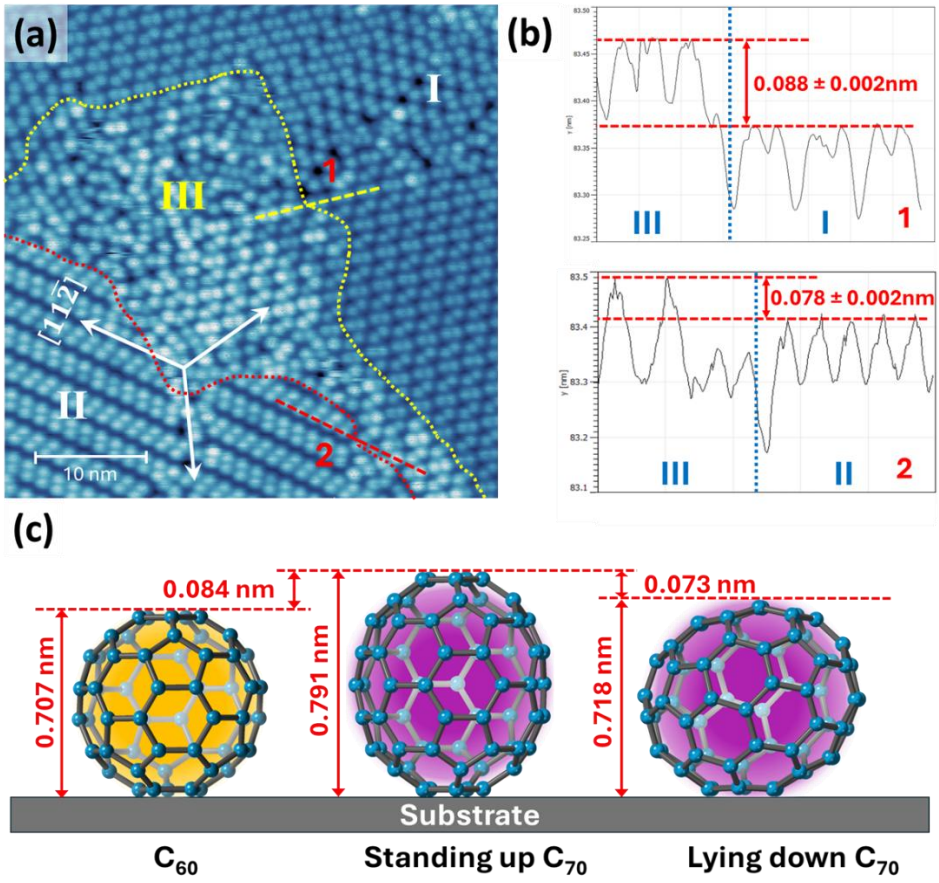

Figure 6.4 (a) The STM image showing three co-existing structures: C_{60}/DT dimer frameworks in region I; C_{70}-DT dimer rows in region II; C_{60}-C_{70}/DT dimer frameworks in region III. The boundaries of each two regions are highlighted respectively in yellow and red dotted lines. The yellow dashed line 1 cross the region I and III, and the red dashed line 2 cross the region II and III. (b) The height profiles along the dashed lines in (a). Profile 1 is taken along the yellow dashed line in (a) across region I and III boundary. Profile 2, taken along the red dashed line in (a), shows the height difference between molecules in regions II and III. (c) Schematic diagram

showing C_{60} and C_{70} and their physical dimensions[4,11] when they contact with the substrate in different ways.

Then we tried to compare these height differences with the standard parameters of C_{60} and C_{70}, and the models for C_{60} and C_{70} in both standing up and lying down orientations are shown in **Figure 6.4** (c). Here we show the side view of fullerene molecules on substrate so that their height differences are more intuitive. In **Figure 6.4** (c), the height of C_{60} is determined using single-crystal x-ray diffraction method, the height of standing up C_{70} is determined using DFT calculation, and the height of lying down C_{70} is directly read from the C_{70} model (CAS number: 115383-22-7) in Crystal Maker. Though these heights are measured in different ways, they reflect the physical atoms-to-atoms distances of a single molecule. According to these parameters of C_{60} and C_{70} molecules, the diameter of C_{60} is 0.707 nm[11], and the long axis of C_{70} is 0.791 nm[4], the theoretical height difference of C_{60} and standing up C_{70} (with their long axis perpendicular to substrate) is 0.084 nm. This standard height difference is consistent with our measured value in profile 1. The theoretic height difference of standing up C_{70} and lying down C_{70} (with their long axis almost parallel to the substrate) is 0.078 nm, which is also consistent with our measured value in profile 2. Thus, the brighter molecules in region III are identified as standing up C_{70} molecules with their long axis perpendicular to the substrate. And those individual bright molecules in region I are then deduced to be the standing up C_{70} molecules that have simply substituted C_{60} molecules within the dimer frameworks. Thus, in the mixed fullerene/DT dimer framework phase in region III, there are three types of fullerene dimers, respectively the C_{60}-C_{60} dimers, C_{70}-C_{70} dimers and C_{60}-C_{70} dimers. We then count the number of each type of fullerene dimers, and there are 25 C_{60}-C_{60} dimers, 28 C_{70}-C_{70} dimers and 35 C_{60}-C_{70} dimers in this region. In comparison to region I, region III is expected to be a strained layer due to the replacement of C_{60} with C_{70}. However, since the footprint of the standing up C_{70} is very close to that of C_{60}, the level of strain in region III is relatively low.

The area covered by this strained layer (region III) is found to be relatively limited, and we have not observed such a region where this strained layer expands as large as the pure C_{60}/DT or C_{70}/DT domains. After analysing the positions of C_{60} and C_{70} within this strained layer, we notice that the arrangements of two fullerene molecules are not even, that the local C_{60}:C_{70} ratio decreases significantly from the side closer to the region I to the other side closer to the region II, and then the region II takes over where the C_{70} molecules take a lying down orientation. After the deposition

of C_{70}, they diffuse randomly on the substrate and gradually gather at the boundaries of C_{60}/DT domains. As the sample is always kept at RT, those C_{70} and C_{60} molecules at the boundaries are both able to diffuse into the domains of other fullerene. However, due to the obstruction of surrounding DT and fullerene molecules, fewer of fullerene could diffuse far into the other domain. Finally, a region (III) of gradient C_{60}:C_{70} ratio is formed in between the C_{60}/DT (I) and C_{70}/DT (II) domains. With the concentration of C_{70} increasing, the rest of disordered C_{70} are less affected by the C_{60}/DT template, and they then form their preferred C_{70}/DT dimer row structure in region II. In semiconductor strained layer growth, the strained layers do not proceed far until stress release interrupts the growth. Here the level of strain is low, and region III is able to grow under the influence of structural inertia.

For this strained layer in our system, it is possible that if we deposit fewer C_{70} for more times onto the C_{60}/DT/Au(111) sample, this strained layer could expand larger. With fewer amounts of C_{70} added each time, the C_{60} and C_{70} at the boundaries both have more time to diffuse and mix more evenly. In addition, if we deposit C_{60} and C_{70} simultaneously onto the C_{60}/DT/Au(111) sample, this strained layer could also grow larger as the newly added C_{60} would help to maintain this C_{60}/DT framework.

3.1.4 Models for C_{70}-C_{60}/Decanethiol Mixture Strained Layer

In **Figure 6.5** (a), we show the measured details of this C_{70}-C_{60}/DT mixture strained layer. The brighter molecules in this region are the standing up C_{70}, and the rest are C_{60}. In comparison with the C_{60}/DT dimer framework structure, there is no structural change when some of the C_{60} in this region replaced by C_{70}. The α-type fullerene dimer has its dimer axis 17.0 ± 0.5° off the $[11\bar{2}]$ direction, and the distance of two fullerene molecules within the α-type fullerene dimer is 1.03 ± 0.03 nm, which is close to the shortest possible distance between them. The β-type fullerene dimer has its dimer axis parallel to the $[11\bar{2}]$ direction, and the distance of two fullerene molecules within the β-type fullerene dimer is 1.21 ± 0.02 nm. Both types of fullerene dimers are also arranged in the direction 17.0 ± 0.5° off the $[11\bar{2}]$ direction, as marked in red dashed lines. The unit cell parameters of this C_{70}-C_{60}/DT mixture strained layer are: a = 3.25 ± 0.06 nm, b = 2.40 ± 0.05 nm, γ = 70.0 ± 0.5°. It is noted that in this selected area, there are more C_{70} molecules than C_{60}. This suggests a strong effect from structural inertia which resists the formation of the C_{70}-DT-like structure. Here, the structural inertia means that the stable self-assembled

domain such as the C_{60}-DT-like structure has the ability to affect the disordered molecules at the boundary, guiding these molecules to arrange themselves in the same structure as the one that already exists. In other words, the molecules around the existing self-assembled structure will prioritize arranging themselves according to the existing structures rather than forming other structures.

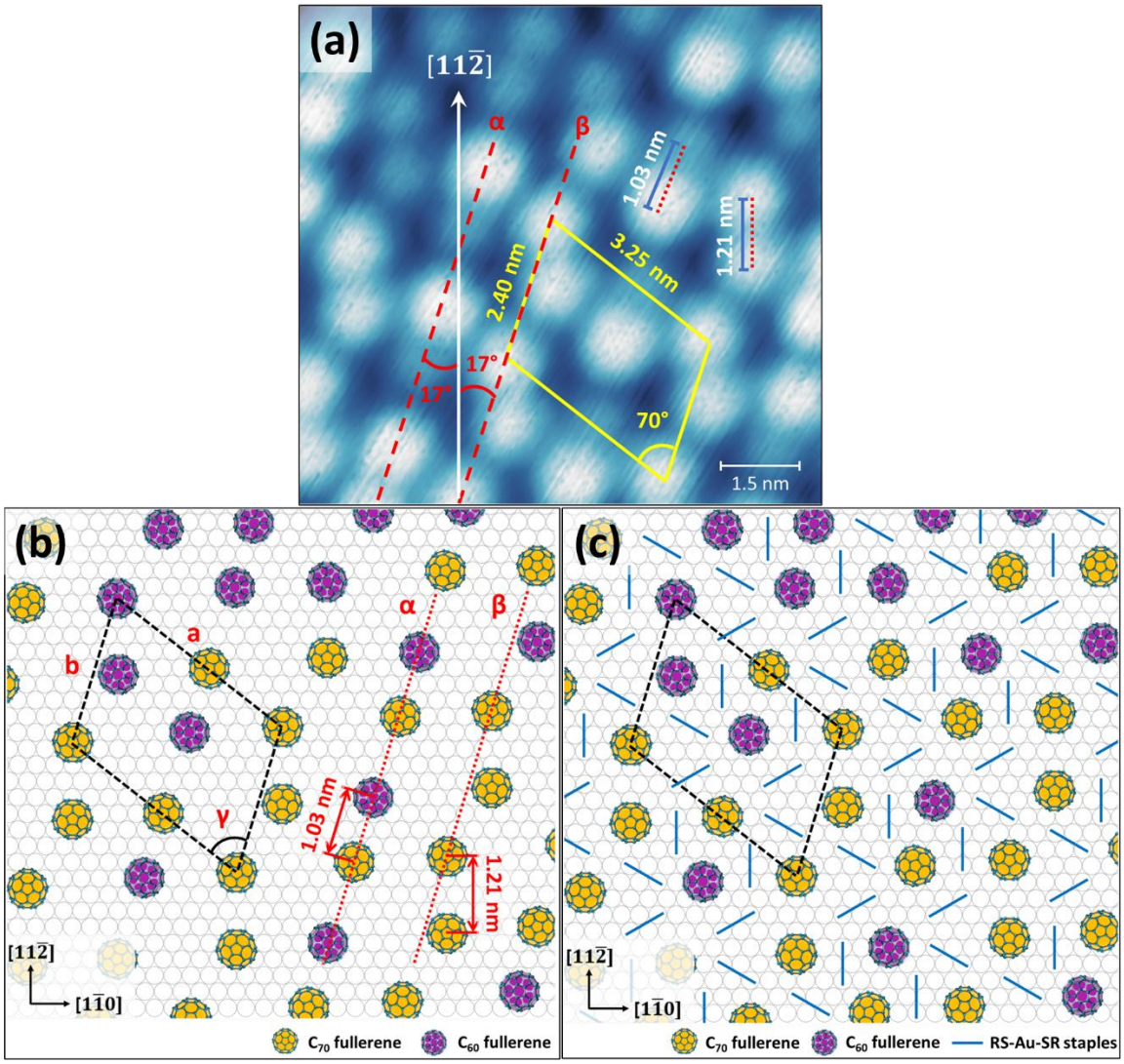

Figure 6.5 (a) The details of mixed fullerene/DT dimer framework structure. The C_{70} in this structure have a standing up orientation, and as the footprint of the standing up C_{70} is very close to that of C_{60}, there is no structural change to this framework and the parameters we measured are the same with those of C_{60}/DT dimer framework. (b) The model showing the arrangement of C_{70} and C_{60} in the corresponding region in (a). The C_{60} are filled in purple and the C_{70} are filled

in yellow. (c) The possible arrangement of RS-Au-SR staple in this region. The RS-Au-SR staples are shown in blue lines.

According to the parameters we measured and the arrangements of fullerene molecules, we place the C_{60} and C_{70} models onto the Au(111) substrate, as shown in **Figure 6.5** (b). In this model, C_{60} are filled in purple and C_{70} are filled in yellow. Since there is no difference in the arrangement of fullerene molecules in C_{60}/DT dimer framework and C_{70}-C_{60}/DT mixture strained layer, we replace some of C_{60} into standing up C_{70} according to **Figure 6.5** (a) without changing their binding positions. Fullerene molecules in α-type dimers occupy the bridge sites of the Au(111) substrate, and the fullerene in β-type dimers occupy the three-fold hollow sites. The coverage of fullerene molecules in this mixed framework is 0.044 ML. DT molecules, shown as units of RS-Au-SR staples in short blue bars, are then placed into the gaps of the dimer framework. Each two DT molecules form a RS-Au-SR staple with a gold adatom which occupies the bridge site of Au(111)[12]. The coverage of DT molecules in this framework is 0.133 ML. In one unit cell of this fullerene/DT dimer framework, there are four fullerene molecules and eight DT molecules, and the C_{60}/C_{70}-DT ratio is thus 1:3. The model also shows the concentration change of C_{60} and C_{70} more clearly. The top half of this model has higher concentration of C_{60}, corresponding to the area closer to a C_{60} rich region. The bottom half corresponds to the area closer to a C_{70} rich region. And that the local C_{60}:C_{70} ratio reduced from the top half region to the bottom half region.

3.2 Au(111)-Decanethiol-C_{70} + C_{60}

After we notice that interesting low strained layer shown in between two different fullerene/DT self-assembled phases, it comes to our mind that C_{70} could also have the ability to guide C_{60} to form into a mixed fullerene strained layer. Hence, we come up with a plan for the subsequent experiment, where we change the deposition order of the C_{60} and C_{70} molecules while keeping all other conditions the same as before. According to our discussion in the previous chapter, C_{70}/DT system on Au(111) substrate shows two distinct self-assembled phases, respectively dimer row phase and porous framework phase. In each phase, C_{70} molecules bind to the Au(111) substrate at specific sites in specific molecular orientations. As we mentioned, C_{60} molecules have a higher symmetry than C_{70}, which allows them to bind to the Au(111) substrate in more ways. Therefore, we initially speculate that it would be easier for C_{60} to join the C_{70}/DT self-assembled structures,

as they are more likely to find the proper binding sites and orientation required within the ordered phase.

3.2.1 Comparison of C_{60}/Decanethiol Dimer Rows and C_{70}/Decanethiol Dimer Rows

The C_{60}, as we introduced in **Figure 6.2** (a), form various dimer frameworks with the participation of DT on Au(111) substrate. In addition, the C_{60} dimers also have the probability to form a dimer row phase, as reported in previous works[13]. Here, in some regions of pure C_{60}/DT on this sample, we observe that the C_{60} form into such a dimer row phase, as shown in **Figure 6.6** (a). The regions of C_{60}/DT dimer row phase are marked in yellow dashed frames. The C_{60} dimer rows grow in the direction of 90.2 ± 0.4° off the $[11\bar{2}]$ direction, which is close to the $[1\bar{1}0]$ direction of Au(111) substrate. The C_{60} dimers within these dimer rows have their dimer axes 17.0 ± 0.5° off the $[11\bar{2}]$ direction, which is the same direction as the α-type C_{60} dimers in C_{60}/DT dimer framework phase.

In comparison, an STM image of C_{70}/DT dimer row phase is shown in **Figure 6.6** (b). The C_{70}/DT dimer row, as we discussed in Chapter IV, grows along the $[11\bar{2}]$ direction of Au(111) substrate, which is strongly related to the arrangement of DT molecules in δ phase. And for the C_{70} dimers, there are two different dimer axes, respectively.

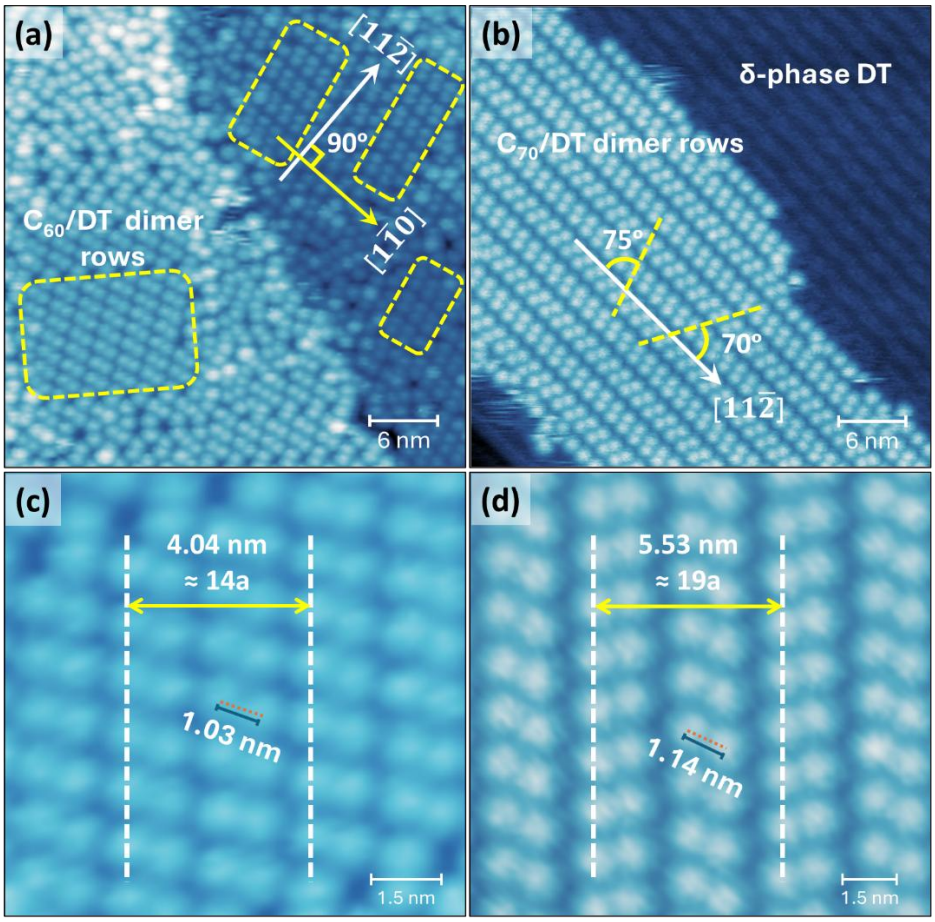

Figure 6.6 (a) The regions marked in yellow frames show the C_{60}/DT dimer row structure on Au(111) substrate. The C_{60} dimer rows have the direction 90.2 ± 0.4° off the [11$\bar{2}$] direction. (b) The C_{70}/DT dimer row structure on Au(111) substrate. The C_{70}/DT dimer rows grow along the [11$\bar{2}$] direction. (c) The details of the C_{60}/DT dimer row structure. The distance between each three dimer rows is 4.04 ± 0.03 nm, and the distance of two molecules in each C_{60} dimer is 1.03 ± 0.02 nm. The C_{60} dimers within the dimer rows have the same dimer axes, which are in the direction of 17.0 ± 0.5° off the [11$\bar{2}$] direction. (d) The details of C_{70}/DT dimer row structure. The distance between each two repeating dimer rows is 5.53 ± 0.03 nm, and the distance of two molecules in each C_{70} dimer is 1.14 ± 0.02 nm. The C_{70} dimers within the dimer rows have two different dimer axes, respectively in the direction of 70.0 ± 0.9° (clockwise) off the [11$\bar{2}$] direction and 75.0 ± 0.8° (counterclockwise) off the [11$\bar{2}$] direction.

More details of two fullerene/DT dimer row structures are shown in **Figure 6.6** (c) and (d). For a more intuitive comparison with the distance in C_{70}/DT dimer row structure, we measure the

distance of three repeating C_{60}/DT dimer rows in the direction perpendicular to the dimer rows. This distance is measured to be 4.04 ± 0.03 nm (≈ 14a), which is about 5a shorter than the distance between two repeating C_{70}/DT dimer rows (≈ 19a). The distance of the C_{60} within the dimers is 1.03 ± 0.02 nm, and it is the same with that distance of α-type C_{60} dimers in framework structure. The distance of the C_{70} within the dimers, due to their lying down orientation on Au(111) substrate, is slightly larger than the C_{60} dimers.

Comparing the arrangements of fullerene molecules in two dimer row phases, the arrangement of C_{60} seems to be more regular than that of C_{70}, which indicates that the arrangement of C_{60} is commensurate with the Au(111) substrate. With each of the C_{60} dimer occupying the equivalent binding sites, all the C_{60} dimers could keep the same dimer axes and distances. While for C_{70} dimers, their arrangements are obviously affected by the ellipsoid-like shape of C_{70} molecule. When C_{70} molecule standing up with its long axis perpendicular to the Au(111) substrate, its footprint is very close to that of C_{60}, so that C_{70} in this molecular orientation could have the similar ordered arrangement with C_{60}, as we discussed in **Figure 6.4**. However, C_{70} are less stable when they bind to the substrate in this orientation[10], and they are likely to lying down if there is no additional strain. Thus, on the pure C_{70}/DT/Au(111) sample, C_{70} form dimers in a lying down orientation, which results in a larger footprint for each C_{70} dimer. Meanwhile, with the participation of DT, C_{70} dimer have to keep a proper distance with the DT alkane chains. Eventually, due to these various restrictions, half of the C_{70} dimers have to change their axes to maintain the whole domains. Though each neighbouring C_{70} dimer row has the same spacing, the C_{70} dimers within are unable to occupy the equivalent binding sites of Au(111) substrate, otherwise the whole structure would be broken. And that makes the arrangement of C_{70} in dimer row phase less compatible with the Au(111) substrate. Having clarified this distinction between C_{70}/DT dimer row structure and C_{60}/DT dimer row structure, it will be easier for us to proceed with our analysis for mixed fullerene/DT dimer row structure later.

3.2.2 Phase Changing after C_{60} Added to C_{70}/Decanethiol/Au(111) Sample

Similar with the first sample, we need to prepare the pure C_{70}/DT/Au(111) sample and wait for the ordered C_{70}/DT structure to form before adding the C_{60}. After the deposition of C_{70} on the δ-phase DT/Au(111) surface, the sample was left at RT for 72 hours during which time large areas of C_{70}/DT dimer rows formed. The final structure we observed from C_{70}/DT/Au(111) sample is

similar to the region shown in **Figure 4.2** (a), and we will not show it in this part. After most of the C_{70} formed into ordered phase, the C_{60} were then deposited onto the C_{70}/DT/Au(111) sample for 10 minutes (deposition temperature: 410 °C), and the STM images were collected in different periods after the deposition. **Figure 6.7** (a) shows the image of C_{60}+C_{70}/DT/Au(111) sample collected within 24 hours after the deposition of C_{60}. It is noticed that in some of the regions, C_{70} molecules remain in the C_{70}/DT dimer row structure and porous framework structure, and there are also some regions of disordered fullerene appearing after the deposition, which are deduced to be disordered C_{60} or mixture of C_{60} and C_{70}.

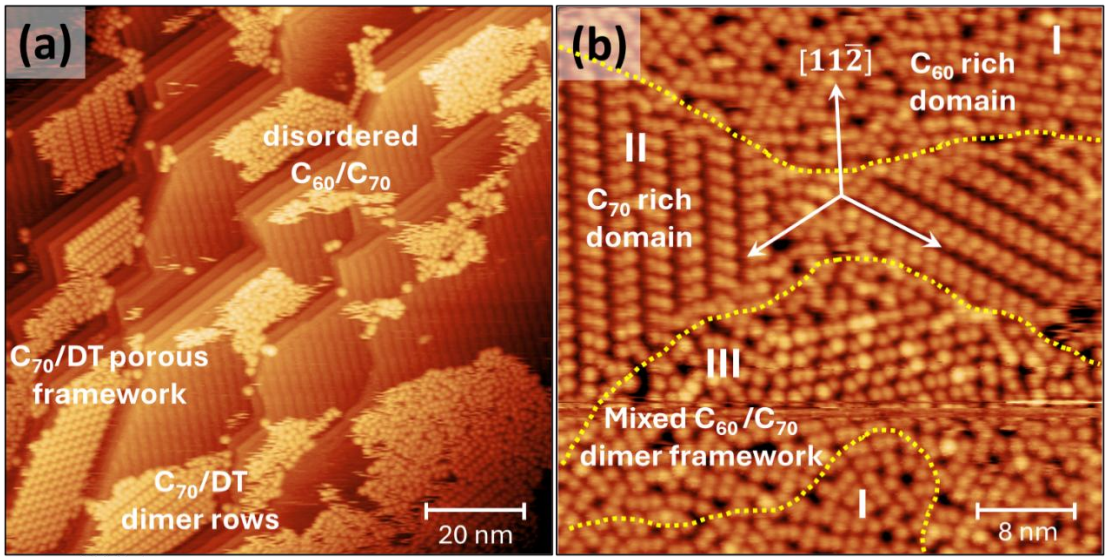

Figure 6.7 (a) The STM image of C_{60}+C_{70}/DT/Au(111) sample collected within 24 hours after the deposition of C_{60}. (b) The STM image collected over 72 hours after the deposition of C_{60}. Most of the C_{60} within the C_{60} rich domains form into dimers, as marked region I. The C_{70} in region II remain in the dimer row structure. And in region III, both two fullerene molecules are found arrange into C_{70}-C_{60}/DT mixture strained framework.

Then, same with the process for the first sample, we left the C_{60}+C_{70}/DT/Au(111) sample at RT for 72 hours. During this time, C_{60} appear to gradually form into their preferred C_{60} dimers, as shown in the region I in **Figure 6.7** (b). In region II, the fullerenes are in the arrangement of C_{70}/DT dimer row structure, which indicates that this is a C_{70} rich domain. Then in region III, we observed the similar C_{70}-C_{60}/DT mixture strained framework as we introduced in **Figure 6.4**. The dimmer (lower) molecules within this framework are C_{60}, and the brighter (higher) molecules are standing

up C_{70}. After the deposition, C_{60} diffuse randomly on the C_{70}/DT/Au(111) substrate, and gradually gather at the boundaries of C_{70}/DT domains. Meanwhile, some of the C_{70} at the boundaries diffuse out into the C_{60}/DT domains, and then form into the C_{70}-C_{60}/DT mixture strained framework structure with the guidance of the C_{60}/DT structural inertia.

In addition to these similar features we observed from the C_{70}+C_{60}/DT/Au(111) sample, we have found two types of distinct fullerene/DT dimer row structures on this C_{60}+C_{70}/DT/Au(111) sample, as shown in **Figure 6.8** (a) and (b). The arrangements of fullerene within these two dimer row structures marked in yellow dotted frames are rather similar to that within the normal C_{70}/DT dimer row structure. And the most notable difference is that all the three dimer rows consist of the fullerene dimers in the same dimer axes, either in the direction of 70.0 ± 0.6° (**Figure 6.8** (a)) or 75.0 ± 0.5° (**Figure 6.8** (b)) off the $[11\bar{2}]$ direction. The normal C_{70}/DT dimer row phase consists of C_{70} dimers in two directions, and each two neighbouring dimer rows have their dimer axes keeping an angle of 70.0 ± 0.9° (clockwise) and 75.2 ± 0.8° (counterclockwise) off the $[11\bar{2}]$ direction respectively. We then measured the distance of these three dimer rows. Comparing it with the distance of two repeating C_{70}/DT dimer rows, there is no difference in the spacing between these two structures, which indicates that the formation of this distinct dimer row is strongly affected by the C_{70}/DT structural inertia. According to the features we observed, we can deduce that the C_{60} participate in this fullerene/DT dimer row structure, however, we still need more information to distinguish these fullerenes.

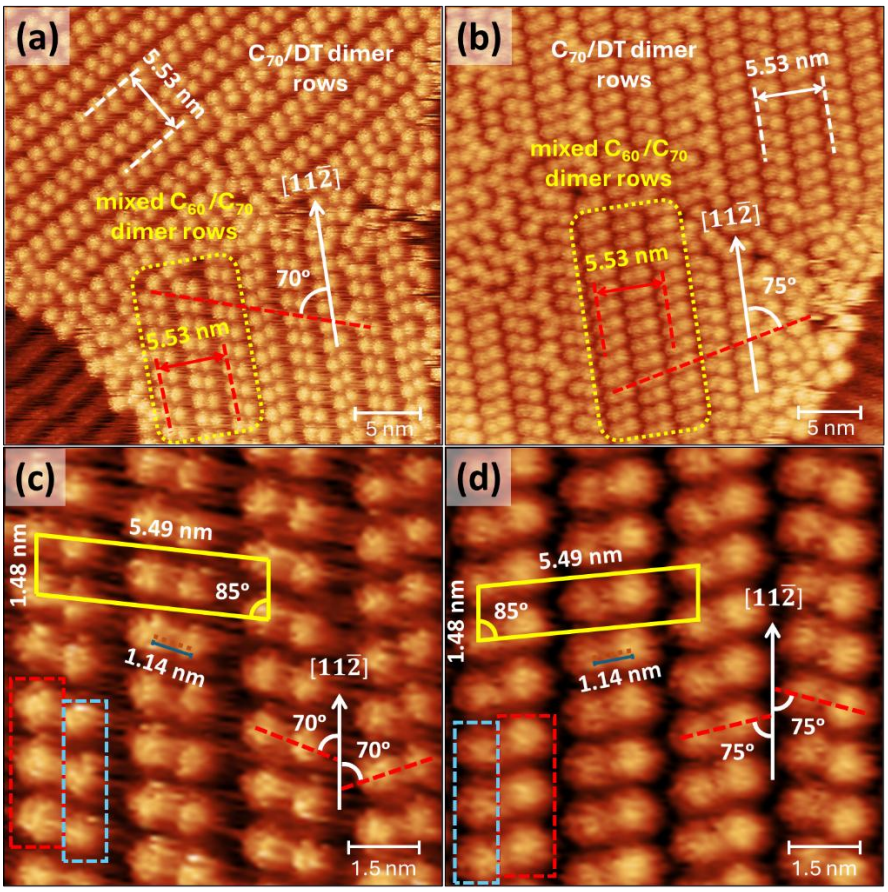

Figure 6.8 (a) The observation of the fullerene/DT dimer rows with the same dimer axes, marked in yellow frame. The dimer axes of these three dimer rows are in the direction of 70.0 ± 0.6° (counterclockwise) off the [11$\bar{2}$] direction. The distance of three mixed fullerene/DT dimer rows is 5.53 ± 0.05 nm, which is the same as the distance of two repeating C_{70}/DT dimer rows. (b) The other type of fullerene/DT dimer rows, of which the dimer axes are in the direction of 75.0 ± 0.5° (clockwise) off the [11$\bar{2}$] direction. (c) The measured details of type 1 mixed fullerene/DT dimer row structure. The fullerenes within these dimer rows are found slightly different in size and brightness, that the fullerenes highlighted in red dashed frame look slightly larger and brighter than the fullerenes highlighted in blue dashed frame from STM image. (d) The measured details of type 2 mixed fullerene/DT dimer row structure. The fullerenes highlighted in red frame also look larger and brighter.

More details of mixed fullerene/DT dimer row structure are revealed in **Figure 6.8** (c) and (d). For the convenience of subsequent descriptions, we name the mixed fullerene/DT dimer row with dimer axes in the direction of 70.0 ± 0.6° (counterclockwise) off the [11$\bar{2}$] direction as type 1

dimer row structure, and the dimer row with dimer axes in the direction of 75.0 ± 0.5° (clockwise) off the $[11\bar{2}]$ direction as type 2 dimer row structure. In **Figure 6.8** (c), the fullerene dimers next to the type 1 dimer rows are found have their dimer axes in the angle of 70.0 ± 0.6° (clockwise) off the $[11\bar{2}]$ direction, which is the same with the angle of type 1 fullerene dimer axes but in different directions. The distance of two fullerene within the type 1 dimers is 1.14 ± 0.02 nm, and it is also the same with that of normal C_{70} dimers. The unit cell of type 1 dimer row structure is marked in yellow parallelogram, and the parameters are: a = 1.48 ± 0.03 nm, b = 5.49 ± 0.05 nm, γ = 85.0 ± 0.5°. In **Figure 6.8** (d), the type 2 dimer rows show the similar features to those of type 1 dimer rows. The angle of type 2 dimer axes is also the same with the neighbouring fullerene/DT dimer row, which is 75.0 ± 0.5° (clockwise) off the $[11\bar{2}]$ direction. The distance of two fullerene within the type 2 dimers is 1.14 ± 0.02 nm. And the unit cell of type 2 dimer row structure is highlight in yellow, of which the unit cell parameters are same with the type 1 dimer structure.

However, even we have collected enough details of these two C_{60}-C_{70}/DT dimer row structures, it is still a challenging to identify the C_{60} from all the fullerenes. After careful comparison, we notice that some of the fullerene molecules are different in size and brightness, as highlighted in the red and blue dashed frames in **Figure 6.8** (c) and (d). The fullerenes in red frame are found slightly larger and brighter than the fullerenes in blue frame. According to the schematic diagram showing the physical dimensions of C_{60} and C_{70} in **Figure 6.4** (c), there is a tiny height difference of 0.011 nm between C_{60} and lying down C_{70}. With a higher physical height, C_{70} will look brighter than C_{60} from STM images. In addition, the C_{70} in lying down orientation has its long axis almost parallel to the Au(111) substrate, as its long axis is about 0.084 nm longer than the diameter of the C_{60}, the lying down C_{70} will also look larger than C_{60} from STM images. Hence, we deduced that the larger and brighter fullerenes within these dimer rows as highlighted in red frames are lying down C_{70} molecules, and the fullerenes highlighted in blue frames are C_{60} molecules.

To prove our assumption, we then measured the height across the fullerenes within the type 1 and type 2 C_{60}-C_{70}/DT dimer rows, and the height profiles are shown in **Figure 6.9**. In **Figure 6.9** (a), the profile on the right corresponds to the height of fullerene dimers highlighted in yellow dashed line. Within each type 2 fullerene dimer, the fullerene in the row marked in blue dotted frame is smaller than the fullerene in the row marked in red dotted frame, and their height differences are shown on the right. For these three selected fullerene dimers, the height differences of two

fullerenes vary from 0.012 nm to 0.058 nm, which indicates that the C_{70} within the C_{60}-C_{70}/DT dimer rows are not as stable as the C_{70} within the pure C_{70}/DT dimer rows. We then measured the heights of all the fullerene dimers within the C_{60}-C_{70}/DT dimer rows. The maximum height difference of two fullerene within a dimer is 0.072 nm, and the minimum height difference is 0.011 nm. As the pure C_{70} dimers have not been found have such a height difference between two C_{70} molecules, we have now determined that each C_{60}-C_{70}/DT dimer row consists of one single row of C_{60} (in blue dotted frames) and one single row of C_{70} (in red dotted frames).

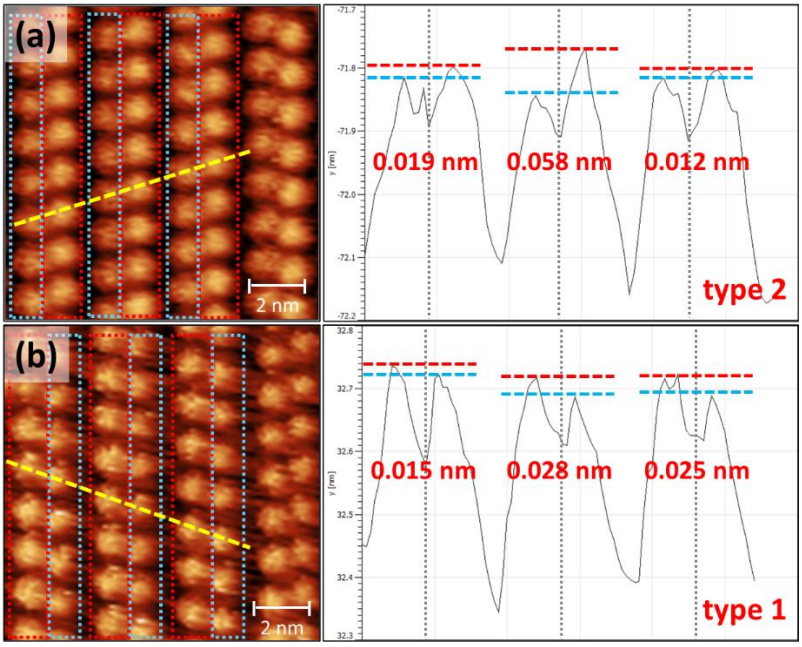

Figure 6.9 (a) The height profile showing the height difference between the fullerenes within the type 2 C_{60}-C_{70}/DT dimer row structure. The fullerenes with different size and brightness are respectively highlighted in red and blue dotted frames. The height differences of fullerenes within each selected fullerene dimers are shown on the right. (b) The height profile showing the height difference between the fullerenes within the type 1 C_{60}-C_{70}/DT dimer row structure. The height differences of selected fullerenes are shown on the right.

The same measurements are conducted to the type 1 C_{60}-C_{70}/DT dimer rows, and the results are shown in **Figure 6.9** (b). In this region, the fullerenes within the C_{60}-C_{70}/DT dimer row show the similar features, that the row of fullerenes marked in red dotted frames appear larger and brighter than the row of fullerenes marked in blue dotted frames. The height profile on the right shows the height differences of three C_{60}-C_{70} dimers. Comparing those with the type 1 C_{60}-C_{70} dimers, the

height differences of type 1 C_{60}-C_{70} dimers are relatively more even. After the complete measurement of all the type 1 dimers, the maximum height difference is found to be 0.053 nm, and the minimum height difference is 0.012 nm. It indicates that the occupations of C_{70} within the type 1 dimers are more regular than those of type 2 dimers.

According to our measurements above, the height differences of C_{60} and C_{70} measured from all the C_{60}-C_{70} dimers vary a lot, and the possible explanation is that the molecular orientation of C_{70} is affected by the C_{60} which forms a dimer with it. Due to the high symmetry of C_{60}, each C_{60} molecule can bind to substrate in various orientations[14,15]. In addition, the fullerene molecules will not form into dimers randomly. They prefer to form dimers with one of their hexagonal rings facing each other[16]. Thus, the C_{70} have to adjust their molecular orientations to meet the requirements of fullerene dimerization, which leads to various heights of C_{70} within the C_{60}-C_{70}/DT dimer rows. Unfortunately, we have not observed the molecular orientations of these fullerenes as the scanning of the sample in this experiment is conducted at RT. And the LT scanning could provide us with more useful information. In addition, as the theoretical height difference of C_{60} and lying down C_{70} is close to the resolution limit of STM in *z* direction (0.01 nm), the results could be strongly affected by the errors during scanning. And it would be better to use other techniques or methods to distinguish between C_{60} and C_{70} molecules, such as scanning tunnelling spectroscopy (STS).

For these mixed C_{60}-C_{70}/DT dimer rows, it is interesting to notice that both type 1 and type 2 dimer rows could only remain in the same direction for three rows, and we have not found a large domain formed with the pure type 1 or type 2 dimer rows. With one of the C_{70} replaced by C_{60} within each fullerene dimer, there is relatively more space left for DT alkane chains. Meanwhile, the interaction between fullerene and DT alkane chains is also changed due to the change in the dimer axes of one of the fullerene dimer rows. As there is no direct observation of DT molecules within the mixed C_{60}-C_{70}/DT dimer rows at RT, we will discuss this later with the theoretic models.

3.2.3 Possible Models for Mixed C_{60}-C_{70}/Decanethiol Dimer Row Structures

To further understand the arrangements of fullerenes and DT molecules in the mixed C_{60}-C_{70}/DT dimer row structures on Au(111) substrate, we try to build the models with the information we have acquired. However, as we discussed, there is some uncertainty about the arrangements of C_{60} and C_{70} within the mixed dimer rows. Due to the lack of resolution, we cannot tell if a dimer is C_{60}-C_{70}, C_{70}-C_{70} or C_{60}-C_{60}. Though we have found some evidence showing that the mixed

fullerene dimers consist of one C_{60} and one C_{70}, without more straightforward data to further prove that, we still decided to consider about all the possible formations of mixed fullerene dimers in the models.

Firstly, we try to replace all the C_{70} in the dimer rows with the C_{60} molecules, and the models for arrangements of fullerenes in type 1 and 2 mixed dimer row structures are shown in **Figure 6.10**. **Figure 6.10** (a) shows the arrangement of C_{60} in type 1 dimer rows, and the C_{60} are filled in yellow. In this model, all the C_{60} occupy the three-fold hollow sites of Au(111) substrate with one of their pentagonal rings in contact with the substrate. Though those C_{60} in this arrangement are well compatible with the binding sites of the Au(111) substrate, the distance of two C_{60} within each dimer is relatively too large, which is about 10.7% larger than the distance of two normal dimerized C_{60}. With larger gaps left in between the C_{60} dimers, it requires more DT molecules to fill into the gaps and stabilise the whole structure. The local coverage of C_{60} in this dimer row structure is 0.041 ML, which is slightly lower than that of the C_{60}/DT dimer framework phase (0.044 ML) shown in **Figure 6.2** (b). The arrangement of C_{60} in type 2 dimer row structure is shown in **Figure 6.10** (b). In comparison with the arrangement of C_{60} in type 1 dimer row, there is no obvious difference except for the directions of C_{60} dimer axes, which is 75.0 ± 0.5° (clockwise) off the $[11\bar{2}]$ direction. The C_{60} occupy the three-fold hollow sites of Au(111) substrate, and the local coverage of C_{60} is 0.041 ML as well.

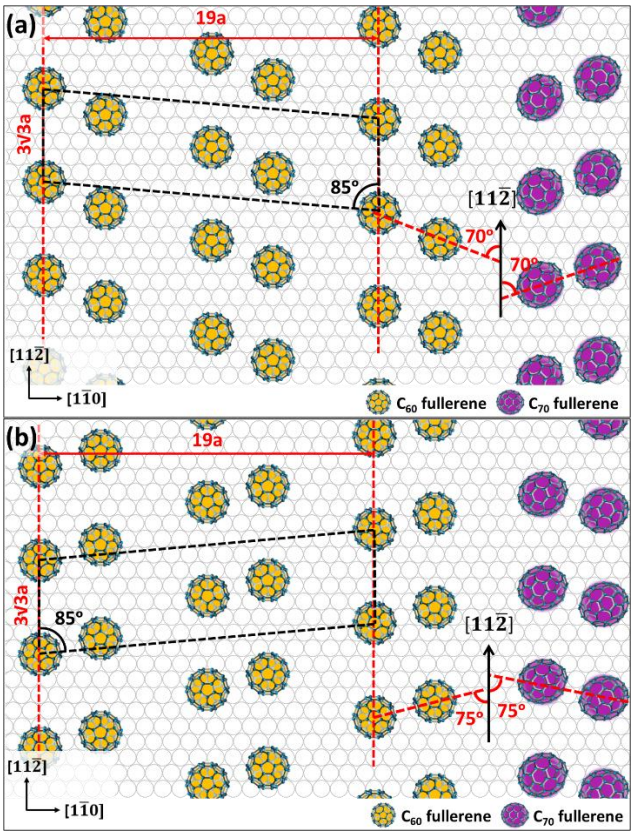

Figure 6.10 (a) Possible arrangement of fullerenes in type 1 dimer row structure when all the C_{70} in these three rows are replaced with C_{60}. The C_{60} , filled in yellow, occupy the three-fold hollow sites of the Au(111) substrate. And the dimer axes of all the C_{60} dimers are in the direction of $70.0 \pm 0.6°$ (clockwise) off the $[11\bar{2}]$ direction. The distance of C_{60} within each dimer is 1.14 ± 0.02 nm, and the distance of two neighbouring C_{60} dimer rows is 8.5a. (b) Possible arrangement of fullerenes in type 2 dimer row structure. The C_{60} occupy the three-fold hollow sites of the Au(111) substrate. The distances of C_{60} in the type 2 dimer row structure are the same with the type 1 dimer row structure, and the only difference is that the direction of C_{60} dimers are $75.0 \pm 0.5°$ (clockwise) off the $[11\bar{2}]$ direction.

Then we consider about the other possibility, that the C_{70} within the type 1 and 2 dimer rows are partially replaced by C_{60}. According to our discussion in **Figure 6.9**, that each C_{60}-C_{70} mixed dimer row contains one row of C_{60} and one row of C_{70}, we then place the C_{60} and C_{70} models onto the corresponding positions on Au(111) substrate. For the C_{70} molecules in type 1 and 2 dimer rows, as we mentioned, are found to have the different heights in different C_{60}-C_{70} dimers, which indicates that these C_{70} have different molecular orientations on Au(111) substrate. However, we

have no clear indications about the exact molecular orientation of C_{70}, thus we use the same lying down orientation for these C_{70} in this model. And the final arrangement of C_{60}-C_{70} dimers is shown in **Figure 6.11**.

Figure 6.11 (a) shows the arrangement of C_{60}-C_{70} dimers in type 1 mixed dimer row structure. In this model, C_{60} are filled in yellow, occupying the bridge sites of Au(111) substrate, and C_{70} are filled in purple, occupying the three-fold hollow sites of Au(111) substrate. The C_{60}-C_{70} dimers have their dimer axes in the direction of 70.0 ± 0.6° (clockwise) off the $[11\bar{2}]$ direction. The distance of the neighbouring C_{60}-C_{70} dimers along $[11\bar{2}]$ direction is 1.48 ± 0.03 nm (≈ 3√3a), and the distance of two neighbouring C_{60}-C_{70} dimer rows is 8.5a. The C_{60} and C_{70} form into dimers with one of their hexagonal rings facing each other. The local coverage of fullerenes is 0.041 ML, and the C_{60}-C_{70} ratio is 1:1.

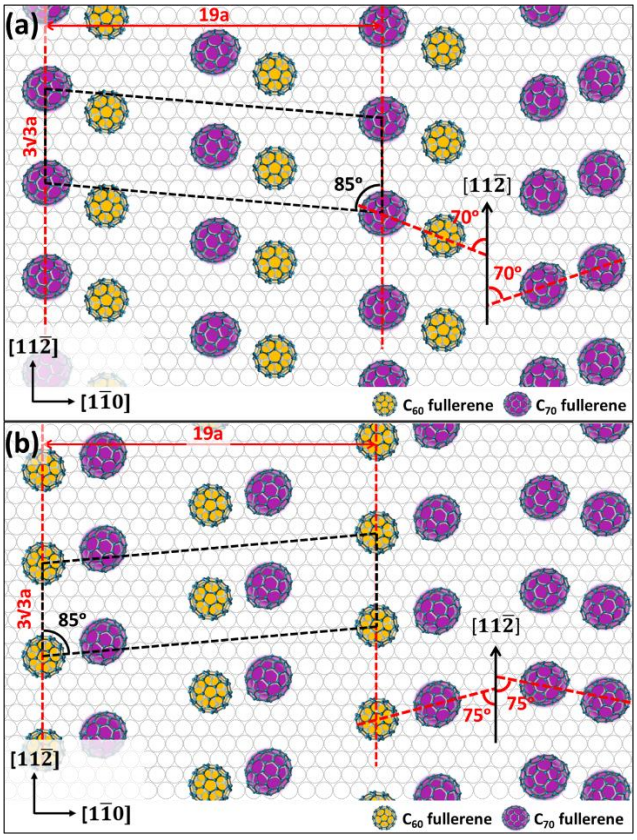

Figure 6.11 The arrangement of fullerene in type 1 and 2 dimer row structures when one row of C_{70} is replaced by C_{60}. The C_{60} are filled in yellow and the C_{70} are filled in purple. There are two C_{60} molecules and two C_{70} molecules within each unit cell. (a) The type 1 fullerene/DT dimer

row formed with C_{60}-C_{70} dimers. (b) The type 2 fullerene/DT dimer row formed with C_{60}-C_{70} dimers.

Figure 6.11 (b) shows the arrangement of C_{60}-C_{70} dimers in type 2 mixed dimer row structure. According to **Figure 6.9** (a), the left row of C_{70} molecules are replaced by C_{60}. The C_{60} and C_{70} molecules in this arrangement both occupy the three-fold hollow sites of Au(111) substrate. These C_{60}-C_{70} dimers have their dimer axes in the direction of 75.0 ± 0.5° (clockwise) off the $[11\bar{2}]$ direction. And the distances of fullerenes are the same with those of type 1 dimer row structure.

After careful analysis, the arrangement of fullerenes in **Figure 6.11** seems to be reasonable. As we observed in **Figure 6.3** (d), there are also some dimmer C_{60} which replacing the C_{70} and joining the C_{70}/DT dimer row structure. These C_{60} seem to be randomly arranged within the C_{70}/DT dimer row domain, and the overall C_{70}/DT dimer row structure is not affected. However, in the regions in **Figure 6.9**, the height profile shows that a whole row of C_{70} are replaced by C_{60}. It is possible that when the C_{60} regularly arranged into the C_{70}/DT dimer row phase, the overall structural features will change, which appears in the mixed dimer row structure as a change in the direction of dimer axes. While when C_{70} within the C_{70}/DT dimer row phase are randomly replaced by C_{60}, the tiny gaps around C_{60} could be easily filled by the DT alkane chains, and the neighbouring fullerenes of C_{60} would still be held at their positions. Though the stability of this fullerene/DT dimer row phase could be different, its structural features will still be under the influence of C_{70}/DT structural inertia. The distance of C_{60} and C_{70} within each dimer in this arrangement also seems to be more reasonable. Though the centre-to-centre distance of fullerenes is still 1.14 ± 0.02 nm, with the C_{70} in a lying down orientation on Au(111) substrate, the distance between the two fullerenes can be kept in a proper range[17], which enhances the stability of the overall structure.

Then we tried to place the RS-Au-SR staples into the gaps, and the possible arrangement of DT molecules in both types of fullerene dimer row structures are shown in **Figure 6.12**. In **Figure 6.12** (a) and (b), we show the arrangement of DT within the type 1 and type 2 fullerene dimer rows form by pure C_{60}. The RS-Au-SR staples are evenly placed with the Au adatoms in the middle occupying the bridge sites of Au(111) substrate. There are four C_{60} molecules and twelve DT molecules in each unit cell marked in dashed frame, and the local coverages of C_{60} and DT are respectively 0.041 ML and 0.122 ML, which are the same with the local coverage of C_{70} and DT in C_{70}/DT dimer row structure. However, the coverage of DT molecules is lower than we expected.

As we mentioned in **Figure 6.10**, the distance of two C_{60} within each dimer is relatively too large, which requires more DT molecules filled in the gaps to stabilise the C_{60}. We have tried to place more RS-Au-SR staples into the gaps in many different ways to more effectively occupy the space (also ensure that the distance between each molecule is greater than the van der Waals radii), but it is hard to arrange them evenly within the C_{60} dimer rows. Thus, the type 1 and type 2 fullerene/DT dimer row structure in the arrangement of both molecules in **Figure 6.12** (a) and (b) are considered to be less stable than the C_{70}/DT dimer row structure. Since we notice that this fullerene/DT dimer row structure could maintain for at most three rows, this may be caused by the lower structural stability, and we still consider this to be one of the possible arrangements.

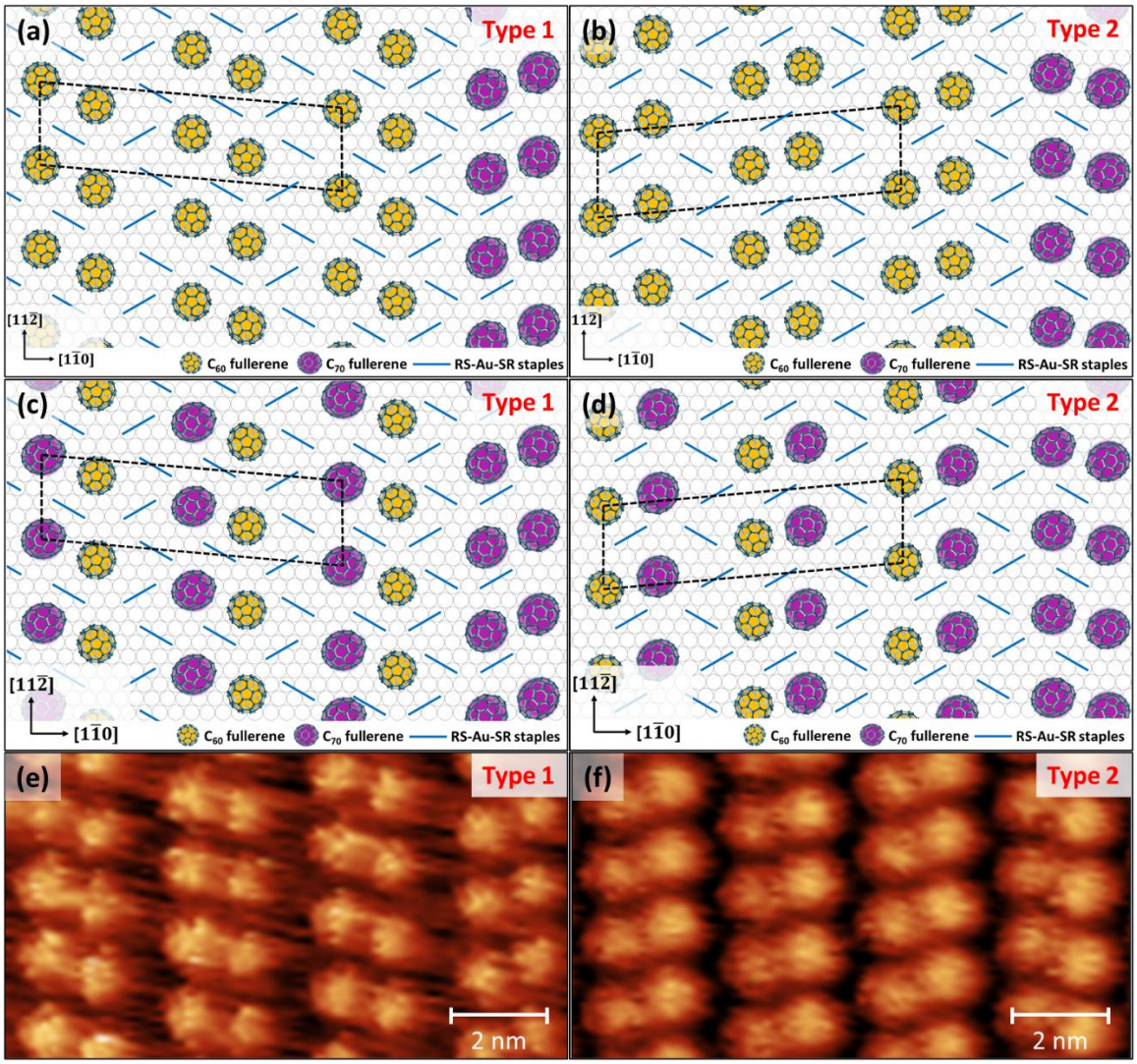

Figure 6.12 The possible arrangement of RS-Au-SR staples within the type 1 and type 2 dimer row structures. (a) The model for the type 1 C_{60}/DT dimer row structure. (b) The model for the

type 2 C_{60}/DT dimer row structure. (c) The model for the type 1 C_{60}-C_{70}/DT dimer row structure. (d) The model for the type 2 C_{60}-C_{70}/DT dimer row structure. (e) The STM image of type 1 fullerene/DT dimer row structure for direct comparison. (f) The STM image of type 2 fullerene/DT dimer row structure for direct comparison.

In **Figure 6.12** (c) and (d), we show the possible arrangement of DT within the type 1 and type 2 fullerene dimer rows form by C_{60}-C_{70} dimers. In comparison with the models in **Figure 6.12** (a) and (b), there is no difference in the arrangement of RS-Au-SR staples, that there are also twelve DT molecules in each unit cell. While with the larger size of C_{70} molecules, the DT alkane chains could have stronger interactions with C_{70}, which will help to stabilise the C_{60}-C_{70} dimer row structure more effectively. The local coverage of fullerene molecules is 0.041 ML, with C_{60} and C_{70} molecules accounting for half each. And the local coverage of DT is 0.122 ML. The parameters of unit cell are: $a = 1.48 \pm 0.03$ nm, $b = 5.54 \pm 0.05$ nm, $\gamma = 85.0 \pm 0.5°$.

Compared with the C_{70}/DT dimer row structure, these mixed C_{60}-C_{70}/DT dimer rows are likely to be less stable, as they only maintain for at most three rows. Different from the C_{70} within the C_{60}/DT dimer framework structure, that the C_{70} could only join the framework in one specific molecular orientation, the C_{60} within this C_{60}-C_{70}/DT dimer row structure are still mobile at their position, which allows the C_{60} binding on the substrate with various of molecular orientations. Though the C_{60} occupy the equivalent binding sites of Au(111) substrate, with different molecular orientations, their binding energies vary, and this will further affect the molecular orientations of C_{70}, as we discussed in **Figure 6.9**. Thus, this may have led to the relatively low stability of this mixed C_{60}-C_{70}/DT dimer row structure.

3.3 Mixed Structure after Thermal Annealing

From the C_{70}+C_{60}/DT/Au(111) sample and the C_{60}+C_{70}/DT/Au(111) sample, we have observed several interesting fullerene/DT mixed self-assembled structures, and both C_{60} and C_{70} seem to be able to participate in the formation of the structure of other fullerene molecules. However, due to the slow and limited diffusion of both fullerenes at RT, C_{60} and C_{70} are unable to mix well. Thus in most of regions, these two fullerenes still maintain their respective self-assembled structures. Since we have collected enough information about the mixed C_{60}-C_{70}/DT structures at RT, we then plan to anneal the sample to accelerate the diffusions of both molecules, seeing what kind of self-

assembled structure will form on δ phase DT/Au(111) sample when the C_{60} and C_{70} are thoroughly mixed.

The C_{70}+C_{60}/DT/Au(111) sample is annealed at 70 °C for 1 hour, during which the vacuum of preparation chamber is kept under 1.0×10^{-8} mbar. The annealed C_{70}+C_{60}/DT/Au(111) sample is cooled down to RT before transferred back to the STM. The scanning of this sample is conducted at RT, and the vacuum is kept under 1.0×10^{-10} mbar during scanning.

3.3.1 Structural Features of C_{70}+C_{60}/Decanethiol/Au(111) Sample after Thermal Annealing

After the annealing, the C_{70}+C_{60}/DT/Au(111) sample was immediately transferred into the STM when the sample temperature dropped down to RT (~ 290 K), and the initial arrangements of both fullerene molecules are shown in **Figure 6.13** (a). In this region, most of C_{70} and C_{60} are shown in the mixed disordered phase, with some small regions of δ phase DT remaining within the large C_{60}/C_{70} domain. It indicates that both C_{60} and C_{70} transfer into a liquid phase during annealing, and diffuse randomly on the Au(111) substrate, which makes the fullerene molecules well mixed with each other. In a few regions, as highlighted in yellow dotted line, it is noticed that the small regions of mixed C_{70}-C_{60}/DT dimer framework structure have started to form. Compared with the time required for the C_{70}/DT dimer row regions to appear, the formation of this dimer framework structure takes much shorter time. In addition, as the self-assembled structures in fullerene/alkanethiol system are strongly related to the local coverage of thiol molecules and the fullerene-thiol ratio, it indicates that in these small regions, the coverage of DT and the fullerene-DT ratio have no obvious change, so that the same dimer framework structure is able to reform.

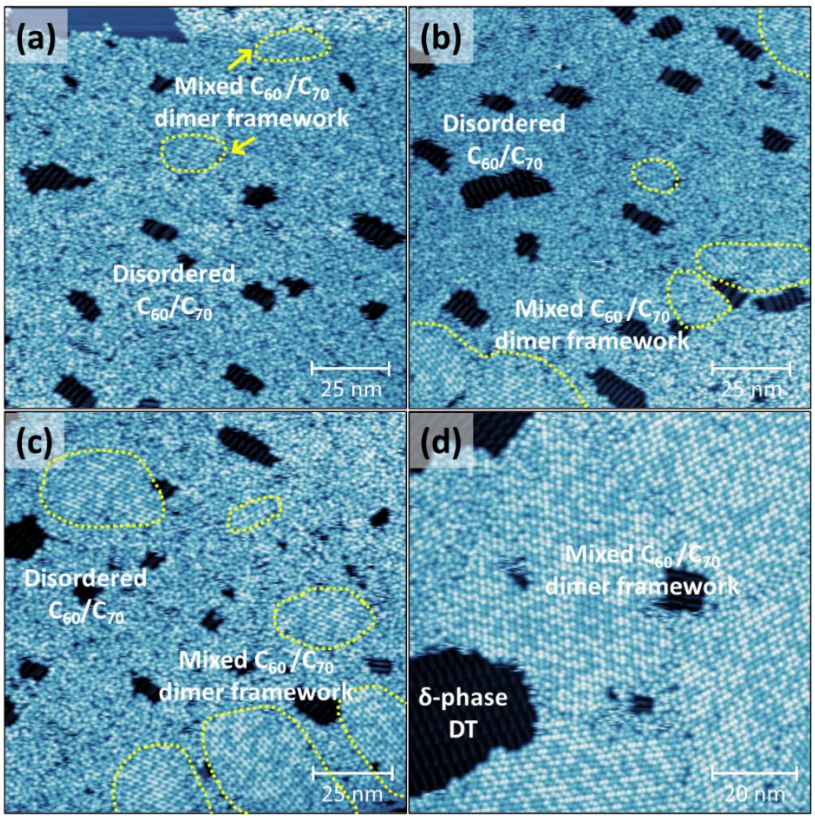

Figure 6.13 (a) The STM image collected soon after the annealing when the temperature of the annealed C_{70}+C_{60}/DT/Au(111) sample drop down to RT. Most of fullerenes are in disordered phase. The regions of initial mixed C_{70}-C_{60}/DT dimer framework structure are highlighted in yellow dotted lines. (b) The sample after left at RT for 2 hours. More of fullerenes start to form into the dimer framework structure. (c) The sample after left at RT for 4 hours. The regions of mixed C_{70}-C_{60}/DT dimer framework phases grow larger. (d) The STM image collected 12 hours after the annealing. Most of disordered fullerene have joined the mixed C_{70}-C_{60}/DT dimer framework phase, which is consisted of C_{70}-C_{70} dimers, C_{60}-C_{70} dimers and C_{60}-C_{60} dimers.

The STM image in **Figure 6.13** (b) and (c) are collected several hours after the annealing. It is noticed that the disordered fullerene molecules form into the mixed fullerene/DT dimer framework structure in more regions simultaneously, and those existing dimer framework phase expand larger significantly. According to this feature, we deduce that the coverages of C_{60}, C_{70} and DT in disordered phase are relatively even on Au(111) substrate, which allows this dimer framework to form anywhere within these disordered fullerene/DT domains.

After the C_{70}+C_{60}/DT/Au(111) sample is left at RT for about 12 hours, most of the fullerenes have been consumed to form the mixed C_{70}-C_{60}/DT dimer framework structures, as shown in **Figure 6.13** (d). The arrangement of C_{70} and C_{60} seems to be well mixed, though in different regions the local coverage of C_{70} or C_{60} is relatively higher. Thus, there are in total three types of fullerene dimers within this dimer framework, respectively C_{70}-C_{70} dimers, C_{60}-C_{70} dimers and C_{60}-C_{60} dimers, which is the same with the mixed C_{60}-C_{70}/DT dimer framework we introduced in **Figure 6.4**. Overall, the C_{70} and C_{60} molecules are evenly distributed. This large domain of dimer framework is consisted of several small domains of dimer framework, and the fullerenes at the boundaries of each dimer frameworks are still disordered. At the edge of dimer frameworks, there is a clear boundary between fullerene and DT, which indicates that most of DT also have been consumed to form this mixed C_{70}-C_{60}/DT dimer framework.

3.3.2 Statistical Analysis

The C_{70}+C_{60}/DT/Au(111) sample is found covered by this mixed C_{70}-C_{60}/DT dimer framework phase formed with three types of fullerene dimers, as shown in **Figure 6.14** (a). To collect more details of this structure, we carefully counted the number of C_{60}-C_{60} dimers, C_{60}-C_{70} dimers and C_{70}-C_{70} dimers in α-type and β-type respectively, and the results are shown in the table in **Figure .14** (b).

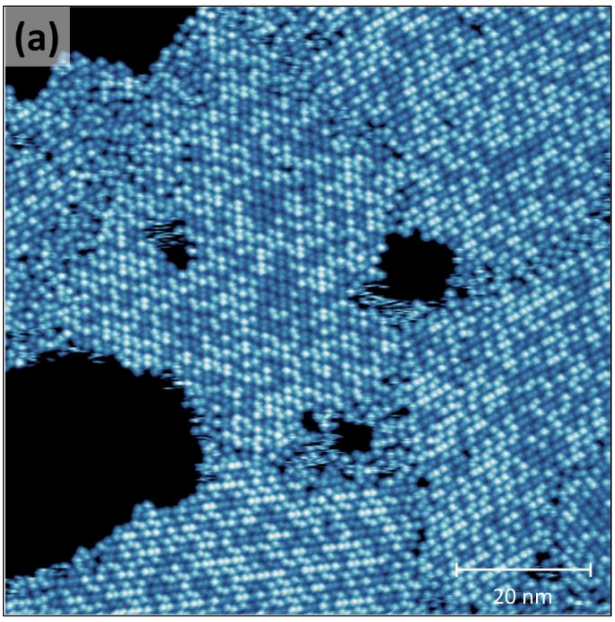

(b) **Dimers Ratio**

TYPE	C_{60}-C_{60}	C_{60}-C_{70}	C_{70}-C_{70}
α	201	334	165
β	101	327	346
Total	302	661	511

Figure 6.14 (a) A 100 nm * 100 nm area on the C_{70}+C_{60}/DT/Au(111) sample selected for counting the number of different types of fullerene dimers. (b) The table showing the number of each type of fullerene dimers.

The table in **Figure 6.14** (b) shows the numbers of all the types of dimerized fullerene in **Figure 6.14** (a). In this area, there are in total 2948 fullerene molecules that participate in the formation of this mixed C_{70}-C_{60}/DT dimer framework domain, including 1265 C_{60} molecules and 1683 C_{70} molecules, and the C_{60}-C_{70} ratio is thus about 3 : 4. Since we assume that both fullerene molecules have been well mixed, this C_{60}-C_{70} ratio reflects the overall number ratio of C_{60} and C_{70} deposited onto the DT/Au(111) sample. Among the 1474 fullerene dimers, there are 302 C_{60}-C_{60} dimers (20.49%), 661 C_{60}-C_{70} dimers (44.84%) and 511 C_{70}-C_{70} dimers (34.67%). If we deposited the same amount of C_{60} and C_{70} onto the sample, the C_{60}-C_{60} : C_{60}-C_{70} : C_{70}-C_{70} dimers ratio would be close to 1 : 2 : 1.

As we introduced in **Figure 6.2** (b), this fullerene/DT dimer framework structure includes two types of fullerene dimers, we then count the number of different fullerene dimers in α-type and β-type. For C_{60}-C_{60} dimers, 201 of them are in α-type and 101 of them are in β-type, and the α-β ratio is about 2 : 1; for C_{60}-C_{70} dimers, 334 of them are in α-type and 327 of them are in β-type, and the α-β ratio is about 1 : 1; for C_{70}-C_{70} dimers, 165 of them are in α-type and 346 of them are in β-type, and the α-β ratio is about 1 : 2. It is noticed that C_{60}-C_{60} dimers prefer to form in α-type, and

C_{70}-C_{70} dimers prefer to form in β-type. According to the structural details of C_{60}/DT dimer framework structure, the distance of fullerenes in α-type dimers is close to distance of close-packed C_{60}, and that seems to be a preferred and more stable binding type for C_{60}. However, that may result in C_{70} over occupying the space, though they can still arrange into the α-type C_{70}-C_{70} dimers in a standing up orientation, it may require stronger local van der Waals interaction of DT to stabilise the C_{70}-C_{70} dimers. For the β-type dimers, that distance of fullerenes is relatively larger. With a relatively larger space, C_{70} are able to slightly adjust their orientations and arrangements have a more stable binding with the substrate and interact more effectively with the surrounding DT molecules. For C_{60} molecules, the distance of β-type dimers is slightly too large, that without the DT molecules in the gaps separating the C_{60}, they would gather closer to keep a distance like in α-type dimers, which would further result in the phase changing from C_{60}/DT dimer framework phase to C_{60}/DT dimer row structure as we introduced in **Figure 6.2** (d). The distribution of C_{60}-C_{70} dimers is more even, with no obvious preference to arrange in α-type or β-type.

3.3.3 Formation of the Mixed Structure

Before we discuss the possible formation of this mixed C_{70}-C_{60}/DT dimer framework structure, it is necessary to introduce the thermal stabilities of C_{70}/DT system and C_{60}/DT system on Au(111) substrate first, which will lead to a better understanding of the formation of this mixed fullerene/DT structure.

For C_{70} molecules, when they are deposited onto the δ phase DT/Au(111) sample, the most stable self-assembled structure we found is the C_{70}/DT dimer row structure. During the thermal annealing of the C_{70}/DT/Au(111) sample, the C_{70} transfer into the disordered liquid phase, diffusing randomly on the substrate. Then after the annealing, it takes about 24 hours for dimer row structure to reform and about 72 hours for most of C_{70} transfer back into the dimer row structure at RT, as we introduced in **Table 4.1**. According to our observation, the annealing temperature at 60 °C is high enough to break the C_{70}/DT dimer row phase. However, there appears to be no great loss of DT before the annealing temperature reaches to 110 °C, as the C_{70} and DT are always able to reform into the same C_{70}/DT dimer row phase after being left at RT for the same time period. It indicates that there is a relatively strong interaction between C_{70} and DT alkane chains, and this interaction could prevent the DT to desorb significantly from the substrate during annealing.

For C_{60} molecules, the self-assembly of C_{60}/DT system is more complex. Due to the high symmetry of C_{60}, they are able to form various self-assembled structures with DT, and even a tiny difference in coverage of DT could lead to a different structure. According to the previous work and our observations, it is likely that there is a step-by-step phase changing for C_{60}/alkanethiol system with the reducing of alkanethiol coverage. From i) the large porous framework structure[7], to ii) the small porous framework[2], to iii) the dimer framework structure (**Figure 6.2** (b)), to iv) the dimer row structure (**Figure 6.6** (c)), to v) the single chain structure[1], the fullerene-thiol ratio gradually drops. Especially, in the work contributed by Xia *et al.*, the C_{60}/DT/Au(111) sample is treated with thermal annealing from 50 °C to 120 °C. After each annealing, the self-assembled structures of C_{60}/DT gradually transfer towards the phase with lower DT coverage, and eventually appear as close-packed C_{60} phase.

For this C_{60}/DT dimer framework structure we introduced in **Figure 6.2** (b), it forms on the C_{60}/DT/Au(111) sample after the initial deposition of C_{60}, but disappears after annealing (50 °C to 120 °C) and does not reform at RT, which indicates that there is an obvious desorption of the DT molecules during annealing. It appears that the DT molecules on the C_{60}/DT/Au(111) sample are less stable than on the C_{70}/DT/Au(111) sample. It is possible that the van der Waals interaction of C_{70} and DT alkane chains is stronger than that of C_{60} and DT alkane chains. With a relatively larger size of C_{70}, they are able to interact with DT more effectively, so that the van der Waals interaction could be strong enough to stabilise the DT and prevent the desorption. While for C_{60}, that van der Waals interaction is less strong, thus the DT keep desorbing from the substrate during annealing. With fewer DT molecules involved, the C_{60}/DT then arrange into the phase with lower fullerene-thiol ratio.

When we add the C_{70} to C_{60}/DT/Au(111) sample, it is interesting to notice that this C_{60}/DT dimer framework structure is able to reform after annealing with the participating of C_{70}. During annealing, the C_{70} and C_{60} both transfer into the disordered liquid phase, diffusing randomly on the substrate, so that the two kinds of fullerenes are well mixed. Due to the relatively stronger interaction of C_{70} and DT alkane chains, those evenly distributed C_{70} molecules help to stabilise the local DT molecules, and the desorption of DT is thus significantly obstructed. With much less loss of DT, the coverage of DT remains similar than that before annealing, and the C_{60} then reform into the dimer framework structure on Au(111) substrate, which indicates that the local fullerene-

DT ratio remains the same. Though we have no specific values showing how effectively the C_{70} reduce the desorption of DT during thermal annealing, we know that it is the effect of C_{70} that help this self-assembled structure to reform.

In addition, we also notice that the mixed C_{70}-C_{60}/DT dimer framework structure is the only ordered structure that appeared after the annealing. However, according to our observation in **Figure 6.14**, the amount of C_{70} molecules is about 33% more than C_{60} molecules on the sample, while the overall self-assembled structure is still dominated by C_{60}. Even in some local regions where C_{70} molecules are only distributed, they still arrange into the dimer framework structure. That feature is quite different from the feature we observed in **Figure 6.3** before annealing, where the C_{70} arrange into their own C_{70}/DT dimer row structure in the regions mainly distributed by C_{70} molecules. Why the C_{70} molecules seem to be more preferred to form into C_{60}/DT dimer framework structure after annealing? Here we come up with some possible explanations for this question.

i) The self-assembly of C_{60}/DT system is much faster than the self-assembly of C_{70}/DT system. According to our observation, the C_{60}/DT self-assembled structures start to form within 2 hours after deposition of C_{60} or thermal annealing, and it takes about 24 hours for most of C_{60}/DT domains transferring into the ordered phase. While for C_{70}/DT system, it takes at least 24 hours for the smallest unit of C_{70}/DT dimer row phase to form, and about 72 hours for most of C_{70}/DT domains transferring into the ordered phase. This difference could be strongly related to the symmetries of C_{60} and C_{70}. With a higher symmetry, it is easier for C_{60} to form into ordered phases in various ways, on the contrary, the C_{70} are only able to form into ordered phases in several specific molecular orientations, which requires a longer time period. It is possible that before the C_{70} adapted into those specific molecular orientations, they have been guided by the C_{60}/DT dimer framework structure which already formed. In the area shown in **Figure 6.3**, the C_{70}/DT dimer row structure is able to form because most of C_{60} have been consumed to form into the dimer framework domain, and only the few C_{60} molecules at the boundaries are able to diffuse into the C_{70} domain without annealing, so that only the C_{70} close to the boundaries of C_{60}/DT domain are guided to join the dimer framework structure. For the rest of the C_{70}, which are less affected by C_{60}/DT structural inertia, they would have enough time to arrange into their own self-assembled structures.

ii) The formation process of C_{60}/DT dimer framework structure starts before the sample temperature dropped to RT. As we introduced, the self-assembly of different system have different properties, and the formation of self-assembled structures also varies at different substrate temperatures[18-20]. When the annealing of sample stopped, it takes about 2 to 3 hours for the sample cooling down to RT. If the C_{60}/DT dimer framework structure have been forming during the cooling process, till the sample temperature is eventually stabilised at RT, the self-assembly of C_{60}/DT system would have lasted for a few hours. It is considered to be possible as we have observed the ordered phase on C_{60}/DT/Au(111) sample soon after the deposition or annealing. While for the C_{70}, even the sample temperature have dropped to RT, it still requires over 20 hours for C_{70}/DT self-assembled structure to form. Thus before the formation of their own structures, the C_{70} molecules could have been consumed to form the C_{60}/DT dimer framework. However, we have not conducted any variable temperature scanning for our samples, and that needs to be further studied with the equipment such as variable-temperature STM (VT-STM), which could provide us with more useful information.

3.4 Simultaneously Deposition of C_{60} and C_{70} on Decanethiol/Au(111)

Since we have observed the interesting self-assembled structure of well mixed C_{60} and C_{70} molecules on δ phase DT/Au(111) sample after thermal annealing, we wonder if the similar structures would appear when molecules are deposited onto the sample surface at the same time. The deposition process provides the fullerene molecules with additional kinetic energy, enabling them to diffuse further across the sample surface, which is similar to the effect of annealing the sample. Therefore, we decide to simultaneously deposit the C_{60} and C_{70} molecules onto the DT/Au(111) sample, to compare with the features shown on the annealed C_{70}+C_{60}/DT/Au(111) sample.

3.4.1 Sample Preparation

To make the results more comparable, we prepare the sample using exactly the same method before the deposition of fullerene molecules. The substrate we use is also a clean and flat Au(111) film, and it is immersed into a 1 mM 1-decanethiol solution in ethanol (99.5%) for 12 hours at RT. The DT/Au(111) sample is then transferred into the UHV chamber, treated with the thermal annealing at 120 °C for 1 hour, during which the DT molecules partially desorb from the substrate and the

remaining DT molecules arrange into δ phase on Au(111) substrate. The evaporation sources of C_{60} and C_{70} are then heated up to 410 °C and 380 °C respectively, and the δ phase DT/Au(111) sample is exposed to both evaporation sources simultaneously. The deposition time of C_{60} and C_{70} is respectively 10 minutes and 5 minutes, so that the coverage of both fullerene molecules is consistent with that of the annealed C_{70}+C_{60}/DT/Au(111) sample. The vacuum of preparation chamber during deposition is kept below 1.0×10^{-8} mbar. And the prepared C_{60}/C_{70}/DT/Au(111) sample is transferred to the analysis chamber of the LT-STM for imaging. The scanning of this sample is conducted in UHV (~ 1.0×10^{-11} mbar) at RT (~ 290 K).

3.4.2 Structural Features

Figure 6.15 (a) shows the sample soon after the deposition of C_{60} and C_{70} molecules. The two kinds of fullerene molecules mix well together and form into a large disordered fullerene domain. Then, after the C_{60}/C_{70}/DT/Au(111) sample is left at RT for over 24 hours (**Figure 6.15** (b)), we observe that the C_{60}/DT dimer framework structure and C_{70}/DT dimer row structure start to form within the disordered fullerene domain. It is interesting to notice that these two structures seem to appear at the same time on this sample, which is different from the features we have observed. According to our discussion about the formation of different fullerene/DT self-assembled structures, the C_{60}/DT dimer framework structure is expected to appear much earlier than the C_{70}/DT dimer row structure, while the formation of C_{60}/DT dimer framework structure seems to be restricted until the C_{70}/DT dimer row structure begins to form.

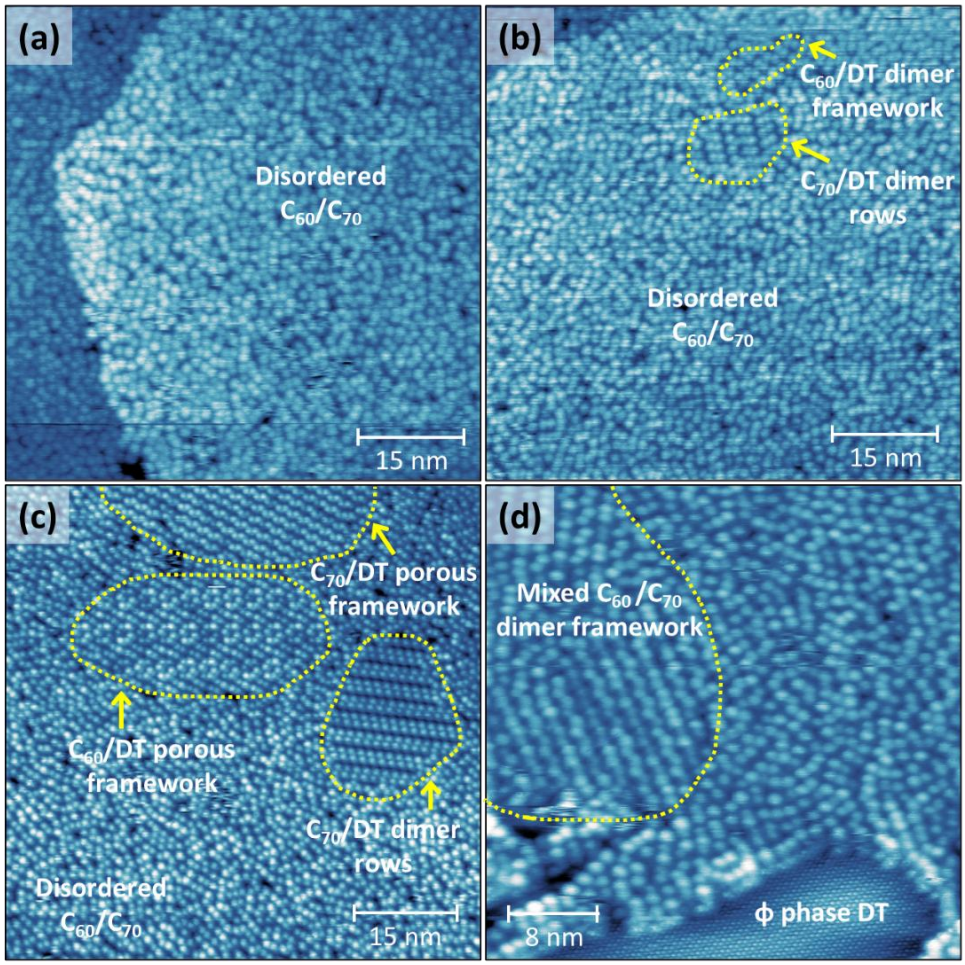

Figure 6.15 (a) The STM image collected within 24 hours after deposition of fullerenes. The C_{60} and C_{70} molecules are still in disordered liquid phase. (b) The small regions of C_{60}/DT dimer framework structure and C_{70}/DT dimer row structure appear on C_{60}/C_{70}/DT/Au(111) sample after the sample is left at RT for over 24 hours. (c) The C_{70}/DT dimer row structure, the C_{70}/DT porous framework structure and the C_{60}/DT porous framework structure are found coexisting on the substrate after the sample is left at RT for over 72 hours. Each structure is formed with both C_{60} and C_{70} molecules. (d) The mixed C_{60}/C_{70} dimer framework structure is observed on the sample over 72 hours after deposition. The region size of this structure is limited.

After the C_{60}/C_{70}/DT/Au(111) sample is left at RT for over 72 hours, various self-assembled structures of both C_{60}/DT and C_{70}/DT systems appear on the substrate, as shown in **Figure 6.15** (c). The C_{70}/DT dimer row structure, the C_{70}/DT porous framework structure and the C_{60}/DT porous framework structure are found to coexist in this area, but the region sizes of each

ordered phase is relatively smaller than those observed on pure C_{60}/DT/Au(111), C_{70}/DT/Au(111) and annealed C_{70}+C_{60}/DT/Au(111) samples after being left at RT for over 72 hours (**Figure 6.15** (d)). The ordered phase on these samples are able to expand to over 100 * 100 nm^2, which indicates that most of the fullerene molecules have been consumed to form the ordered phases. However, the maximum area of ordered phase appearing on this C_{60}/C_{70}/DT/Au(111) sample is approximately 40 * 40 nm^2, and only less than half of the fullerene molecules contribute to the formation of ordered phase, as we observed in **Figure 6.15** (c). The rest of the fullerene molecules remain in disordered phase, even they are given more time to diffuse locally and interact with DT molecules. It seems that not only the self-assembly process of the C_{60}/DT system are restricted, but the self-assembly process of the all the molecules on this sample is affected. And these self-assembled structures not only form more slowly, but also have lower coverages. We also observe the mixed C_{60}/C_{70} dimer framework structure on this sample, as shown in **Figure 6.15** (d). Similar with the features we mentioned above, the area of this dimer framework phase is small than that appears on the annealed C_{70}+C_{60}/DT/Au(111) sample. The possible reason for this feature will be further discussed later. Overall, the distributions of different ordered phases are relatively close to each other. In a local region, either two or three ordered phases coexist or no ordered phases appear at all.

Then we focus on the various of self-assembled structures observed on this sample. **Figure 6.16** (a) shows the two same structures as appearing on the C_{70}+C_{60}/DT/Au(111) sample before annealing, respectively the C_{70}/DT dimer row structure and mixed C_{60}-C_{70}/DT dimer framework structure. These two structures on different sample have the same structural features, and the main difference is their region sizes.

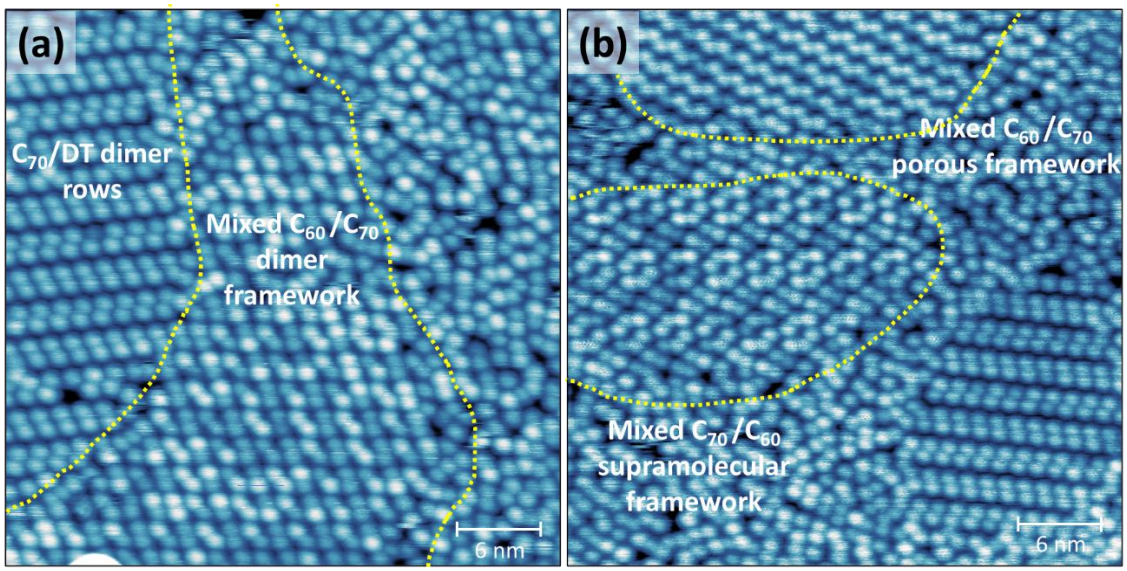

Figure 6.16 (a) The mixed fullerene/DT dimer framework structure and C_{70}/DT dimer row structure observed on the C_{70}+C_{60}/DT/Au(111) sample. (b) The mixed fullerene/DT porous framework structure and a new mixed fullerene/DT supramolecular framework structure observed on the C_{70}+C_{60}/DT/Au(111) sample.

In addition to these two same mixed fullerene/DT structures shown in **Figure 6.16** (a), more of mixed fullerene/DT structures are highlighted in yellow dotted lines in **Figure 6.16** (b). In this region, we observed the C_{60}/DT supramolecular framework structure[7] and the C_{70}/DT porous framework structure, which have only been observed on pure C_{60}/DT/Au(111) sample and C_{70}/DT/Au(111) sample respectively. Similar with the features of mixed C_{70}-C_{60}/DT dimer framework structure, some of the C_{70} and C_{60} molecules within their ordered phases are replaced by the other kinds of fullerene molecules, and thus they form into the mixed C_{70}-C_{60}/DT supramolecular framework structure and the mixed C_{60}-C_{70}/DT porous framework structure.

In the region of mixed C_{70}-C_{60}/DT supramolecular framework structure, the C_{70} replace some of the C_{60}, arranging into this structure in a standing up molecular orientation. And thus we can easily distinguish the C_{70} within this phase according to the molecular heights (brightness). However, this mixed C_{70}-C_{60}/DT supramolecular framework is still slightly different from that of pure C_{60}/DT systems, that there are some fullerene dimers filled within this framework, which are likely to be contributed by the C_{70} in different molecular orientations. However, we have not come up with a specific result due to the lack of LT scanning data. For the region of mixed C_{60}-C_{70}/DT

porous framework structure, it is also easy to distinguish the C_{60} molecules within this phase, where the C_{60} molecules are lower and shown as dimmer molecules in the STM image. From the features shown on this C_{70}+C_{60}/DT/Au(111) sample, we speculate that as long as there are proper coverage of DT molecules on Au(111) substrate, both C_{70} and C_{60} have the ability to join any self-assembled structures of the other fullerene molecules. And thus it is possible for us to guide the fullerene molecules to form into a specific structure through the effect of structural inertia.

3.4.3 Formation of Structures

According to our observation, the formation of the self-assembled structures on this C_{70}+C_{60}/DT/Au(111) sample is slower compared with the other samples we introduced previously, and the final ordered phases have rather small region sizes. During the deposition of fullerene molecules, both C_{60} and C_{70} molecules are given relatively higher kinetic energy[21,22], which allows them to diffuse further on the substrate though the sample temperature is always kept at RT. Thus, the C_{60} and C_{70} molecules are able to mix well on the substrate, as we observed in **Figure 6.15** (a). Without annealing of the sample, the distribution of DT molecules remains uneven, which makes the local fullerene-DT interactions in different regions vary. And that is the most possible reason for various of fullerene/DT self-assembled structures forming on this sample. If the DT molecules diffuse as freely as fullerene molecules during the deposition, both DT and fullerene molecules were supposed to well mixed and form into a relatively more stable structures, as shown in **Figure 6.13** (d). However, these various self-assembled structures shown on the C_{70}+C_{60}/DT/Au(111) sample only occupy the rather limited area, and over half of the fullerene molecules remain in disordered phase when the molecules are locally stabilised at RT. Here we come up with several possible factors.

i) The C_{70} molecules within the fullerene/DT domain affect the self-assembly of C_{60}/DT system. As we discussed in **Figure 6.15** (b), the formation of C_{60}/DT dimer framework structure appears to be restricted after the deposition, and this structure is observed until the C_{70}/DT dimer row structure has formed. According to the shape of C_{70} molecules, we deduce that there is a stronger van der Waals interaction of C_{70} and DT alkane chains. As the C_{70} molecules evenly distributed within the disordered fullerene/DT domains, the DT molecules are thus locally held by neighbouring C_{70}, which makes it harder for C_{60} to interact with DT alkane chains and arrange the DT as they preferred. Then till the C_{70}/DT self-assembled structures start to form, some of C_{70}

molecules are consumed and stabilised in the ordered phases, and the neighbouring DT are freer to interact with C_{60}, so that the self-assembly C_{60}/DT is then able to start. In other words, if the C_{70} are unable to form into an ordered phase with DT, then the C_{60} in the neighbouring area cannot form into any ordered phase either. And it is consisting with our observation that the C_{60}/DT ordered phases always appear next to the C_{70}/DT ordered phases, as shown in **Figure 6.15** (c).

ii) The uneven distribution of DT on the Au(111) substrate could also be one of the main reasons. As we introduced in **Figure 4.1** (b), the distribution of DT on Au(111) substrate after 120 °C annealing is not even, and the coverage of DT varies from 0.33 ML to 0.23 ML. As we analysed, the C_{70} molecules restrict the diffusion of DT, and the local coverage of DT is thus partially fixed. Meanwhile, the diffusion of C_{70} is also restricted by neighbouring C_{60} and DT. With almost the same amount of C_{60} occupying the Au(111) substrate, it is harder for C_{70} to arrange onto their preferred binding sites. Without a proper fullerene-DT ratio, the fullerene/DT self-assembled structures are then unable to form, and it remains disordered phase in most of regions on the C_{70}+C_{60}/DT/Au(111) sample.

4. Conclusion

4.1 Summery

In this chapter, we mainly investigate the multicomponent self-assembly of mixed fullerene/DT system on Au(111) substrate. Three samples are treated with different deposition methods of fullerene molecules: i) DT/Au(111) + C_{60} + C_{70}; ii) DT/Au(111) + C_{70} + C_{60}; iii) DT/Au(111) + C_{60}/C_{70}. The sample i) and ii) are also treated with the thermal annealing at 70 °C.

For the sample i) and ii) before thermal annealing, it is found that both the self-assembled structures of C_{60}/DT system and C_{70}/DT system appear to guide the following added fullerene molecules to join the pre-existing ordered phase. After the self-assembled structures of the first deposited fullerene molecule formed, the arrangement of DT molecules at the boundaries are strongly fixed by the neighbouring ordered phase. And for the other fullerene molecules diffusing to the boundaries, they will be guided to adjust their molecular orientations and arrangements to fit into the pre-existing ordered phase, and we consider that as a low-strained phase growth with the guidance of structural inertia. In addition, when the C_{60} regularly arrange into the C_{70}/DT dimer

row structure, the whole dimer row structure are also arranged more regularly due to the higher symmetry of C_{60} molecule.

From the data of the sample i) and ii) after thermal annealing, we have found the most stable multicomponent self-assembled structure of C_{60}/C_{70}/DT system when all the molecules are well mixed and stabilised. This mixed structure is dominated by C_{60}/DT self-assembly, and both two types of fullerenes are arranged into the C_{60}/DT dimer framework structure. As it requires specific molecular orientation of C_{70} within their own structures, most of the C_{70} have been consumed by C_{60}/DT self-assembly before the formation of C_{70}/DT self-assembled structure.

From the DT/Au(111) + C_{60}/C_{70} sample, we have observed various of C_{60}/DT and C_{70}/DT self-assembled structures contributed by both C_{60} and C_{70} fullerenes, which reveals a high potential of the fullerene-alkanethiol system. By adjusting the coverage of thiol molecules on substrate and the ratio of fullerene molecules, it is possible for us to guide the fullerene molecules to form any specific self-assembled structures through the effect of structural inertia.

4.2 Improvement

Although the results of this experiment have revealed many interesting phenomena of multicomponent self-assembly in fullerene/DT system, there are still many improvements to be made.

i) It would be very helpful to conduct the variable temperature scanning for the samples. Through the continuous scanning of sample during the thermal annealing process, the thermal stabilities of the C_{70}/DT and C_{60}/DT system can be clarified, and the gradual phase changing of fullerene/DT system could also be observed.

ii) We can also try to change the C_{60}-C_{70} ratio on the sample by adjusting the deposition time of them. According to our discussion in **Figure 6.14**, with the C_{60}-C_{70} ratio of 3 : 4, the self-assembly is still dominated by C_{60}/DT. If we gradually increase the amount of C_{70} molecules, it is expected that an obvious phase changing would be observed at a certain C_{60}-C_{70} ratio, which can provide us with a more straightforward comparison of C_{60}/DT and C_{70}/DT self-assembly.

iii) To investigate the universality of this property of fullerene-alkanethiol self-assembly, we can repeat the experiment with more types of fullerene molecules and alkanethiol molecules, to

investigate whether they have the similar properties. And this may provide new insights for surface synthesis.

References

[1] Xia, C. Structure of Self-Assembled Monolayer of Decanethiol and C60 on Au(111) Studied by Scanning Tunnelling Microscope, Ph.D. thesis from the University of Birmingham, **2024**.

[2] Ding, H.; Zhang, X.; Li, B.; Wang, Y.; Xia, C.; Zhao, H.; Yang, H.; Gao, Y.; Chen, X.; Gao, J.; Pan, M.; Guo, Q. Orientational Growth of Flexible van Der Waals Supramolecular Networks. *Small Structures* **2023**, *5*, 2300230.

[3] Liu, S.; Lü, Y.; Kappes, M. M.; Ibers, J. A. The Structure of the C_{60} Molecule: X-Ray Crystal Structure Determination of a Twin at 110 K. *Science* **1991**, *254*, 408–410.

[4] Hedberg, K.; Hedberg, L.; Bühl, M.; Bethune, D. S.; Brown, C. A.; Johnson, R. D. Molecular Structure of Free Molecules of the Fullerene C_{70} from Gas-Phase Electron Diffraction. *J. Am. Chem. Soc.* **1997**, *119*, 5314–5320.

[5] Dubois, L. H.; Zegarski, B. R.; Nuzzo, R. G. Molecular Ordering of Organosulfur Compounds on Au(111) and Au(100): Adsorption from Solution and in Ultrahigh Vacuum. *J. Chem. Phys.* **1993**, *98*, 678–688.

[6] Poirier, G. E. Coverage-Dependent Phases and Phase Stability of Decanethiol on Au(111). *Langmuir* **1999**, *15*, 1167–1175.

[7] Zhang, X.; Fan, X.; Zhu, G.; Wang, Y.; Ding, H.; Lin, H.; Li, Y.; Li, Q.; Gao, J.; Pan, M.; Guo, Q. Two-Dimensional van Der Waals Supramolecular Frameworks from Co-Hosted Molecular Assembly and c_{60} Dimerization. *J. Phys. Chem. C* **2020**, *124*, 12589–12595.

[8] Johnson, R. E.; Meijer, G.; Bethune, D. S. C60 Has Icosahedral Symmetry. *J. Am. Chem. Soc.* **1990**, *112*, 8983–8984.

[9] Favre, H. A.; Powell, W. H. *Nomenclature of Organic Chemistry*; Royal Society of Chemistry: Cambridge, **2013**.

[10] Niu, G.; Geng, J.; Wang, X.; Yang, X.; Xiong, W.; Zhang, H.; Ruan, Z.; Zhang, Y.; Gao, L.; Lu, J.; Cai, J. Adsorption Configurations and Electronic Properties of Self-Assembled c_{60} and c_{70} Molecules on a Semiconductor CuSe Monolayer with Periodic Nanopores. *Nanotechnology* **2023**, *34*, 395602–395602.

[11] Liu, S.; Lü, Y.; Kappes, M. M.; Ibers, J. A. The Structure of the C_{60} Molecule: X-Ray Crystal Structure Determination of a Twin at 110 K. *Science* **1991**, *254*, 408–410.

[12] Maksymovych, P.; Oleksandr Voznyy; Dougherty, D. B.; Sorescu, D. C.; Yates, J. R. Gold Adatom as a Key Structural Component in Self-Assembled Monolayers of Organosulfur Molecules on Au(111). *Prog. Surf. Sci.* **2010**, *85*, 206–240.

[13] Bogdan Diaconescu; Yang, T.; Berber, S.; Mikael Jazdzyk; Miller, G. P.; Tománek, D.; Pohl, K. Molecular Self-Assembly of Functionalized Fullerenes on a Metal Surface. *Phys. Rev. Lett.* **2009**, *102*, 056102.

[14] Vaezi, M.; Nejat Pishkenari, H.; Nemati, A. Mechanism of C60 Rotation and Translation on Hexagonal Boron-Nitride Monolayer. *J. Chem. Phys.* **2020**, *153*, 234702.

[15] Jung, M.; Shin, D.; Sohn, S.-D.; Kwon, S.-Y.; Park, N.; Shin, H.-J. Atomically Resolved Orientational Ordering of c_{60}Molecules on Epitaxial Graphene on Cu(111). *Nanoscale* **2014**, *6*, 11835–11840.

[16] Matsumoto, M.; Junji Inukai; Tsutsumi, E.; Yoshimoto, S.; Kingo Itaya; Ito, O.; Fujiwara, K.; Murata, M.; Murata, Y.; Komatsu, K. Adlayers of c_{60}−c_{60} and c_{60}−c_{70} Fullerene Dimers Formed on Au(111) in Benzene Solutions Studied by STM and LEED. *Langmuir* **2004**, *20*, 1245–1250.

[17] Girard, C.; Ph. Lambin; Alain Dereux; Lucas, A. Van Der Waals Attraction between Two C_{60} Fullerene Molecules and Physical Adsorption of C_{60}. *Phys. Rev. B* **1994**, *49*, 11425–11432.

[18] Janas, A.; Jany, B. R.; Szajna, K.; A. Kryshtal; G. Cempura; Kruk, A.; Krok, F. Nanostructure Phase and Interface Engineering via Controlled Au Self-Assembly on GaAs(001) Surface. *Appl. Surf. Sci.* **2019**, *492*, 703–710.

[19] Packwood, D. M.; Han, P.; Hitosugi, T. Chemical and Entropic Control on the Molecular Self-Assembly Process. *Nat. Commun.* **2017**, *8*, 14463.

[20] Lei, P.; Zhao, L.; He, L.; Zhao, F.; Xiao, X.; Tu, B.; Zeng, Q. Temperature Induced Supramolecular Structural Transition and as a Host Cavity to Capture the Guest Molecules. *Appl. Surf. Sci.* **2021**, *550*, 149352–149352.

[21] Muratore, C.; Voevodin, A. A.; Glavin, N. R. Physical Vapor Deposition of 2D van Der Waals Materials: A Review. *Thin Solid Films* **2019**, *688*, 137500.

[22] Meyers, R. A. *Encyclopedia of Physical Science and Technology*, 3rd ed.; Academic Press, Cop: San Diego, 2001.

VII. Conclusions

I have conducted experimental investigations on the co-assembly of DT molecules and fullerene molecules. Both C_{60} and C_{70} are able to mix with DT to form regular two-dimensional structures on Au(111). The van der Waals interaction between the alkane chains of DT and the fullerene cage plays an important role in stabilising the fullerene/DT structure. The major findings from this study are:

1) The dense φ phase of DT is not permissible to fullerene molecules. The close-packed alkane chains in the φ phase prevent fullerene molecules reaching the Au(111) substrate. Moreover, the fullerene molecules cannot stay on top of the DT layer at RT.

2) The lower coverage δ phase consisting of nearly flat-lying alkane chains can accommodate fullerene molecules. Fullerene molecules interact directly with the Au(111) substrate. The interaction between the fullerene molecules and the DT chains prevents the fullerene molecule from forming phase-separated closed-packed structure. With the addition of fullerene molecules, DT molecules change their tilt angle from around 0° toward 90°. The flat-lying to standing up switching facilitates van der Waals interaction between DT and fullerene.

3) The DT-fullerene co-crystal has limited stability. Above 70 °C, the crystal would go through an order-disorder phase transition. Above 120 °C, partial desorption of DT occurs leading to the formation of close-packed fullerene. The formation of close-packed fullerene is irreversible.

4) C_{70}/DT has a rather simple structure composed of C_{70} dimer rows running in the $[11\bar{2}]$ direction. C_{70} take the lying down configuration with its long axis parallel to the substrate. There is also a framework structure which is less frequently observed.

5) C_{60}/DT can form a variety of stable structures. In comparison to C_{70}, C_{60} appears to be much more adaptive and can interact with DT more effectively.

When C_{60}, C_{70} and DT are mixed at 70 °C, a regular mixture can form upon cooling to RT. This three component mixture follows one of the C_{60}/DT structures with C_{70} randomly replacing C_{60}. C_{70} is forced to take the standing up orientation so that it takes up the same area as C_{60}. In the following, each of the observed structures are further elaborated.

1. C_{70}/Decanethiol Bicomponent Self-Assembly on Au(111) Surface

1.1 Summary

Through the RT scanning of the sample, we have collected enough information showing the structural details of the C_{70}/DT self-assembled structures. In addition, the formation and the thermal stability of these structures are also observed form our data, which help us to comprehensively understand this system from multiple perspectives.

The intramolecular information of C_{70} and the position of DT within the C_{70}/DT self-assembled structures are revealed through the LT scanning at 77 K. The C_{70}/DT dimer row structure, C_{70}/DT porous framework structure and the C_{70}/DT trimer row structure are analysed in detail, and the possible models of each structure showing the arrangements of C_{70} and DT on Au(111) substrate are established.

1.2 Further Work

1.2.1 LT Scanning at 5 K

It would be helpful to conduct the LT scanning at LHe temperature. With a lower temperature of the sample, there would be less thermal motion, and this would lead to improved resolution.

1.2.2 Refine the δ Phase DT Model on Au(111) Surface

As we previously mentioned, that the deposition of C_{70} might cause some DT to desorb leading to reduced coverage. However, when we tried to deposit C_{70} at different temperatures, the features shown on the sample have no obvious difference. It indicates that adding C_{70} may not cause changes in the DT coverage. And that could explain why there is a sharp boundary between C_{70}/DT dimer row phase and the δ phase DT, as we mentioned in Chapter IV **Figure 4.1**. As we are still unable to directly observe the whole DT chains and the S-Au-S staple, this fullerene-DT system

could provide us indirect evidence for the coverage of DT in δ phase. Meanwhile, the LT data of DT can also provide the useful information about the arrangement of DT.

1.2.3 More Useful Information from Other Instruments

i) Scanning tunnelling spectroscopy (STS): to find the DOS change of C_{70}; ii) X-ray photoelectron spectroscopy (XPS): to find the interactions between C_{70}-C_{70}, C_{70}-DT; iii) density functional theory (DFT) calculation and simulation: to prove our model or to find the more reasonable arrangements of the molecules within the self-assembled structure.

2. C_{70}/C_{60}/Decanethiol Multicomponent Self-Assembly on Au(111) Surface and the Guided Molecular Self-Assembly

2.1 Summary

For the sample i) and ii) before thermal annealing, we have noticed an interesting phenomenon that both of the self-assembled structures of C_{60}/DT system and C_{70}/DT system appear to guide the following added fullerene molecules to join the pre-existing ordered phase. After the self-assembled structures of the firstly deposited fullerene molecule formed, the arrangement of DT molecules at the boundaries are strongly fixed by the neighbouring ordered phase. And when the other fullerene molecules diffusing to the boundaries, these will be guided to adjust their molecular orientations and arrangements to fit into the pre-existing ordered phase, and we consider that as a low-strained phase growth with the guidance of structural inertia.

From the DT/Au(111) + C_{60}/C_{70} sample, we have observed various of C_{60}/DT and C_{70}/DT self-assembled structures contributed by both C_{60} and C_{70} fullerenes, which reveals a high potential of the fullerene-alkanethiol system. By adjusting the coverage of thiol molecules on substrate and the ratio of fullerene molecules, it is possible for us to guide the fullerene molecules to form any specific self-assembled structures through the effect of structural inertia.

2.2 Further Work

2.2.1 Variable Temperature Scanning

It would be very helpful to conduct the variable temperature scanning for the samples. Through the continuous scanning of sample during the thermal annealing process, the thermal stabilities of the C_{70}/DT and C_{60}/DT system can be clarified, and the gradual phase changing of fullerene/DT system could also be observed.

2.2.2 LT scanning at 5 K.

The fullerene and DT molecules will be more stable on the surface when the temperature drop down to 5 K. And it could be easier for us to find the clear molecular orientations for both C_{70} and C_{60}, which would provide us with direct evidence to prove our model.

2.2.3 Expansion of Guided Molecular Self-Assembly

To investigate the universality of this property of fullerene-alkanethiol self-assembly, we can repeat the experiment with more types of fullerene molecules and alkanethiol molecules, to investigate whether they have the similar properties. And this may provide new insights for surface synthesis.

3. Potential Applications

1) Nanoscale patterning

The self-assembly of fullerene/decanethiol on substrates (gold or other metals) enables precise control over nanoscale patterns. This can be used in nanolithography or to create templates for building complex nanostructures, such as quantum dots or nanowire arrays, with applications in sensors and optoelectronics.

2) Organic field-effect transistors

The excellent electron-accepting properties of fullerene make it a strong candidate for n-type semiconductors in organic field-effect transistors. Decanethiol SAMs can act as dielectric layers or molecular linkers to improve charge transport and interface stability between fullerenes and electrodes, enhancing device performance in flexible electronics.

3) Functional coatings

Fullerene/decanethiol assemblies can be used to create thin films with tailored electrical, optical, or thermal properties. For instance, these coatings can be applied to sensors, optical devices, or energy storage systems, where the fullerene contributes conductivity or light absorption, and the thiol ensures uniform deposition.

4) Photodetectors and sensors

Fullerene's ability to absorb light across a wide spectrum, combined with decanethiol's role in forming stable, ordered films, makes these assemblies suitable for photodetectors or optical sensors. The thiol layer can also be used to tune the bandgap or enhance charge transfer in these devices.